Bielefeld University
Faculty of Physics

Insights into Thermal Modifications of Charmonium and Bottomonium from a Comparison of Lattice QCD and Perturbative Spectral Functions

- PhD Thesis -

Anna-Lena Lorenz (geb. Kruse)

Supervisor and 1st Referee:
Dr. Olaf Kaczmarek

2nd Referee:
Prof. Dr. Frithjof Karsch

Bielefeld, 15.06.2021

Published Work

This thesis heavily relies on the work published in

> Y. Burnier, H.-T. Ding, O. Kaczmarek, A.-L. Kruse, M. Laine, H. Ohno and H. Sandmeyer, *Thermal quarkonium physics in the pseudoscalar channel.* JHEP 1711 (2017) 206. arXiv: 1709.07612.

The methods and results of this thesis have been partially published and presented in

> H. -T. Ding, O. Kaczmarek, A. -L. Kruse, H. Ohno and H. Sandmeyer, *Insight into thermal modifications of quarkonia from a comparison of continuum-extrapolated lattice results to perturbative QCD.* MDPI Proc. 10 (2019) 45. arXiv: 1901.04226.
>
> A.-L. Lorenz, H.-T. Ding, O. Kaczmarek, H. Ohno, H. Sandmeyer and H.-T. Shu, *Thermal modifications of quarkonia and heavy quark diffusion from a comparison of continuum-extrapolated lattice results to perturbative QCD.* arXiv: 2002.00681.

The method to obtain continuum correlators is an updated version of

> H.-T. Ding, O. Kaczmarek, A.-L. Kruse, H. Ohno and H. Sandmeyer, *Continuum extrapolation of quarkonium correlators at non-zero temperature.* EPJ Web Conf. 175 (2018) 07010. arXiv: 1710.08858.

The correlator data from this work have also been used in

> H.-T. Ding, O. Kaczmarek, A.-L. Kruse, S. Mukherjee, H. Ohno, H. Sandmeyer, H.-T. Shu, *Thermal modifications of charmonia and bottomonia from spatial correlation functions.* EPJ Web Conf. 175 (2018) 07021. arXiv: 1710.08587.
>
> H.-T. Ding, O. Kaczmarek, A.-L. Kruse, R. Larsen, L. Mazur, S. Mukherjee, H. Ohno, H. Sandmeyer, H.-T. Shu, *Charmonium and bottomonium spectral functions in the vector channel.* Nucl.Phys. A982 (2019) 715-718. arXiv: 1807.06315.

Based on the results from this thesis, a new paper

> H.-T. Ding, O. Kaczmarek, A.-L. Lorenz, H. Ohno, H. Sandmeyer and H.-T. Shu, *Charm and Beauty in the deconfined plasma from lattice QCD.* Work in progress

is in preparation.

Contents

Chapter 1

Introduction

For a long time, science tried to find out "what holds the world together in its innermost core". With the formulation of the Standard Model of Particle Physics in the 20th century, physicists finally got closer to an answer. Out of the four fundamental forces of nature, namely gravitational, electromagnetic, weak and strong force, the latter three are described in this standard model. Its constituents are the elementary particles, divided into leptons and quarks as well as the force carriers leading to interactions. Leptons contain the electron, muon, tauon and their corresponding neutrinos. They can interact via electroweak coupling mediated by photons and the $W^{\pm}, Z$ bosons. The six quarks (up, down, strange, charm, bottom and top) additionaly carry a property called color charge and are thus able to participate in the strong interaction mediated by gluons. The quark masses are largely different for the different flavors, ranging from $m_u \approx 2.3\text{MeV}$ for the light up quark to $m_t \approx 160\text{GeV}$ for the heavy top quark. This work focuses on two of the heavy quarks, the charm quark at a mass of $m_c \approx 1.28\text{GeV}$ and the bottom quark with $m_b \approx 4.18\text{GeV}$[1].

The field theory describing this strongly interacting matter is called Quantumchromodynamics (QCD), a non-abelian gauge theory with an underlying SU(3) symmetry, since there are three different values, named red, green and blue, that the color charge can take. What makes QCD interactions special in comparison to other interactions is the dependence on the distance of the quarks. While most forces decrease with increasing distance (decreasing energy scale), the strong force increases until the energy becomes large enough to create a new quark-antiquark pair. Due to this property called confinement, we do not observe single quarks, but hadrons, color-neutral combinations of quarks. There are combinations of three quarks, so-called baryons, like the proton and neutron, combinations of quark and antiquark, so-called mesons, and even more complex combinations like tetraquarks. A

[1] All masses in $\overline{\text{MS}}$-scheme at a scale of $\mu = m_Q$, taken from [1].

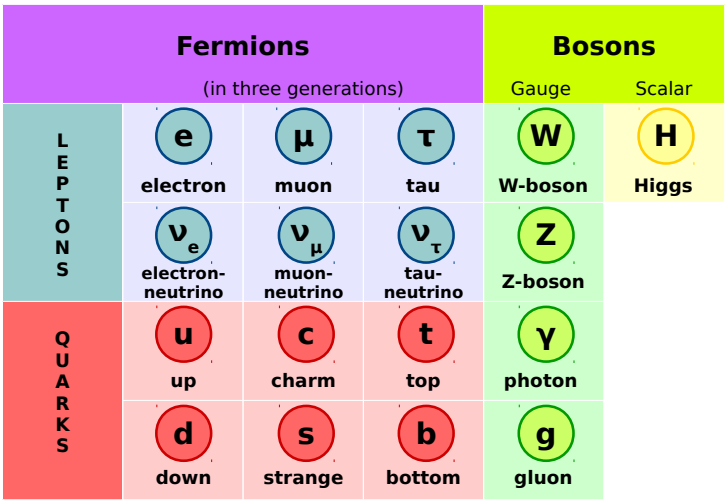

Figure 1.1: The Standard Model of Particle Physics.

special kind of these mesons are quarkonia, pairs of a quark and its antiquark of the same flavor. However, when decreasing the distance (increasing the energy scale), the strong force decreases and the quarks become asymptotically free [2]. The coupling constant is thus not constant, but depending on the energy scale.

The nature of strong interactions makes first principle investigations of QCD matter complicated. Perturbation theory often breaks down, as its underlying assumption of small couplings and approximately free particles is often not fulfilled. Only at high temperatures, perturbative QCD becomes applicable. A better, non-perturbative method in a lot of other cases is Lattice QCD (LQCD, [3]). First introduced by Kenneth Wilson in the 1970s, LQCD discretizes the continuous space-time on a four dimensional Euclidean lattice. With Monte-Carlo algorithms it is possible to simulate a medium using supercomputers. With the huge development in regards to computational power over the last decades, more and more physics has become accessible by LQCD. Despite facing some challenges (e.g. sign problem, doublers), LQCD has proven to be a powerful tool in investigating strongly interacting matter at different temperatures and zero or, with some tricks, small chemical potential.

With changing temperature or density, strongly interacting matter undergoes phase transitions. At high energies, present in e.g. neutron stars or the early universe, the hadrons dissolve and instead of ordinary matter, a quark-gluon-plasma (QGP,[4]), where the quarks and gluons are no longer bound, forms. With colliders like the LHC, these extreme conditions are accessible

to experiments as well. In probing the QGP, heavy quarkonia, i.e. charmonia and bottomonia[2], can play a crucial role. Due to their large mass, they can rarely be created after equilibration of the medium. They are produced in the early stage of the collision and their suppression can later be used to gain information. As Matsui and Satz argued in [5], the suppression of the charmonium bound state J/ψ, also observed experimentally at RHIC and LHC [6–10], could signal the formation of a QGP. Therefore an interesting feature of heavy quarks is the sequential melting of their bound states. Not all bound states vanish immediately, when crossing the critical temperature, but some persist up to higher temperatures. This was also observed in experiments [11, 12] and heavy quarkonia can thus be used as a thermometer. Therefore, it is of fundamental importance to obtain as much information on these quarkonia as possible. How many states are there? At which energies? What are the dissociation temperatures?

In principle, this information is included in the change of hadronic spectral function and there have been many attempts to find a suitable spectral function with different methods, including the aforementioned Lattice QCD. However, a direct calculation of spectral functions on the lattice is impossible. Instead, LQCD uses correlation functions that are related to spectral functions via an integration with a kernel. Extracting a spectral function out of a few lattice points for the correlators is an ill-posed inversion problem due to the many degrees of freedom. Imposing some conditions, like the positivity of spectral functions, excludes many possibilities, but the number of spectral functions that are suitable to describe the correlator data still remains infinite. Several methods have been proposed to extract meaningful spectral functions, most of them relying on Bayesian statistics [13]. To gain a deeper understanding, often combined efforts of different methods are needed. This work tries to gain insight into in-medium modifications of charmonium and bottomonium by comparing continuum extrapolated lattice correlators to a perturbative spectral function. Using a perturbatively inspired model we investigate the intermediate and higher frequency regime of the spectral function. From this comparison we can understand wether the search for spectral functions can be treated perturbatively at certain temperatures and conditions.

For the small frequency part in the vector channel, where perturbation theory does not provide an ansatz, we use a Lorentzian ansatz [14] to gain information on the heavy quark diffusion coefficient D and the drag coefficient η. The heavy quark diffusion coefficient is (along with other transport coefficients) of crucial importance for understanding heavy ion collisions. Most theories focus on a medium in equilibrium, but the quark-gluon-plasma cre-

[2]A quarkonium of the top-quark and antiquark is hard (maybe even impossible) to observe, as the formation time of toponium might be longer than the life-time of the extremely heavy top-quark.

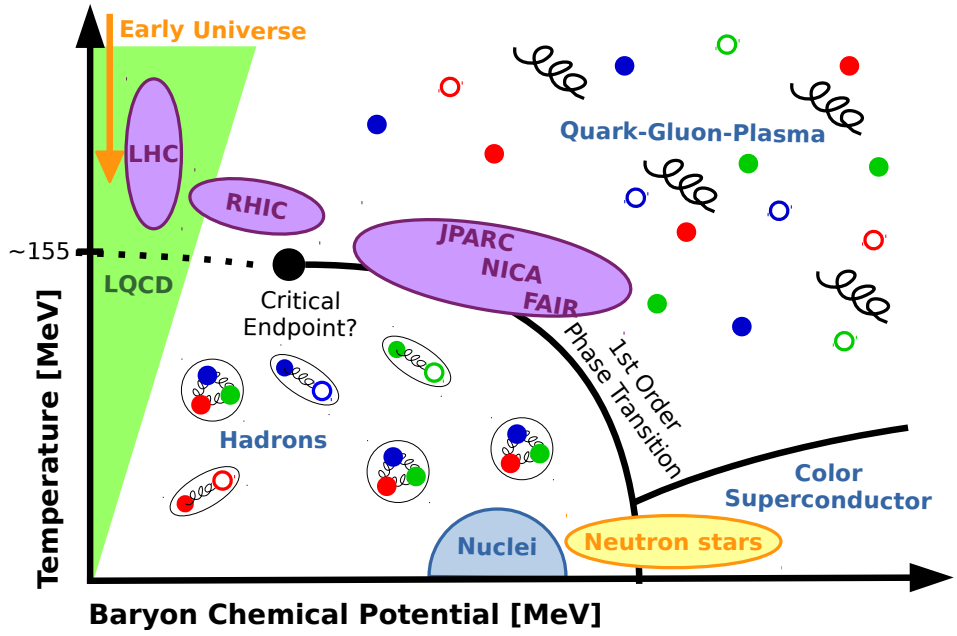

Figure 1.2: Phase diagram of QCD matter. At low temperature and density, the quarks are bound in hadrons. When going to more extreme conditions, there are different kinds of phase transitions. The solid black line stands for a first order phase transition. At a certain point, this line ends and below this density there is only a crossover between different phases. The nature of this point is still debated. The orange marks show, where some of the extreme conditions are realized in nature. The purple marks show where some experiments operate. Lattice QCD (green) is only applicable at zero or, with great effort, at small baryon chemical potential. This work is placed along the temperature-axis (zero baryon chemical potential).

ated in a collision expands and cools down and is thus not in equilibrium. On the experimental side, we can only observe the result of the collision, when particles hit a detector, which is after the chemical freeze-out. The evolution of the medium from the collision to this point is unclear and can only be modelled. The transport coefficients are an important input to these transport models, so extracting D from an analysis of the transport contribution is a goal of this work. So far, a lot of effort has been made to estimate the heavy quark diffusion coefficient from different ansätze, e.g. perturbation theory, lattice methods or transport models. But most methods lead to large uncertainties and in addition the agreement between different ansätze is not very high. The current state of research provides more of a range, in which we would expect the coefficient, than an actual value. With this work, we will check towards which end of this range our method hints. In total, we analyze pseudoscalar and vector correlators at four temperatures above T_c

(1.1, 1.3, 1.5 and $2.25T_c$) and also provide a correlator for $0.75T_c$.

The outline of this thesis is as follows: In chapter 2, we start with an introduction to correlators and spectral functions by building an intuition for their relation. We present the current state of the research on spectral functions as well as the diffusion coefficient. A special focus lies on the construction of a perturbative spectral function in section 2.3.3 by combining pNRQCD calculations with vacuum asymptotics. To obtain correlators, we apply LQCD. After a brief introduction to this powerful tool, chapter 3 provides the necessary information on the lattices used in this work. As we work with continuum extrapolated data to reduce cut-off effects and make a comparison to perturbation theory possible, we also present the extrapolation method. The continuum correlators are shown and compared to perturbation theory in chapter 4. We account for systematical uncertainties and build a model for the spectral function based on the perturbative ansatz. While this is relatively straightforward for the pseudoscalar channel (see section 4.1), the presence of the transport peak provides some challenges in the vector channel (4.3). The differences between the perturbative description and the data hint to a transport contribution and are further analyzed in chapter 5. We gain a qualitative understanding of the transport contribution and also show two attempts to analyze this more quantitatively, before we conclude with a brief summary and outlook.

This work uses the quenched approximation, but the method for obtaining the continuum limit (chapter 3), as well as the comparison to a perturbatively inspired model (chapter 4) and the analysis of the transport peak (chapter 5) would work in full QCD as well. The methodology of this thesis thus provides a basis for further studies.

Chapter 2

Heavy Quarkonium Correlators and Spectral Functions

All information on the in-medium modification of bound states as well as transport properties are encoded in spectral functions. The simplified qualitative shape of the spectral function is shown in Fig. 2.1. At zero temperature, the spectral function consists of a continuum part describing asymptotically non-interacting quarks at higher frequencies ω (see section 2.3.1) and δ peaks describing the bound states at intermediate ω. When increasing the temperature, these peaks get broadened until they melt and dissolve while the threshold of the continuum part shifts to lower frequencies. So far, it is not clear, wether the location of the bound states shift. While some studies based on potential model calculations find that the bound state mass decreases with increasing temperature [15], others do not [16]. In the vector channel a transport peak in the form of a Lorentzian arises on the other side of the spectrum (see section 2.4.3). The shape of this peak is determined by the drag coefficient η and the heavy quark diffusion coefficient D and transforms into a δ peak at infinite temperature. In the pseudoscalar channel there is no such transport contribution.

Unfortunately, this is only a qualitative description as spectral functions are not easily accessible. There are many different approaches to find a spectral function, e.g. using perturbation theory (see 2.3.3). In this work we used lattice QCD, where we do not directly calculate the spectral function but instead measure hadronic correlation functions related to the spectral function via a Laplacian transformation problem. For an overview on lattice QCD see chapter 3. To make use of the path integral formalism, lattice correlators are calculated in imaginary time. But since the corresponding spectral function is the same in Minkowski space, Euclidean correlators are

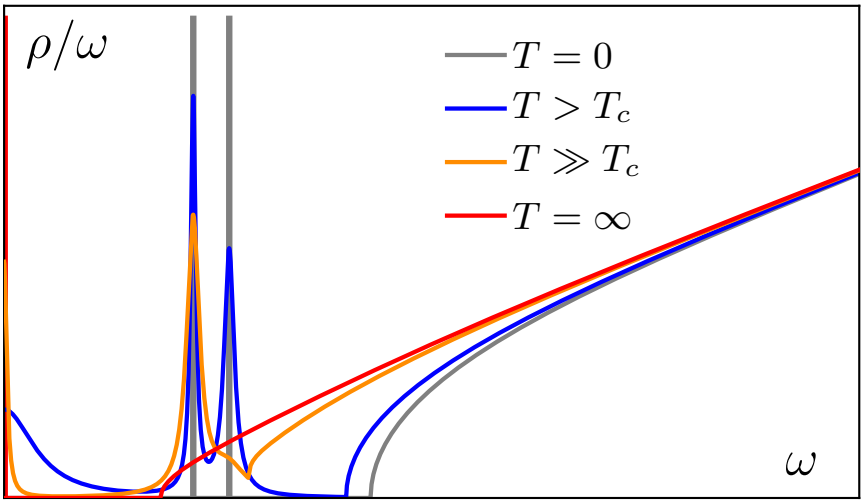

Figure 2.1: Qualitative shape of the spectral function at different temperatures.

a great tool to investigate real-time physics.

In this section, we will give an overview on hadronic correlators and their computation in Euclidean space (see sec. 2.1). While these observables can be used to perform hadron spectroscopy and are thus an interesting quantity themselves, this work mostly focuses on their relation to the spectral functions. Since we are interested in the properties of heavy quarkonia, we define mesonic correlators. For baryonic correlation functions, see [17].

2.1 Hadronic Correlators

The correlation function is defined as

$$G(\tau) = \langle O(\tau) O^\dagger(0) \rangle \,, \tag{2.1}$$

where O is an operator describing an observable, e.g. a meson with specific quantum numbers. On the lattice, we calculate current-current correlators

$$G(\tau) = \langle J_H(\tau, \vec{x}) J_H^\dagger(0, \vec{0}) \rangle \,. \tag{2.2}$$

In this case, O is a meson interpolator given by

$$O_H^{f_1,f_2}(\tau) = \bar{\psi}^{f_1}(n) \Gamma_H \psi^{f_2}(n), \tag{2.3}$$

where the f_i denote the quark flavors ($f_1 = f_2$ for quarkonia), H the channel and n the lattice site, where the fermion is created. Tab. 2.1 gives an overview of the different channels and their corresponding matrices.

Channel	Γ_H	$^{2S+1}L_J$	J^{PC}	$c\bar{c}$	$M(c\bar{c})$ [GeV]	$b\bar{b}$	$M(b\bar{b})$ [GeV]
Vector	γ_μ	$^3S_1$	1^{--}	J/ψ	3.097(1)	Υ	9.460(3)
Axial Vector	$\gamma_5\gamma_\mu$	$^3P_1$	1^{++}	χ_{c1}	3.511(1)	χ_{b1}	9.892(1)
Scalar	1	$^3P_0$	0^{++}	χ_{c0}	3.415(3)	χ_{b0}	10.233(1)
Pseudoscalar	γ_5	$^1S_0$	0^{-+}	η_c	2.981(1)	η_b	9.399(2)

Table 2.1: Charmonium and bottomonium states in different channels with masses taken from the Particle Data Group booklet ([1]).

In real time, we can write the correlator as a linear combination

$$G(t) = i\left(G^{>}(t) - G^{<}(t)\right), \tag{2.4}$$

where

$$G^{>}(t) = \langle O(t)O(0)\rangle \quad \text{and} \quad G^{<}(t) = \langle O(0)O(t)\rangle = G^{>}(-t). \tag{2.5}$$

Using the time evolution operator, we can express $O(t)$ as $e^{iHt}O(0)e^{-iHt}$, which allows us to write $G^{>}(t)$ as a sum over states $\langle n|$, $\langle m|$:

$$G^{>}(t) = \frac{1}{Z}\sum_{m,n} e^{-\beta E_n} e^{it(E_n - E_m)} || \langle n| O(0) |m\rangle ||^2, \tag{2.6}$$

where Z denotes the canonical partition function, β is the inverse of the temperature an $E_{n,m}$ are the energies corresponding to the states $\langle n|, \langle m|$.

By taking a Fourier transform, we obtain the spectral function

$$\rho(\omega) = \frac{1}{\pi i}\int_{-\infty}^{\infty} \mathrm{d}t\ e^{i\omega t} G(t) = G^{>}(\omega) - G^{<}(\omega). \tag{2.7}$$

With the Kubo-Martin-Schwinger relation [18, 19]

$$G^{>}(t) = G^{<}(t + i\beta) \tag{2.8}$$

we get

$$G^{>}(\omega) = \frac{e^{\beta\omega}}{e^{\beta\omega} - 1}\rho(\omega), \quad G^{<}(\omega) = \frac{1}{e^{\beta\omega} - 1}\rho(\omega). \tag{2.9}$$

We can now define the retarded correlator

$$G_R(\omega) = \int_0^{\infty} \mathrm{d}t e^{i\omega t} G(t), \tag{2.10}$$

with which we can rewrite the spectral function as

$$\rho(\omega) = \frac{1}{2\pi i}\left(G_R(\omega) - G_R(\omega)^\star\right) = \frac{1}{\pi}\mathrm{Im}\left(G_R(\omega)\right). \tag{2.11}$$

So far, the correlation function has been defined in real time. To go to imaginary time as on the lattice, we relate the Euclidean correlator from (2.2) to the forward real time correlator:

$$G_H(\tau) = G^>(-it). \tag{2.12}$$

In a definite momentum projection,

$$G_H(\tau, \vec{p}) = \int \mathrm{d}x\ e^{-i\vec{p}\cdot\vec{x}} \left\langle J_H(\tau, \vec{x}) J_H^\dagger(0, \vec{0})\right\rangle, \tag{2.13}$$

we get

$$\begin{aligned} G_H(\tau, \vec{p}) &= \int \mathrm{d}^3x\ e^{-i\vec{p}\cdot\vec{x}} G^>(-it, \vec{x}) \\ &= \int \mathrm{d}^3x \int_{-\infty}^{\infty} \frac{\mathrm{d}\omega}{\pi} \int \mathrm{d}^3q\ e^{i(\vec{q}-\vec{p})\vec{6}x - \omega\tau} G^>(\omega, \vec{q}) \\ &= \int_{-\infty}^{\infty} \frac{\mathrm{d}\omega}{\pi} e^{-\omega\tau} G^>(\omega, \vec{p}), \end{aligned} \tag{2.14}$$

where we have inserted (2.9). We transform the negative part of the integration to the positive half-axis using the relation

$$G^>(-\omega) = e^{-\beta\omega} G^>(\omega). \tag{2.15}$$

In the end, we obtain the following relation between the correlator and the spectral function:

$$G(\tau) = \int_0^{\infty} \frac{\mathrm{d}\omega}{\pi} \rho(\omega) K(\omega, \tau) \tag{2.16}$$

with the integration kernel

$$K(\omega, \tau) = \frac{\cosh(\omega(\tau - \frac{1}{2T}))}{\sinh(\frac{\omega}{2T})}. \tag{2.17}$$

Extracting the spectral function is an ill-posed inversion problem. Many different solutions have been proposed, such as using a Bayesian ansatz in MEM ([20]) or SAI ([21]), gaining information by looking at a reconstructed correlator or a Taylor expansion of the midpoint (see section 2.2). One of

the main goals of this thesis will be to fit a perturbative spectral function to the correlator data and thus to combine different approaches.

In this work, we are especially interested in the pseudoscalar correlators given by

$$G_{PS}(\tau) = M_B^2 \int_{\vec{x}} \langle (\bar{\psi} i\gamma_5 \psi)(\tau, \vec{x})(\bar{\psi} i\gamma_5 \psi)(0, \vec{0}) \rangle_c \,, \tag{2.18}$$

where M_B is a bare quark mass. By including the factor M_B^2, the pseudoscalar correlator is believed to be finite after mass and gauge coupling renormalization. The vector channel correlators read

$$G_{ii}(\tau) = \int_{\vec{x}} \langle (\bar{\psi} \gamma_i \psi)(\tau, \vec{x})(\bar{\psi} \gamma_i \psi)(0, \vec{0}) \rangle_c \,. \tag{2.19}$$

As indicated by the c, we only analyze the connected (flavor non-singlet) part of the correlator, since the disconnected part is only accessible with great computational effort. Due to OZI suppression, the disconnected part is so small that its neglection is justified.

2.2 Gaining information on the correlator level

Even without extracting the spectral function, we can obtain knowlegde about how bound states and the transport contribution change with temperature. This section builds an intuition for how changes in different parts of the spectral function affect the correlator. Fig. 2.2 provides a better understanding of which parts of the spectral function influence the correlator in which τT regime. Due to the structure of the kernel (Fig. 2.3), the low frequency regime of the spectral function mostly contributes to the large τ part of the correlator. This can be made use of when analyzing the influence of the transport peak around $\omega \approx 0$.

2.2.1 Reconstructed, Midpoint-subtracted and Difference correlator

If we want to qualitatively compare how many changes occur between different temperatures, we take a look into the reconstructed correlator [22–24]

$$G^{rec}(\tau, T, T') = \int_0^\infty \mathrm{d}\omega \; \rho(\omega, T') K(\omega, \tau, T), \tag{2.20}$$

where $T' < T$. The trivial temperature dependence of the kernel is removed and by comparing the reconstructed to the original correlator we obtain a qualitative change in the spectral function from T' to T. If we want to

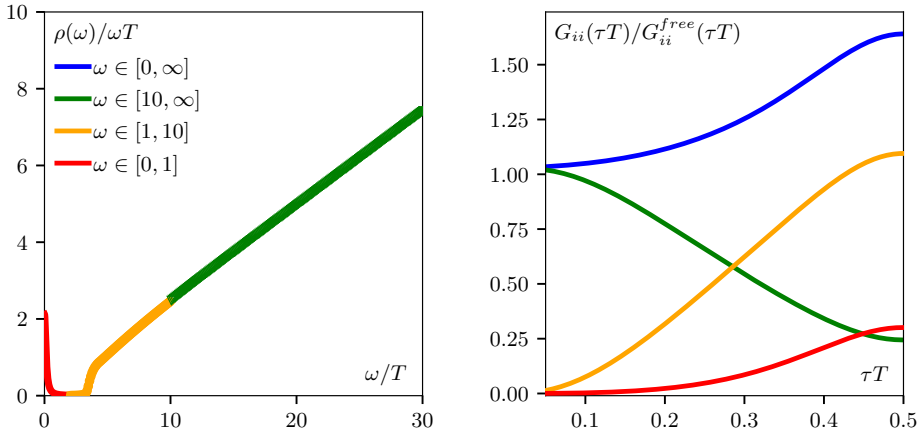

Figure 2.2: The influence of different parts of the spectral function to the different regimes of the correlator.

calculate the expression in (2.20) from our lattice data, we make use of the relation [24]

$$\frac{\cosh(\omega(\tau - N_\tau/2))}{\sinh(\omega N_\tau/2)} = \sum_{n'_\tau = n_\tau; n'_\tau += N_\tau}^{N'_\tau - N_\tau + n_\tau} \frac{\cosh\left(\omega\left(\tau' - N'_\tau/2\right)\right)}{\sinh\left(\omega N'_\tau/2\right)} \tag{2.21}$$

that holds when the temperature T is an integer multiple of T', i.e. $N'_\tau = mN_\tau$ with $m \in \mathbb{N}$. With this, the reconstructed correlator becomes

$$G^{rec}(\tau, T; T') = \sum_{n'_\tau = n_\tau; n'_\tau += N_\tau}^{N'_\tau - N_\tau + n_\tau} G\left(\tau', T'\right). \tag{2.22}$$

To estimate the effect of the transport contribution, we can take a look into the midpoint subtracted correlator

$$G^{mid}(\tau T) = G(\tau T) - G(\tau T = 0.5). \tag{2.23}$$

As the transport peak mostly influences the midpoint of the correlator, its subtraction will cancel a lot of the transport contribution and thus make it possible to investigate the higher ω region seperately. If the transport peak had the form of a δ, the midpoint subtraction would already remove all transport effects, but since in reality we mostly expect a smeared out shape, it can be more useful to use the difference of neighbouring correlators

$$G^{diff}(n_\tau) = G(n_\tau) - G(n_\tau + 1) \tag{2.24}$$

instead. In this work we will refer to this expression as the difference correlator.

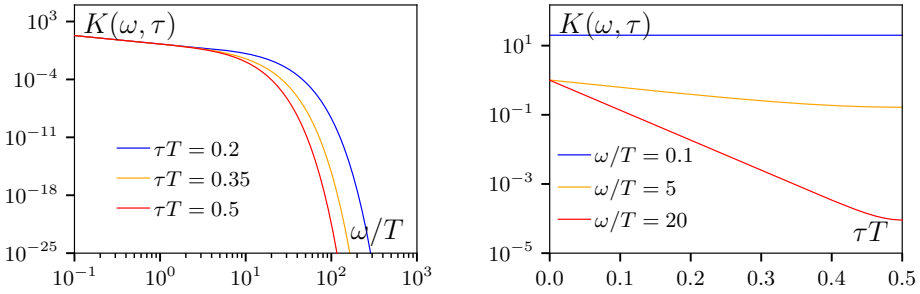

Figure 2.3: The shape of the integration kernel for different τT (*left*) and for different ω/T (*right*). It is clearly seen, that the suppression of higher ω contributions is larger for higher τT. Due to this, the lower frequencies have an higher influence on the correlator around the midpoint.

2.2.2 Thermal Moments

For an investigation of the transport peak, the correlator around the midpoint $\tau T = 0.5$ is especially interesting[1]. The Taylor expansion around this point reads [25]

$$\begin{aligned} G_H(\tau T) &= \int_0^\infty \frac{\mathrm{d}\omega}{\pi} \rho_H(\omega) \frac{\cosh(\omega(\tau - \frac{1}{2T}))}{\sinh(\frac{\omega}{2T})} \\ &\approx \int_0^\infty \frac{\mathrm{d}\omega}{\pi} \frac{\rho_H(\omega)}{\sinh(\frac{\omega}{2T})} \left(1 + \frac{1}{2!}\left(\frac{\omega}{T}\right)^2 (\tau T - 0.5)^2 + \frac{1}{4!}\left(\frac{\omega}{T}\right)^4 (\tau T - 0.5)^4\right) \\ &= G_H^{(0)} + G_H^{(2)}(\tau T - 0.5)^2 + G_H^{(4)}(\tau T - 0.5)^4 + \ldots \end{aligned} \tag{2.25}$$

with Taylor coefficients

$$G_H^{(n)} = \frac{1}{n!} \int_0^\infty \frac{\mathrm{d}\omega}{\pi} \left(\frac{\omega}{T}\right)^n \frac{\rho_H(\omega)}{\sinh(\frac{\omega}{2T})}. \tag{2.26}$$

These Taylor coefficients are the so called thermal moments and provide some insights to the curvature of the correlator around the midpoint. The zeroth moment is simply the value of the correlator at the midpoint. To avoid problems with renormalization, we build ratios

$$R_H^{n,m} = \frac{G_H^{(n)}}{G_H^{(m)}} \tag{2.27}$$

[1] Of course, the transport peak is only investigated in the vector channel, but since the following procedure is applicable to all channels, we still denote the generalized version using H to denote the channel and then set $H = ii$ later.

and use them in the expansion

$$G_H(\tau T) = G_H^{(0)} \sum_{n=0}^{\infty} R_H^{2n,0} (\tau T - 0.5)^{2n} \tag{2.28}$$

To obtain the moments from our data, we calculate the curvature

$$\Delta_H(\tau T) = \frac{G_H(\tau T) - G_H(\tau T = 0.5)}{(\tau T - 0.5)^2} \tag{2.29}$$

and express it using our ratios

$$\frac{\Delta_H(\tau T)}{G_H(\tau T = 0.5)} = R_H^{2,0} \left(1 + \sum_{n=1}^{\infty} R_H^{2n+2,2n} (\tau T - 0.5)^{2n} \right). \tag{2.30}$$

To obtain the $R_H^{2n+2,2n}$, we fit (2.30) to match our data. The approximation is valid close to the midpoint, so we should conduct the fit for the points close to $\tau T = 0.5$. But at the same time, we should not make our fit intervall too small. To find a balance between fitting a reasonable number of data points and staying close to the midpoint, we vary the lower limit $\tau_{min} T$ of the fit intervall and keep the upper bound at $\tau T = 0.5$. At some value of $\tau_{min} T$, a plateau is reached and we use the average over the plateau as our final value for the $R^{2n+2,2n}$.

2.3 Spectral functions

The methods described in the previous section help to gain a qualitative understanding of the in-medium modifications of quarkonia. To extract quantitative information, one has to look into the spectral function directly. Therefore it is useful to compare the lattice data to model spectral functions. A few of them will be presented in this section.
The spectral function consists of mainly three parts. For high energies, there is a continuum part that can be treated perturbatively, at intermediate frequencies bound states arise and at very small ω, a transport peak arises in the vector channel. The temperature dependence is schematically shown in Fig. 2.1. In the zero temperature limit, the spectral function consists of bound states described by δ peaks, that broaden, when going to higher temperatures until they eventually melt. There are many different ansätze for the spectral function and those important for this work will be presented in this section.

2.3.1 Non-interacting spectral function

In the case of two non-interacting quarks, which is reached at asymptotically high temperatures, the spectral function can be calculated analytically as

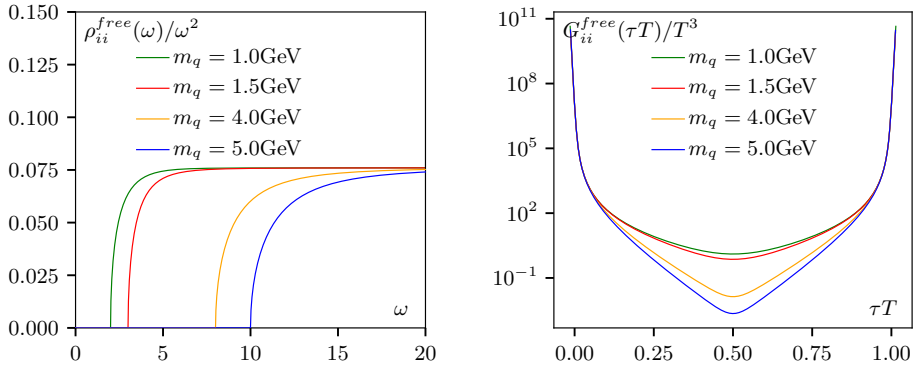

Figure 2.4: Non-interacting spectral function (*left*) and its corresponding correlator (*right*) for four different masses at an example temperature of $T \approx 1.5 T_c$.

[26]

$$\begin{aligned}\rho_{free}(\omega) =& \frac{N_C}{16\pi^2}\Theta\left(\frac{\omega^2}{T^2} - \frac{4m_q^2}{T^2}\right)\omega^2 \tanh\left(\frac{\omega}{4T}\right)\sqrt{1-\left(\frac{2m_q}{\omega}\right)^2} \\ &\cdot\left(\left(a_H^{(1)} - a_H^{(2)}\right) + \left(a_H^{(2)} - a_H^{(3)}\right)\left(\frac{2m_q}{\omega}\right)^2\right) \\ &+ \omega\delta(\omega) N_c\left[\left(a_H^{(1)} + a_H^{(3)}\right) I_1 + \left(a_H^{(2)} - a_H^{(3)}\right) I_2\right],\end{aligned} \tag{2.31}$$

with the quark mass m_q and N_c the number of colors (here $N_c = 3$). The coefficients a_H depend on the channel and can be seen in tab. 2.2. Fig. 2.4 shows an example of the free spectral function. Constructing a correlator of this spectral function leads to

$$\begin{aligned}\frac{G_{free}(\tau')}{T^3} =& \frac{3}{16\pi^2}\int_{2m_q'}^{\infty} \omega'^2 \tanh\left(\frac{\omega'}{4}\right)\sqrt{1-\left(\frac{2m_q'}{\omega'}\right)} \\ &\cdot\left(\left(a_H^{(1)} - a_H^{(2)}\right) + \left(a_H^{(2)} - a_H^{(3)}\right)\left(\frac{2m_q'}{\omega'}\right)^2\right) \\ &\cdot\frac{\cosh(\omega'(\tau' - \frac{1}{2}))}{\sinh(\frac{\omega'}{2})} d\omega'.\end{aligned} \tag{2.32}$$

This correlator is later used as a normalization for the lattice correlators to suppress the exponential fall-off and thus make the region around the midpoint more visible.

The non-interacting spectral function also provides a good example to study cut-off effects. Fig. 2.5 shows the massless spectral function calculated on different lattices compared to the analytic solution (2.31). Due to

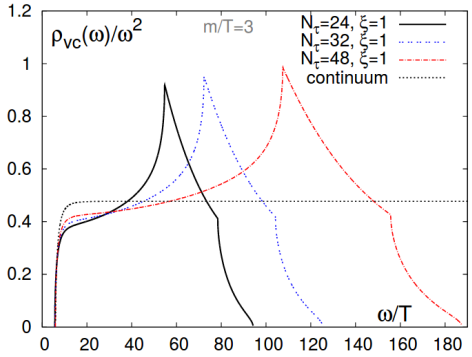

Figure 2.5: Non-interacting spectral function in the continuum and on the lattice. The discretization effects are clearly visible. Instead of becoming constant in ρ/ω^2, the lattice spectral functions show peaks and then fall off to zero. Figure taken from [25].

discretization artifacts, the lattice results show a peak that gets shifted to higher ω with increasing lattice size. It thus describes physics differently and only after taking the continuum limit, the correct solution is obtained. For a more detailled discussion see [25].

Channel	$a_H^{(1)}$	$a_H^{(2)}$	$a_H^{(3)}$
Vector			
$\rho_{\mu\mu}$	2	-2	-4
ρ_{ii}	3	-1	-3
ρ_{00}	1	1	1
Pseudoscalar	1	-1	-1
Scalar	1	-1	1
Axial Vector	2	-2	4

Table 2.2: Coefficients for G^{free} in different channels. Taken from [26].

2.3.2 Bound States

In the intermediate to higher frequency part of the spectral function, we expect bound states to arise, at least until the temperature exceeds the dissociation temperature. At $T = 0$, we expect the bound states to appear as δ-peaks in the spectral function. When increasing the temperature, they are expected to broaden. Some calculations, e.g. the NRQCD calculation in [15], suggest, that the bound state mass shifts, when going to higher temperatures, while others do not observe this.

So far, a lot of attempts have been made to estimate a spectral function. On the lattice, techniques like MEM provide insight, see [27–32]. Most of the results show a few peaks that could be interpreted as bound states, but the number and amplitude of these peaks vary from study to study. For higher frequencies, most show shapes that are similar to the non-interacting spectral function, but sometimes it is hard to distinguish between physical features of the spectral function and oscillations due to lattice artifacts. [33] discusses how MEM compares to two other popular stochastical methods, Stochastic Analytical Interference (SAI) and Stochastic Optimisation Method (SOM), and finds that the results agree well. Furthermore, the default model dependence is analyzed. It is found that while the location of peaks is not very dependent on the default model, the height and width are. MEM requires many lattice points and a high precision to produce reliable results independent from the default model. As [27, 28] mentioned, details of the spectral functions can not be resolved for high temperatures, as the lattice extent becomes too small.

Another approach is to work with potential models. Under some circumstances given by effective field theory [34], the medium effects can be characterized by a temperature dependent potential. This potential has a real part, which can be calculated on the lattice and an imaginary part that can be expressed perturbatively or with the help of LQCD. There are several studies using a real potential, e.g. [35, 36]. [16], however, finds that the imaginary part has a significant effect on the spectral functions as it is responsible for the dissolution of the charmonium 1S state and excited bottomonium states at $T \approx 250$MeV and the melting of the bottomonium bound state at $T \gtrsim 450$MeV. In total, the study finds one other charmonium S-bound state at $T = 0$, which is gone for the non-zero temperatures analyzed. For the location of the ground state peak, there is a shift to lower masses with increasing temperature. When taking the imaginary potential into account, the melting is visible. For bottomonium, the spectral function shows three bound states and one small peak that could hint to a fourth. The three clearly visible bound states melt sequentially. $\Upsilon(3S)$ is gone for the non-zero temperatures in this study, $\Upsilon(2S)$ melts above 245MeV, while the ground state persists up to 449MeV. Temperatures above this were not analyzed. The mass shift observed in charmonium spectral functions does not show for bottomonium.

In [15] analytic expressions for the real and complex potentials are found by using a generalized Gauss law ansatz. The expressions depend on a single parameter, the Debye mass, which can be determined via a fit to the real part of the potential evaluated on full QCD lattices. Fig. 2.6 shows the results for the vector spectral functions. Even though [15] presents the calculation for the vector channel, it holds information on the pseudoscalar as well since the two channels are related in the non-relativistic limit.

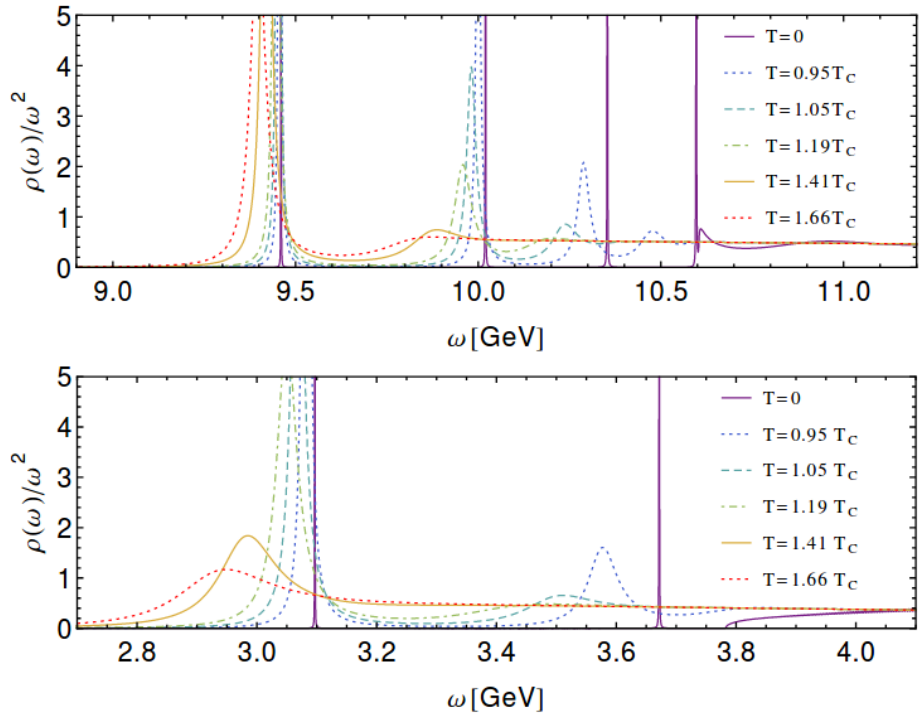

Figure 2.6: Vector spectral functions for bottomonium (*upper figure*) and charmonium (*lower figure*) obtained by the potential model study in [15]. With increasing temperature, sequential melting can be observed, as well as a shift of the peak to lower ω.

The sequential melting is confirmed in this study. The charmonium spectral functions show two bound states, $\psi(2S)$ disappearing almost at T_c and the ground state surviving up to between 1.19 and $1.41T_c$. Four bottomonium states can be observed, the highest already gone around T_c, the next highest disappearing rapidly around the same temperature, while $\Upsilon(2S)$ melts only above $1.19T_c$ and the ground state even survives up to $1.66T_c$, the highest temperature used in that study. The positions of the bound state peaks shift significantly to lower masses with increasing temperature. In contrast to [16] this is observed for charmonium and bottomonium.

2.3.3 Perturbative spectral function

As seen in the previous section, estimating a spectral function works best as a combined effort of different ansätze. For the potential model studies, LQCD and perturbation theory have been employed and the same combination can be done for MEM, if a perturbatively motivated default model is chosen. In this work, we will further explore how LQCD and perturbation theory can be

combined to gain insight into spectral functions. A major goal is to compare lattice correlators to a perturbative spectral function as done in [37, 38]. In this section, the perturbative spectral functions for vector and pseudoscalar channel will be given. Note that the expression "perturbative" in this case means a combination of perturbative and pNRQCD calculations, valid for different energy regimes. The basic idea how to construct these spectral functions is given in [39]. The matching procedure between the different energy regimes is presented in [37].

For energies well above the threshold, the spectral function can be described by ultraviolet asymptotics, which is perturbatively known up to 5-loop order, see [37, 40]. The spectral function can be written as

$$\rho_{ii}^{vac} = \frac{N_c \omega^2}{4\pi} R_{ii}^c(\omega^2), \tag{2.33}$$

in the vector channel and

$$\rho_{PS}^{vac} = \frac{M^2 N_c \omega^2}{8\pi} R_{PS,M}^c(\omega^2), \tag{2.34}$$

in the pseudoscalar channel, where we need the factor M^2 to be consistent with our definition of the correlator (2.18). We normalized the correlator with M^2 to take care of the anomalous dimension and to get a finite correlator after renormalization.

It is convenient to rewrite expression (2.34) in terms of the $\overline{\text{MS}}$ mass $m(\bar{\mu})$ instead of the pole mass M, which means leaving the on-shell scheme. This changes the coefficients in R_{PS}^c, so that there are two versions, $R_{PS,M}^c$ and $R_{PS,m}^c$. As a reference scale, we choose $\bar{\mu} = \max(\omega, \pi T)$.

With

$$l = \ln\left(\frac{\bar{\mu}^2}{\omega^2}\right), \tag{2.35}$$

R^c is given by

$$\begin{aligned} R_{PS,ii}^c(\omega^2) =& r_{0,0} + r_{1,0}\alpha_s + (r_{2,0} + r_{2,1} l)\,\alpha_s^2 \\ &+ \left(r_{3,0} + r_{3,1} l + r_{3,2} l^2\right)\alpha_s^3 \\ &+ \left(r_{4,0} + r_{4,1} l + r_{4,2} l^2 + r_{4,3} l^3\right)\alpha_s^4 + \mathcal{O}\left(\alpha_s^5\right). \end{aligned} \tag{2.36}$$

The coefficients $r_{i,j}$ are given in [37] for the pseudoscalar spectral function and in [40] for the vector channel. Since this expression is given in terms of the $\overline{\text{MS}}$ mass, it must be related to the pole mass. Therefore, one makes use of the different R_c:

$$M^2 = m^2(\bar{\mu}) \frac{R_c^m}{R_c^M}. \tag{2.37}$$

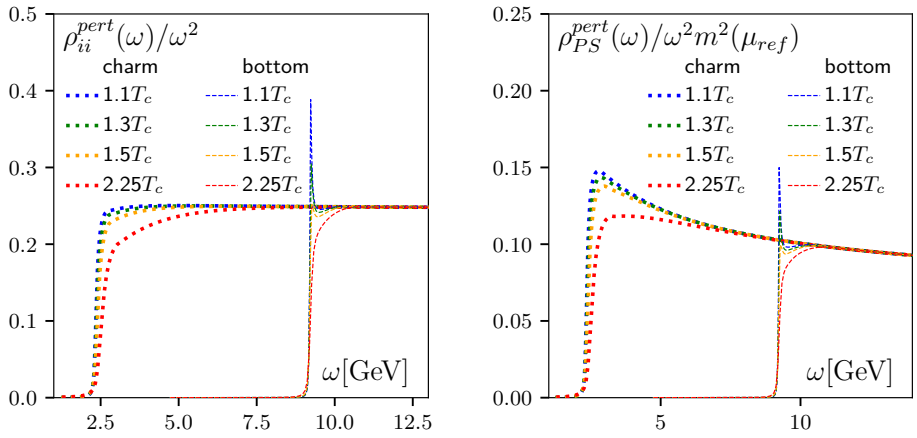

Figure 2.7: Perturbative spectral functions for charmonium and bottomonium in the vector and pseudoscalar channel.

For energies around the threshold, thermal effects arise and the physics can no longer be treated strictly perturbatively, since a perturbative expression is only available up to NLO. Instead we treat the system non-relativistically and apply pNRQCD. In the non-relativistic limit, pseudoscalar and vector channel are related via

$$\rho_{PS}^{\text{NRQCD}} = \frac{M^2}{3}\rho_{ii}^{\text{NRQCD}}. \tag{2.38}$$

ρ_{ii}^{NRQCD} has been calculated in [41, 42] in resummed hot QCD by solving

$$\rho_{ii}^{NRQCD}(\omega) = \frac{1}{2}\left(1 - e^{-\frac{\omega}{T}}\right)\int_{-\infty}^{\infty} \mathrm{d}t\ e^{i\omega T} C_>(t, \vec{0}, \vec{0}). \tag{2.39}$$

The Wightman function $C_>$ is evaluated using a real-time static potential by solving

$$\left(i\partial_t - \left(2M + V_T(r) - \frac{\nabla_{\vec{r}}^2}{M}\right)\right) C_>(t, \vec{r}, \vec{r'}) = 0, \quad t \neq 0$$
$$C_>(0, \vec{r}, \vec{r'}) = 6N_c\delta^3(\vec{r} - \vec{r'}). \tag{2.40}$$

The resulting spectral functions is valid for frequencies around the threshold region. When going to much smaller ω, the expression (2.39) overestimates the spectral function. An exponential suppression $\Phi(\omega) = \theta(2M-\omega)e^{-\frac{|\omega-2M|}{T}}$ is introduced to overcome this problem.
To combine the NRQCD regime and the vacuum asymptotics, we multiply

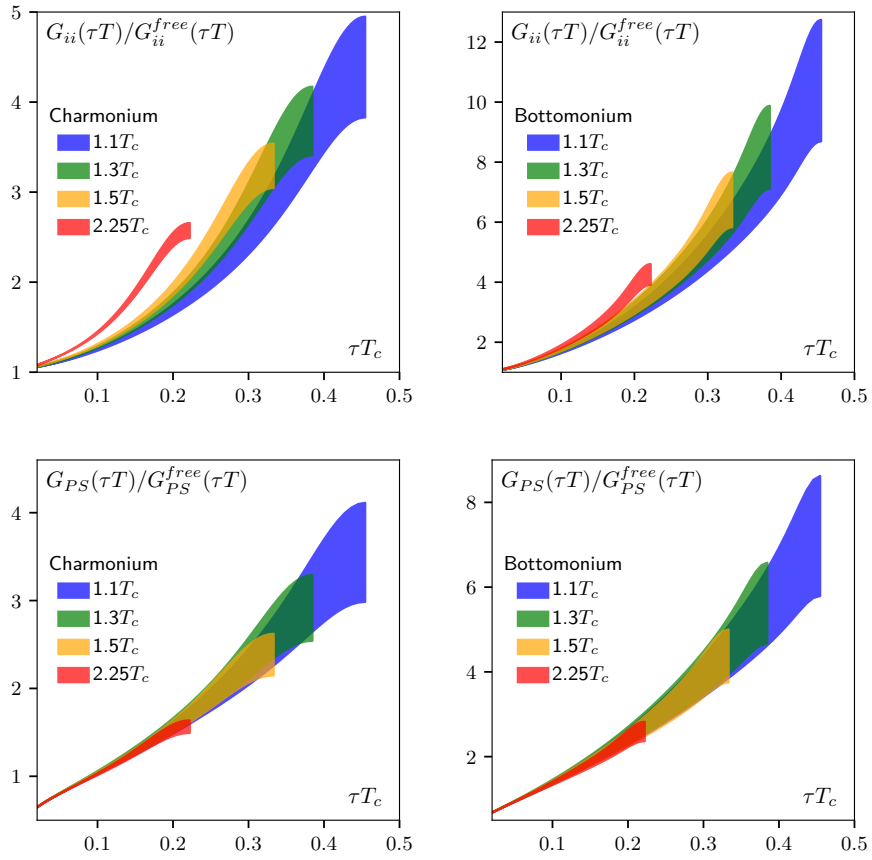

Figure 2.8: Perturbative correlators in the vector channel (*top*) and pseudoscalar channel (*bottom*). The left side shows charmonium, the right side shows bottomonium. The error bands come from varying the mass $m(\bar{\mu})$ by 10% in each direction, as the main source of systematic uncertainties in the calculation of the perturbative spectral function is the unclear relation between the $\overline{\text{MS}}$ and the pole mass.

an overall factor A^{match}, so that the two expressions connect smoothly at a matching point ω^{match}. We arrive at the final result for the spectral function:

$$\rho^{pert}(\omega) = A^{match}\Phi(\omega)\rho^{NRQCD}(\omega)\theta(\omega^{match} - \omega) + \rho^{vac}\theta(\omega - \omega^{match}). \tag{2.41}$$

Examples of these perturbative spectral functions are shown in Fig. 2.7. Inserted in (2.16) they lead to the correlators in Fig. 2.8.

2.3.4 The Spectral Function at Low Frequencies

At frequencies around zero, a transport contribution arises in the vector channel due to heavy quark diffusion. In the spectral function, this takes a form

of a narrow peak, in the correlator it gives an almost constant contribution. The interest in the transport peak stems from its connection to the heavy quark diffusion coefficient D, which can be derived by combining linear response theory with diffusive motion as done in [43]. As the transport peak is of great interest to this work, we will present the details on this as well as some calculations for the transport coefficient D in the next section.

2.4 Transport Peak

2.4.1 Relation to the Heavy Quark Diffusion Coefficient

We follow [43] and start by introducing a small, time-dependend disturbance H_{ext} to the hamiltonian of the system. The new Hamiltonian then reads

$$H'(t) = H + H_{ext}(t). \tag{2.42}$$

H_{ext} can be described by an external source h_{ext} coupling to the observable O itself:

$$H_{ext} = -\int \mathrm{d}\vec{r} A(\vec{r}) h_{ext}(\vec{r}, t) \quad \text{with} \quad h_{ext} = h(\vec{r}) e^{\epsilon t} \Theta(-t), \tag{2.43}$$

where we chose h_{ext} in such a way, that it perturbs the medium and switches off above $t = 0$ and thus creates out of equilibrium states. The expectation value of our observable at $t = 0$ is no longer zero anymore. The modified expectation value now reads

$$\langle \psi' | \, O(\vec{x}, t) \, | \psi' \rangle = \langle \psi | \, U^{-1}(t) O(\vec{x}, t) U(t) \, | \psi \rangle \tag{2.44}$$

with the time evolution operator

$$U(t) = \exp\left(-i \int_{-\infty}^{t} \mathrm{d}t' H_{ext}(t') \right). \tag{2.45}$$

To estimate the effect of the disturbance, we subtract the unperturbed expectation value $\langle \psi | \, O(\vec{x}, t) \, | \psi \rangle$. Since we only introduced a small disturbance, it is reasonable to omit non-linear terms, so that the difference between the

expectation values is given by

$$\begin{aligned}
\delta\langle O(t)\rangle &= \langle\psi'|\, O(\vec{x},t)\,|\psi'\rangle - \langle\psi|\, O(\vec{x},t)\,|\psi\rangle \\
&= \int_{-\infty}^{t} \mathrm{d}t' \,\langle\psi|\left[H_{ext}\left(t'\right), O(\vec{x},t)\right]|\psi\rangle \\
&= -i\int_{-\infty}^{t} \mathrm{d}t' \int \mathrm{d}\vec{x}' h_{ext}\left(\vec{x}',t'\right)\Theta\left(-t'\right)\langle\left[O(\vec{x},t), O(\vec{x}',t')\right]\rangle \\
&= \int_{-\infty}^{t} \mathrm{d}t' \int \mathrm{d}\vec{x}' h_{ext}\left(\vec{x}',t'\right)\Theta\left(-t'\right)\langle i\left[O(\vec{x}-\vec{x}',t-t'), O(\vec{0},0)\right]\rangle \\
&= \int_{-\infty}^{t} \mathrm{d}t' \int \mathrm{d}\vec{x}' h_{ext}\left(\vec{x}',t'\right) G(\vec{x}-\vec{x}',t-t') \\
&= \int_{-\infty}^{\infty} \mathrm{d}t' \int \mathrm{d}\vec{x}' h_{ext}\left(\vec{x}',t'\right)\Theta\left(t-t'\right) G(\vec{x}-\vec{x}',t-t') \qquad (2.46)
\end{aligned}$$

We then switch to momentum-frequency-space by making use of the Fourier decompositions

$$\delta\langle O(t)\rangle = \int \mathrm{d}\vec{k}\int \mathrm{d}\omega e^{i(\vec{k}\vec{r}-\omega t)}\delta\langle A(\vec{k},\omega)\rangle \qquad (2.47)$$

$$\Theta\left(t-t'\right)G(\vec{x}-\vec{x}',t-t') = \int \mathrm{d}\vec{k}\int \mathrm{d}\omega e^{i(\vec{k}(\vec{r}-\vec{r}')-\omega(t-t'))}G_R(\vec{k},\omega) \qquad (2.48)$$

$$h_{ext}(\vec{x}',t') = \int \mathrm{d}\vec{p}\int \mathrm{d}\alpha e^{i(\vec{p}\vec{r}'-\alpha t')}h_{ext}(\vec{p},\alpha). \qquad (2.49)$$

With this, we obtain

$$\delta\langle O(\vec{k},\omega)\rangle = G_R(\vec{k},\omega)h_{ext}(\vec{k},\omega). \qquad (2.50)$$

The retarded correlator G_R appearing here, has already been defined in (2.10) and gives the relation to the spectral function. We now define the susceptibility $\chi(\vec{k})$ via the difference of the expectation values at $t=0$

$$\begin{aligned}
\delta\langle O(\vec{k},0)\rangle &= h_{ext}(\vec{k})\int_{-\infty}^{\infty}\mathrm{d}t' e^{-\epsilon t'}G(\vec{k},t')\Theta(t') \\
&= h_{ext}(\vec{k})G_R(\vec{k},\omega=i\epsilon)|_{\epsilon\to 0^+} = h_{ext}(\vec{k})\chi(\vec{k}), \qquad (2.51)
\end{aligned}$$

so that

$$\chi(\vec{k}) = \int \frac{\mathrm{d}\omega}{\pi}\frac{\rho(\vec{k},\omega)}{\omega}. \qquad (2.52)$$

At $t > 0$, the difference of the expectation values is given by a Laplace transform of (2.46):

$$\delta \langle O(\vec{k}, z)\rangle = \int \frac{\mathrm{d}\omega}{i\pi} \frac{\rho(\vec{k}, \omega)}{\omega(\omega - z)} h_{ext}(\vec{k}) \tag{2.53}$$

$$= \frac{1}{iz}\left(\frac{G_R(\vec{k}, z)}{\chi(\vec{k})} - 1\right) \delta \langle O(\vec{k}, t = 0)\rangle \,. \tag{2.54}$$

Note that, in this last equation, the external field does not appear anymore.

To now derive a connection between the spectral function and transport coefficients from this, we need another ingredient, which is diffusive motion. Starting from the diffusion equation

$$\delta_t \langle O(\vec{r}, t)\rangle = D\nabla^2 \langle O(\vec{r}, t)\rangle \,, \tag{2.55}$$

with the diffusion coefficient D, we Fourier transform in space and Lapace transform in time and obtain the solution

$$\langle O(\vec{k}, z)\rangle = \frac{i}{z - iD\vec{k}^2} \langle A(\vec{k}, t = 0)\rangle \,. \tag{2.56}$$

We can now directly compare this solution and (2.54), which yields

$$G_R(\vec{k}, z) = \frac{iD\vec{k}^2}{z + iD\vec{k}^2}\chi(\vec{k}). \tag{2.57}$$

Since the retarded correlator is related to the spectral function via (2.11), we take the imaginary part and additionally substitute $z = \omega + i\epsilon$, so that we finally obtain the connection between the spectral function and the transport coefficient D:

$$\rho(\vec{k}, \omega) = \frac{D\vec{k}^2\omega}{\omega^2 + D^2\vec{k}^4}\chi(\vec{k}) \tag{2.58}$$

With this we arrive at a Kubo formula [44]

$$D = \frac{1}{\chi_s} \lim_{\omega\to 0} \lim_{k\to 0} \frac{\omega}{k^2}\rho(k, \omega), \tag{2.59}$$

where we defined

$$\chi_s = \lim_{k\to 0} \chi(k) \tag{2.60}$$

As already mentioned at the beginning of this chapter, the observables we are interested in are the heavy quark currents J_H, for the transport peak

especially the vector current J^μ, consisting of J^0 and J^i. According to [14], the corresponding spectral functions are related by

$$\rho^{00}(k,\omega) = \frac{k^2}{3\omega^2}\rho^{ii}(k,\omega). \tag{2.61}$$

The factor 3 is obtained by summing over the spatial components. If we insert this in the Kubo relation, we obtain

$$D = \frac{1}{3\chi_s}\lim_{\omega\to 0}\lim_{k\to 0}\frac{\rho^{ii}(k,\omega)}{\omega}. \tag{2.62}$$

for the spatial component of the vector spectral function. The susceptibility we obtain from the zero-component of the correlator is the quark number susceptibility

$$\chi_q = \int_0^{1/T} \mathrm{d}\tau G^{00}(\tau) \quad \text{with} \quad q = u,d,s. \tag{2.63}$$

2.4.2 Modelling the Transport Peak

In the previous section we already have established the connection between the transport peak and the heavy quark diffusion coefficient, but the exact shape of the low frequency spectral function is still missing. [14] models this based on Langevin dynamics and Brownian motion.

According to the equipartition theorem, the thermal momentum p of a heavy quark is of order $p \sim \sqrt{MT}$, where M is the quark mass. From this follows $p \gg T$, meaning that the time scale of heavy quark transport effects is large enough to apply the Langevin formalism [45]. The momentum of the heavy quark is then determined by the langevin equation

$$\frac{\mathrm{d}p_i}{\mathrm{d}t} = \xi_i(i) - \eta p_i, \tag{2.64}$$

where η is the drag coefficient. ξ denotes the noise function that produces random momentum kicks. Its expectation value

$$\langle \xi_i(t)\xi_j(t')\rangle = \kappa\delta_{ij}\delta(t-t') \tag{2.65}$$

is related to yet another transport coefficient, the heavy quark momentum diffusion coefficient κ. Comparing with the diffusion equation (2.55) yields the Einstein relation, which connects the two new transport coefficients η and κ to the heavy quark diffusion coefficient D via

$$D = \frac{T}{\eta M} = \frac{2T^2}{\kappa}. \tag{2.66}$$

M is the kinetic mass of the heavy quark.

After a small perturbation, the distribution of heavy quarks will equilibrate again according to

$$N(\vec{x},t) = \int \mathrm{d}^3\vec{v}' P(\vec{x}-\vec{x}',t)N(\vec{x}',0) \tag{2.67}$$

$$N(\vec{k},t) = P(\vec{k},t)N(\vec{k}',0). \tag{2.68}$$

$P(\vec{x},t)$ is the probability that a heavy quark moves a distance $\vec{x}$ in a time t given an initial velocity distribution of $\langle\vec{v}/3\rangle = T/M$. With a Gaussian distributed noise, the Langevin formalism yields that $P(\vec{x},t)$ is Gaussian

$$P(\vec{x},t) = \frac{1}{(2\pi\sigma^2(t))^{\frac{3}{2}}}\exp\left(-\frac{x^2}{2\sigma^2(t)}\right) \tag{2.69}$$

with a width of

$$\sigma^2(t) = 2Dt = \frac{2D}{\eta}\left(1-e^{-\eta t}\right). \tag{2.70}$$

Using (2.50) to establish the connection to the retarded correlator and (2.11), which relates G_R to the spectral function, we obtain a Lorentzian shape for the transport peak [14]

$$\rho_{ii}^{trans}(k=0,\omega) = 3\chi_q D\frac{\omega\eta^2}{\omega^2+\eta^2}. \tag{2.71}$$

2.4.3 Transport Coefficients from Different Methods

The transport coefficient D appearing in the low frequency spectral function in section 2.3.4 is a quantity of great interest, since it can be used as an input parameter in simulations to understand heavy ion collisions better. There have been some attempts to determine D, not only from lattice calculations, which is one of the goals of this work, but also from transport models, perturbative QCD and AdS/CFT [46]. Fig. 2.9 shows an overview of the ranges for $2\pi TD$ obtained with different methods.

Previous quenched lattice studies using MEM [51] provide values of $2\pi TD \approx 1...3$ for temperatures between 1.5 and $3T_c$. Note that, in contrast to this work, [51] does not use continuum extrapolated results.

Another property that is accessible in lattice calculations is the heavy quark momentum diffusion constant κ, which is connected to D via the Einstein relation $D = 2T^2/\kappa$ in the non-relativistic limit $M \gg \pi T$. κ can be obtained from the color-electric correlator [55]

$$G_E(\tau) = -\frac{1}{3}\sum_{i=1}^{3}\frac{\langle\mathrm{Re\ Tr}\left[U\left(\frac{1}{T},\tau\right)gE_i(\tau,\vec{0})U\left(\tau,0\right)gE_i\left(0,\vec{0}\right)\right]\rangle}{\langle\mathrm{Re\ Tr}\left[U\left(\frac{1}{T},0\right)\right]\rangle}. \tag{2.72}$$

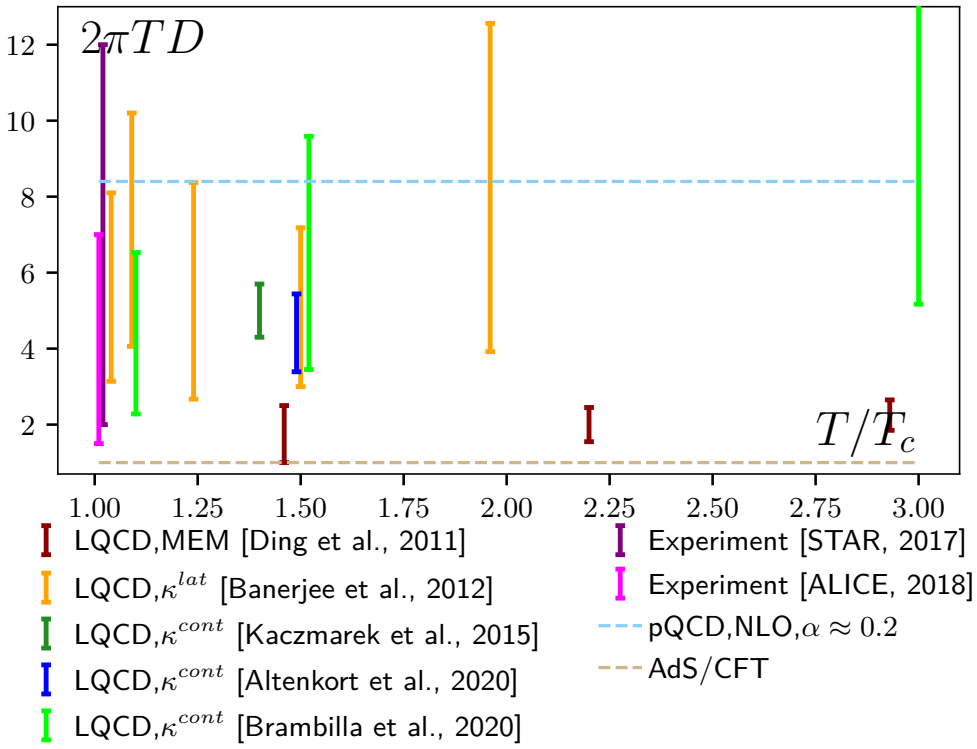

Figure 2.9: Overview over selected results for the heavy quark diffusion coefficient. The lattice results based on the heavy quark momentum diffusion coefficient κ are taken from [47–50], while the MEM result is from [51]. The perturbative NLO calculation can be found in [52] and the AdS/CFT calculation is done in [46]. The LO perturbative result is not shown, as it deviates significantly from all other calculations. The experimental values are taken from the ALICE ([53]) and STAR ([54]) collaborations. The figure clearly shows that there are large uncertainties regarding the value of $2\pi TD$, but most calculations fall in the range between 1 and 9.

Here, gE_i are the components of the color-electric field and $U(\tau_1, \tau_2)$ is a Wilson line. G_E can be calculated on the lattice. Encoded in this correlator is the spectral function $\rho_E(\omega)$ and κ is obtained from its low frequency limit

$$\frac{\kappa}{T^3} = \lim_{\omega \to 0} \frac{2\rho_E(\omega)}{\omega T^2}. \tag{2.73}$$

[47] finds κ/T^3 to be 2.5(4) at $1.4T_c$, which corresponds to $2\pi TD \approx 5$, while [56] quotes $\kappa/T^3 \approx 1.8..3.4$ leading to $2\pi TD \approx 3.7..6.9$. These are the first available continuum estimates of κ/T^3. A newer study [48] using gradient flow methods obtains $\kappa/T^3 \approx 2.31..3.70$ ($2\pi TD \approx 3.39..5.44$) at a temperature of $1.5T_c$. [49] studies a broad range of temperatures (from 1.1 to $10^4 T_c$) and finds κ/T^3 to be decreasing with increasing temperature. For the temperatures that are relevant to our work, the results range from $\kappa/T^3 = 1.91..5.4$

at $1.1T_c$ over $\kappa/T^3 = 1.31..3.64$ for $1.5T_c$ to $\kappa/T^3 = 0.63 - 2.20$ at $3T_c$. This leads to $2\pi TD = 2.33..6.58$, $2\pi TD = 3.45..9.59$ and $2\pi TD = 5.71..19.94$ correspondingly. Other studies with a similar method but on fine lattices instead of continuum data [50] lead to $2\pi TD \approx 4..10$ with no clearly seen temperature dependence. All studies on κ are carried out in the heavy quark mass limit. To compare to results obtained with physical masses, corrections of order $\mathcal{O}(T/M)$ need to be included [57].

Perturbation theory finds $2\pi TD \approx 70$ for $\alpha_s \approx 0.2$ at leading order [58] and $2\pi TD \approx 8$ at next-to-leading order [52], but as [52] suggests, convergence might be poor. AdS/CFT calculations in the strong coupling limit hint to lower values for the diffusion constant. [46, 59] obtain values around 1.

A direct experimental measurement of the heavy quark diffusion coefficient is not possible. To obtain experimental results, a comparison to transport models is needed, where the parameter of interest is tuned or fitted to match experimental observables like the elliptic flow. With this procedure, experiments estimate the heavy quark diffusion coefficient close to the critical temperature to be around $2\pi TD \approx 1.5..7$ (ALICE collaboration, [53]) or $2\pi TD \approx 2..12$ (STAR collaboration, [54]).

So far, there are large uncertainties regarding the value of $2\pi TD$ and most methods give an idea of the region in which we can expect the heavy quark diffusion coefficient to be rather than a reliable value. Since most estimates give $2\pi TD < 10$, we later compare our data to examples in this range.

The calculation that deviates significantly from the others is the perturbative one and as it is already mentioned, the result might not be reliable due to poor convergence. Perturbation theory can thus not provide an exact shape of the transport peak. A better way to treat the transport contribution perturbatively might be to apply unresummed perturbation theory which can provide an estimate of the constant part of the transport contribution. These constant contributions are calculated up to NLO in [60] together with an estimate for the quark number susceptibility (see next section). The leading order contribution is given by

$$G_{ii}^{LO}(\tau)\Big|_{const} = -4C_A \int_p \left(1 - \frac{M^2}{E_p^2}\right) T n_F'(E_p), \tag{2.74}$$

where n_F' denotes the derivative of the Fermi distribution, $C_A = N_c = 3$ and $E_p = \sqrt{p^2 + M^2}$. At NLO the constant contribution reads

$$\begin{aligned}\frac{G_{ii}^{NLO}(\tau)\Big|_{const}}{4g^2 C_A C_F} = \int_p T n_F'(E_p) \int_k \Bigg(& \frac{-3}{E_p^2}\frac{n_B(\epsilon_k)}{\epsilon_k} \\ & + \frac{n_F(E_k)}{E_k}\left(\frac{-3}{E_p^2} - \frac{M^2}{E_p^2 E_k^2} + \frac{M^2(4E_k^2 - M^2)}{2pkE_p^2E_k^2}\ln\left(\left|\frac{p+k}{p-k}\right|\right)\right)\Bigg)\end{aligned} \tag{2.75}$$

	Charmonium		Charmonium	
T/T_c	χ_q/T^2	$G_{ii}^{pert.const}/T^3$	χ_q/T^2	$G_{ii}^{pert.const}/T^3$
1.1	0.247	0.125	0.809e-04	0.155e-04
1.3	0.324	0.176	0.348e-03	0.746e-04
1.5	0.416	0.245	0.146e-02	0.354e-03
2.25	0.637	0.444	0.229e-01	0.757e-02

Table 2.3: The perturbative estimates for the quark number susceptibility and the constant part of the transport contribution from [60]. The values are also quoted here: [61]

with the group theory factor $C_F = (N_c^2 - 1)/(2N_c)$, the Bose distribution n_B and $\epsilon_k = |\vec{k}|$. The results for the perturbative transport contribution and the quark number susceptibility at the four temperatures relevant to this work are given in tab. 2.3. [60] also provides a comparison to lattice data from [25] and concludes that there is hope to resolve the transport peak with lattice methods if $2\pi TD \approx 1 - 2$ and the statistical errors of the data are small enough. If the heavy quark diffusion coefficient is higher, the task becomes more challenging.

Chapter 3

Lattice QCD - A Method To Obtain Correlators

QCD describes one of the fundamental interactions in nature, namely the strong interaction of quarks and gluons, and is thus an interesting field of research. To gain insight, we would have to solve the equations of motion from the Yang-Mills lagrangian

$$\mathcal{L} = \bar{\psi}(x)(i\gamma^\mu D_\mu - m)\psi(x) - \frac{1}{4}F^i_{\mu\nu}(x)F^{\mu\nu,i}(x), \tag{3.1}$$

where ψ is the vector of spinor fields, D_μ the covariant dericative, γ_μ the Dirac matrices and $F^i_{\mu\nu}$ the components of the field strength tensor with color index i, which can be written as

$$F^i_{\mu\nu}(x) = \partial_\mu A^i_\nu(x) - \partial_\nu A^i_\mu(x) - g f_{ijk} A^j_\mu(x) A^k_\nu(x). \tag{3.2}$$

Here, the f_{ijk} are the structure constants, g is the bare coupling constant and A^i_μ are the gauge fields.

As there are too many degrees of freedom in (3.1), an analytical solution is impossible. Instead we make use of statistical mechanics and calculate expectation values of different observables in the path integral formalism. For this, it is necessary to switch from Minkowski to Euclidean space via a Wick rotation, where we replace real with imaginary time $\tau = -it$. We then define the Euclidean action

$$S_E(\psi, \bar{\psi}, U) = \int_0^\beta \mathrm{d}\tau \int \mathrm{d}\vec{x} \left(\bar{\psi}(x)(\gamma^\mu D_\mu + m)\psi(x) + \frac{1}{4}F^i_{\mu\nu}F^{\mu\nu,i} \right), \tag{3.3}$$

where β denotes the inverse of the temperature and U are the link variables related to the gauge fields A as explained in section 3.1.1. With the path

integral measure $\mathcal{D}\phi$ for generalized fields $\phi = \psi\bar{\psi}, U$, the expectation value of any operator O can now be expressed as

$$\langle O \rangle = \frac{1}{Z} \int \mathcal{D}\psi \mathcal{D}\bar{\psi} \mathcal{D}U O e^{-S_E(\psi,\bar{\psi},U)} \tag{3.4}$$

where

$$Z(\beta) = \int \mathcal{D}\psi \mathcal{D}\bar{\psi} \mathcal{D}U e^{-S_E(\psi,\bar{\psi},U)} \tag{3.5}$$

is the partition partition function. The partition function alone can not be computed by current methods, but the whole expression (3.4) is accessible with Monte-Carlo techniques. This gives the basis to the field of Lattice QCD, which has proven to be a useful tool to gain insight into physics that is unreachable by perturbative calculations or any other approaches. In our case, the observable of interest are the correlators described previously. This chapter is dedicated to give an introduction on the method of LQCD and is based on [17]. We will also provide information on the lattices used in this work and present our method to get from lattices to continuum data.

3.1 Discretization

To evaluate (3.4) with numerical methods, we need to discretize space-time so that the path integral has finite dimenson. In lattice QCD, this is done by introducing a finite lattice spacing a to build a four dimensional lattice as shown in Fig. 3.1. The points n are called sites and correspond to fermions, while the links U connecting them represent gluons. The continuous x is now replaced with an and the Euclidean time is given by $\tau = an_\tau$. Usually all spatial extents N_σ are chosen to be equal, so that the volume of the lattice is given by $V = (aN_\sigma)^3$. In our work, a quite large number of data points is needed for reconstruction methods and we choose spatial extents of $N_\sigma = 96, 120, 144, 192$. Meanwhile the temporal extent is linked to the temperature via $T = 1/aN_\tau$. For each spatial extent N_σ we investigated four or five different N_τ, chosen in such a way that the temperatures are approximately $0.75, 1.1, 1.3, 1.5$ and $2.25T_c$. More information on these lattices is summarized in tab. 3.1.

When discretizing (3.4), we interchange the integrals by sums $\int d^4x \to \sum_n a^4$ and derivatives by difference quotients $\partial_\mu \phi \to \frac{\phi(na+\hat{\mu})-\phi(na-\hat{\mu})}{2a}$, where $\hat{\mu}$ denotes a unit vector in μ direction.

For the further discussion we split the action into two parts: The fermionic part S_F and the gauge part S_G.

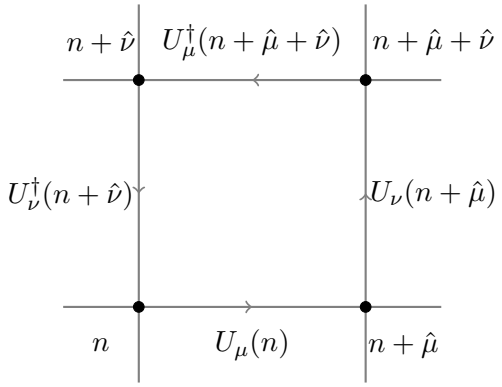

Figure 3.1: Picture of a lattice in two dimensions. The points n are the sites where fermion fields ψ are evaluated, while the links U between them are gluons. The product of the four links is called plaquette.

3.1.1 Gauge action

For the gauge action we only need the links

$$U_\mu(n) = e^{igaA_\mu(n)}. \tag{3.6}$$

These belong to the $SU(3)$ group and fulfill

$$U_{-\mu}(n) = U_\mu^\dagger(n-\hat{\mu}). \tag{3.7}$$

However, these links are not invariant under gauge transformations $\psi(n) \to \psi'(n) = \Omega(n)\psi(n)$, $\bar{\psi}(n) \to \bar{\psi}'(n) = \bar{\psi}(n)\Omega(n)^\dagger$ as in general

$$U_\mu(n) \to U'_\mu(n) = \Omega(n)U_\mu(n)\Omega(n+\hat{\mu})' \neq U_\mu(n). \tag{3.8}$$

But still, the links can be used to construct a gauge invariant object. We define the plaquette

$$U_{\mu\nu}(n) = U_\mu(n)U_\nu(n+\hat{\mu})U_\mu^\dagger(n+\hat{\nu})U_\nu^\dagger(n) \tag{3.9}$$

as a product of link variables shown in Fig. 3.1. As the plaquette describes a closed loop, the Ω in (3.8) cancel each other. The Wilson gauge action can then be expressed through plaquettes:

$$S_G(U) = \frac{6}{g^2}\sum_n \sum_{\mu<\nu} \left(\mathbb{I} - \frac{1}{3}\mathrm{Re\ tr}\left(U_{\mu\nu}(n)\right)\right). \tag{3.10}$$

To take the continuum limit $a \to 0$, we apply the Baker-Campbell-Hausdorff formula to the plaquette

$$\begin{aligned} U_{\mu\nu} = \exp(&iaA_\mu(n) + iaA_n u(n+\hat{\mu}) - \frac{a^2}{2}[A_\mu(n), A_\nu(n+\hat{\mu})]) \\ &- iaA_\mu(n+\hat{\nu}) - iaA_\nu(n) - \frac{a^2}{2}[A_\mu(n+\hat{\nu}), A_\nu(n)] \\ &+ \frac{a^2}{2}[A_\nu(n+\hat{\mu}), A_\mu(n+\hat{\nu})] + \frac{a^2}{2}[A_\mu(n), A_\nu(n)] \\ &+ \frac{a^2}{2}[A_\mu(n), A_\mu(n+\hat{\nu})] + \frac{a^2}{2}[A_\nu(n+\hat{\mu}), A_\nu(n)] + \mathcal{O}(a^3) \end{aligned} \tag{3.11}$$

and Taylor expand the fields

$$A_\nu(n+\mu) = A_\nu(n) + a\partial_\mu A_\nu(n) + \mathcal{O}(a^2). \tag{3.12}$$

With this, we arrive at the Yang-Mills action

$$\begin{aligned} S_G[U] &= \frac{6}{g^2} \sum_n \sum_{\mu<\nu} \mathrm{Re}(\mathrm{tr}(1 - U_{\mu\nu}(n))) \\ &= \frac{3a^4}{2g^2} \sum_n \sum_{\mu<\nu} \mathrm{tr}(F_{\mu\nu}(n)^2) + \mathcal{O}(a^2) \\ &\xrightarrow{a\to 0} \quad \frac{1}{2}\int_V \mathrm{d}^3x \int_0^{\frac{1}{T}} \mathrm{d}\tau \ \mathrm{tr}(F_{\mu\nu}(n)F^{\mu\nu}(n)) + \mathcal{O}(g^2) \end{aligned} \tag{3.13}$$

and have thus shown that the Wilson gauge action produces the correct continuum result.

3.1.2 Fermionic action

By applying the changes mentioned above, a naive discretization of S_F for the case of free fermions reads

$$S_F = a^4 \sum_n \bar{\psi}(n) \left(\sum_{\mu=0}^{3} \gamma_\mu \frac{\psi(n+\hat{\mu}) - \psi(n-\hat{\mu})}{2a} + m\psi(n) \right) \tag{3.14}$$

In the following, we change the notation to get rid of the factor a by rescaling the fields with $a^{\frac{3}{2}}\psi(an) \mapsto \psi(n)$ and the mass with $am \mapsto m$. To switch on interactions, we have to include the links (3.6):

$$S_F = \sum_n \bar{\psi}(n) \left(\sum_{\mu=0}^{3} \gamma_\mu \frac{U_\mu(n)\psi(n+\hat{\mu}) - U_\mu^\dagger(n-\hat{\mu})\psi(n-\hat{\mu})}{2} + m\psi(n) \right) \tag{3.15}$$

However, the naive discretization in (3.14) leads to a problem. In momentum space

$$\bar{\psi}(p) = \frac{1}{\sqrt{V}} \sum_n e^{-ipn} \bar{\psi}(n); \quad \psi(p) = \frac{1}{\sqrt{V}} \sum_n e^{ipn} \psi(n)$$
$$\text{with} \quad p_\mu = \frac{2\pi}{N_\mu} k_\mu, \quad k_\mu \in \{\frac{-N_\mu}{2} + 1, ..., \frac{N_\mu}{2}\} \tag{3.16}$$

the above formulation of the free fermion action leads to

$$S = \sum_p \bar{\psi} \left(i \sum_\mu \gamma_\mu \sin(p_\mu) + m \right) \psi(p) = \bar{\psi} M \psi \tag{3.17}$$

The fermion matrix M appearing here is the inverse of the free fermion propagator

$$G(p) = M^{-1} \propto \frac{m - \frac{i}{a} \sum_\mu \gamma_\mu \sin(p_\mu a)}{m^2 + a^{-2} \sum_\mu \sin(p_\mu a)^2} \tag{3.18}$$

In the limit $a \to 0$, this has 16 poles, where only one is the physically correct one and the other 15 are so-called doublers, additional unwanted particles. There are several methods to circumvent this problem, each with different advantages and disadvantages. The most prominent solutions are Wilson fermions [62], Ginsparg-Wilson fermions [63] and highly improved staggered quarks (HISQ, [64]). While the Ginsparg-Wilson method is the theoretically superior of the aforementioned, it comes with high computational costs and is thus not applicable to this work, where we need an extremely large number of lattice points. HISQ fermions are less computationally intensive and do not fully break chiral symmetry but at the price of introducing a new so called *taste* component to the spinor and having to control for the unphysical mixing of such tastes. Wilson fermions on the other hand break chiral symmetry, but have the advantage of low computational cost and theoretical simplicity. In this work, we thus choose clover-improved Wilson fermions explained in the following section.

3.1.3 Clover-improved Wilson fermions

The idea of Wilson in [62] was to add an extra mass term in the action that shifts the doublers to heavier masses. This term depends on the cut-off, so that it vanishes in the continuum limit. After rescaling the quark fields with $\sqrt{m+4}\psi(n) \mapsto \psi(n)$, the new action reads

$$S_F = a^4 \sum_{x,\mu} \left(\bar{\psi}_x \psi_x - \kappa \left(\bar{\psi}_x (r - \gamma_\mu) U_{x,\mu} \psi_{n+a\hat{\mu}} + \bar{\psi}_x (r + \gamma_\mu) U_{x,\mu} \psi_{x-a\hat{\mu}} \right) \right) \tag{3.19}$$

with the newly introduced *hopping parameter*

$$\kappa = \frac{1}{2am + 8}. \tag{3.20}$$

The discretization error of this action is of order a. A significant improvement can be made by adding yet another term [65]

$$S_{clover} = c_{sw} a^5 \sum_{n \in \Lambda} \sum_{\mu < \nu} \psi(n) \frac{1}{2} \sigma_{\mu\nu} \hat{F}_{\mu\nu}(n) \psi(n). \tag{3.21}$$

On the lattice, the field strength tensor takes the form of

$$\hat{F}_{\mu\nu}(n) = \frac{-i}{8a^2} \left(Q_{\mu\nu}(n) - Q_{\nu\mu} \right), \tag{3.22}$$

where the $Q_{\mu\nu}(n)$ are sums over plaquettes in the $\mu - \nu$-plane around a point n. Their shape of a four leave clover gives the name to this *clover-improvement*. In the quenched approximation used in this work, the appearing Sheikholeslami-Wohlert coefficients are determined non-perturbatively and can be interpolated using [66]

$$c_{sw} = \frac{1 - 0.656 g_0^2 - 0.512 g_0^4 - 0.054 g_0^6}{1 - 0.922 g_0^2}, \tag{3.23}$$

which is valid in the range of $0 \leq g_0 \leq 1$.

While Wilson fermions bring the advantage of theoretical simplicity and low computational cost, they come with the disadvantage of symmetry breaking, especially chiral symmetry. But since in this work we need large lattices rather than chiral symmetries as we study heavy quarks, clover-improved Wilson fermions are a good choice. To realize the large and fine lattices needed for reconstructing spectral functions, we also perform our calculations in the quenched approximation, where we omit sea quarks.

3.2 Scale setting

In order to connect our dimensionless observables Γ^{lat} to meaningful physical quantities Γ, we need a scale in units of GeV so that $\Gamma = a^{-d} \Gamma^{lat}$, where d is the dimension of the operator. The lattice spacing a can be determined from the coupling $\beta = 6/g^2$ via some considerations on the continuum extrapolation. On the one hand, the coupling has to depend on a, but on the other, the continuum limit has to be independent. These conditions make the renormalization group equation

$$a \frac{\mathrm{d}}{\mathrm{d}a} \Gamma = \left(a \frac{\partial}{\partial a} - \beta(g) \frac{\partial}{\partial g} \right) \Gamma = 0. \tag{3.24}$$

Note that $\beta(g)$ is not $\beta = 6/g^2$, but the so called β-function given by

$$\beta(g) = -a\frac{\mathrm{d}g}{\mathrm{d}a} \tag{3.25}$$

and thus relates a to the coupling. For small enough a, a perturbative solution is possible, but still leaves an undefined integration constant. Thus we instead make use of a non-perturbative scale setting. The basic idea there is to measure lattice observables whose physical values are known from experiments (e.g. masses, decay constants) and then find a relation. Several of these methods exist. We choose the Sommer scale [67] that works with the static quark potential

$$V(r) = A + \frac{B}{r} + \sigma r. \tag{3.26}$$

At the Sommer scale r_0 the slope of this potential is given by

$$r^2 \frac{\mathrm{d}V(r)}{\mathrm{d}r}\bigg|_{r=r_0} = B + \sigma r_0^2 = 1.65. \tag{3.27}$$

By determining r_0 from the lattice data for the potential, a direct relation to a physical value is obtained. This relation has been interpolated for different quenched lattices, leading to [68, 69]

$$\ln\left(\frac{r_0}{a}\right) = \left[\frac{\beta}{12b_0} + \frac{b_1}{2b_0^2}\ln\left(\frac{6b_0}{\beta}\right)\right]\frac{1 + c_1/\beta + c_2/\beta^2}{1 + c_3/\beta + c_4/\beta^2} \tag{3.28}$$

with the coefficients $b_0 = \frac{11}{(4\pi)^2}$, $b_1 = \frac{102}{(4\pi)^2}$, $c_1 = -8.9664$, $c_2 = 19.21$, $c_3 = -5.25217$ and $c_4 = 0.606828$.

To connect to physical units, we need a value for r_0. With $r_0 = 0.469(7)$fm [70] we obtain the lattice spacings in tab. 3.1.

3.3 Lattice Setup

To realize the large number of data points needed for different spectral reconstruction methods, we used the quenched approximation with Clover-improved Wilson fermions. We generated lattices with four different spacings and spatial extents from $N_\sigma = 96$ to $N_\sigma = 192$. After a thermalization time of 6000 sweeps the configurations are separated by 500 sweeps in the Markov chain, where each sweep consists of four overrelaxations and one heatbath update. The statistics of these lattices are given in tab. 3.1 together with the lattice spacing a. As the table shows, our lattices are very fine. The temporal extents from $N_\tau = 16$ to $N_\tau = 96$ correspond to five different temperatures $T \approx 0.75, 1.1, 1.3, 1.5$ and $2.25T_c$. The differences in the temperatures originate from uncertainties in the scale and have to be accounted for later (see

β	r_0/a	a[fm](a^{-1}[GeV])	N_σ	N_τ	T/T_c	# confs
7.192	26.6	0.018(11.19)	96	48	0.74	237
				32	1.12	476
				28	1.27	336
				24	1.49	336
				16	2.23	237
7.394	33.8	0.014(14.24)	120	60	0.76	171
				40	1.13	141
				30	1.51	247
				20	2.27	226
7.544	40.4	0.012(17.01)	144	72	0.75	221
				48	1.13	462
				42	1.29	660
				36	1.51	288
				24	2.26	237
7.793	54.1	0.009(22.78)	192	96	0.76	224
				64	1.13	291
				56	1.30	291
				48	1.51	348
				32	2.27	235

Table 3.1: The four different $N_\sigma^3 \times N_\tau$ lattices used for the continuum extrapolation. The lattice spacing a stems from Wilson-loop expectation values with $r_0 = 0.469(7)$fm [70]. With the relation $r_0 T_c$=0.7457(45) from [68], we obtain the temperature in units of T_c. On each lattice, the correlators for five to six different κ-values have been measured, see tab. 3.2.

section 3.6). On each of the lattice spacings, we examined up to six κ values corresponding to vector meson masses in the region of the J/ψ and Υ mass. The masses are measured with the many-state-fit method described in [71] and shown in tab. 3.2 and Fig. 3.2. As it can be seen, the masses of the different lattices do not exactly match each other nor the physical masses. A major task described in section 3.6 will thus be to interpolate the correlators between different κ values.

In contrast to other works, we will not work directly on the correlators calculated on these lattices, but with continuum extrapolated results. For the extrapolation we closely follow the procedure in [71], which is an update of the method presented in [72]. We start with the renormalization of the lattices (section 3.5), then interpolate between different masses to obtain the correlators at the physical J/ψ and Υ masses (section 3.6) and in the end extrapolate to the continuum using a spline interpolation (section 3.7).

β	κ	m_V[GeV]	β	κ	m_V[GeV]
	0.13194	3.21(1)		0.132008	3.38(2)
	0.1315	3.59(1)		0.1315	3.94(2)
	0.131	4.01(1)	7.394	0.131	4.47(2)
7.192	0.13	4.81(1)		0.129	6.50(2)
	0.128	6.34(1)		0.124772	10.04(1)
	0.12257	10.11(1)			
	0.13236	3.06(2)		0.13221	3.37(1)
	0.1322	3.28(1)		0.13209	3.59(1)
	0.1318	3.82(2)		0.13181	4.11(1)
7.544	0.131	4.86(2)	7.793	0.13125	5.11(1)
	0.1295	6.70(2)		0.13019	6.92(1)
	0.12641	10.23(2)		0.12798	10.42(1)

Table 3.2: κ-values and the corresponding vector meson masses m_V for each lattice. The results for m_V are determined using many-state fits to spatial correlators at $0.75T_c$. From this table it can already be seen that the measured masses are distributed around the J/ψ and Υ masses but do not exactly match one of them.

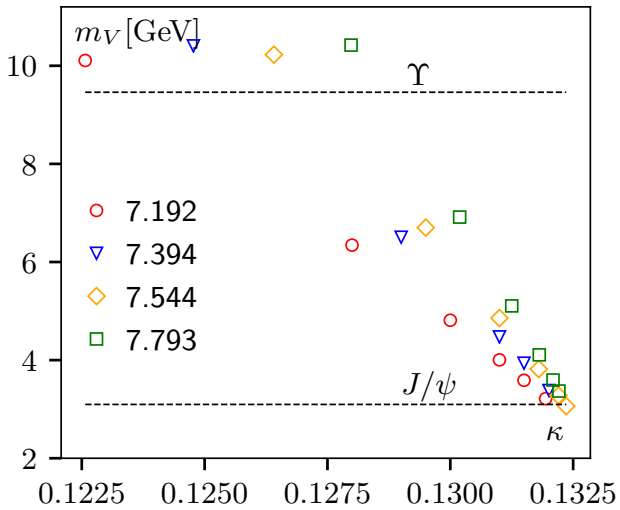

Figure 3.2: The vector meson masses for different values of κ. The dashed lines represent the physical masses of J/ψ and Υ. It can be seen that the measured masses are close to the physical masses, but do not exactly match. To overcome this, we interpolated the correlators between the different masses as shown in Fig. 3.3.

3.4 Analysis of Statistical Errors

Our lattices consist of several configurations that are generated using Markov chains. As each of these configurations are based on the previous one, they are not independent but correlated. To reduce correlations, we skip some of the configurations in between but not enough to assume uncorrelated data. Thus, we can not rely on the standard deviation as it would underestimate the statistical error. To still be able to perform an an error analysis, we make use of the bootstrap method.

Bootstrapping relies on randomly chosen samples. Given a data set of size N for an observable O, we construct M different samples of size N by randomly drawing data points from our set. Some points will be drawn more than one time, others not at all. The observable of interest is now calculated on every sample, leading to M different values O_m. The expectation value $\tilde{O}$ is then given by the average of the O_m and its error is given by the standard deviation

$$\sigma_O = \sqrt{\frac{1}{M}\sum_{m=1}^{M}(O_m - \tilde{O})^2}. \tag{3.29}$$

To get an estimate on the statistical errors, the whole continuum extrapolation is carried out on bootstrap samples. The further investigation of our data in the following chapters is also done on bootstrap samples. Only in the end we average to get our final result.

As for our observables (meson correlators) the neighbouring lattice points are correlated on each configuration, the final correlators will also show correlations. Again, bootstrapping can be applied to resolve this. For some methods, especially for MEM, a covariance matrix

$$C_{ij} = \frac{1}{N(N-1)}\sum_{k=1}^{N}\left(y_{i,k} - \bar{y_i}\right)\left(y_{j,k} - \bar{y_j}\right) \tag{3.30}$$

is required to account for these cross-correlations. Unfortunately, the bootstrap required for the continuum extrapolation destroys the covariance matrix. While the diagonal elements C_{ii} associated with the error ΔG_i remain reliable, the off-diagonal elements suffer from numerical errors. Instead of the continuum covariance matrix we thus use the covariance matrix from the finest lattice and rescale it to the continuum limit via

$$C_{ij}^{res} = C_{ij}^{lat}\sqrt{\frac{\Delta G_i^{cont}\Delta G_j^{cont}}{\Delta G_i^{lat}\Delta G_j^{lat}}}. \tag{3.31}$$

3.5 Renormalization

Befor going towards the continuum limit, we have to consider that the discretization acts as a regulator and thus renormalization is needed. Currents of the form

$$J_H(\tau,\vec{x}) = \bar{\psi}(\tau,\vec{x})\Gamma_H\psi(\tau,\vec{x}) \tag{3.32}$$

are renormalized as

$$J_H^{ren} = 2\kappa Z_H J_H \tag{3.33}$$

with the renormalization constants Z_H that can either be calculated perturbatively or, in the case of vector and axial vector channel, non-perturbatively. The perturbative renormalization constants are available up to two-loop order [73].

3.5.1 Non-perturbative Renormalization Constants and Renormalization Independent Ratios

For the vector channel the renormalization constants have been calculated non-perturbatively and interpolated in [74].

$$Z_V^{m=0}(g^2) = \frac{1 - 0.7663g^2 + 0.0488g^4}{1 - 0.6369g^2}. \tag{3.34}$$

To include the mass dependence in the renormalization prescription, the mass correction was interpolated with

$$b_V(g^2) = \frac{1 - 0.6518g^2 - 0.1226g^4}{1 - 0.8467g^2}. \tag{3.35}$$

The massive renormalization constants are then given by

$$Z_V^{massive}(g^2,\kappa) = Z_V^{m=0}(g^2)\left(1 + b_V(g^2)am_q\right). \tag{3.36}$$

This is valid for $6 \leq \beta \leq 24$, so the lattices used in this work lie within this range. (3.36) is only valid for small am_q. The renormalization constants are given in the appendix.

In this work, we use non-perturbative renormalization constants for the continuum extrapolation of the quark number susceptibility. As a test we also extrapolate the spatial vector correlator with these constants, but for continuum results that are used in the rest of this work, we apply another method. Since G^{00} and G_{ii} are renormalized in the same way, we build a renormalization independent ratio of the correlator and χ_q' at a fixed temperature $T' = 2.25T_c$, where this quantity is believed to be most reliable. Since we are also interested in the χ_q at other temperatures, we also extrapolate the ratios $\chi_q T'^2/\chi_q' T^2$. In this way, some results can already be obtained without ever using the renormalization constants and thus we avoid additional uncertainties.

3.5.2 Perturbative Renormalization Constants

Unfortunately the non-perturbative formula does not work in the pseudoscalar case, so that a perturbative calculation is needed. For clover-improved Wilson fermions at vanishing mass, the one-loop renormalization constants are given by [75]

$$Z_H = 1 - \frac{g^2}{16\pi^2} C_F(\gamma_\mathcal{O} \ln(a\mu) + B_\mathcal{O}), \tag{3.37}$$

where $\gamma_\mathcal{O}$ is the anomalous dimension, $B_\mathcal{O}$ the finite part of the renormalization constant and $C_F = \frac{4}{3}$. $\gamma_\mathcal{O}$ and $B_\mathcal{O}$ are given in [76].
When comparing perturbatively and non-perturbatively calculated renormalization constants in the vector channel, where both versions exist, huge differences are found. To improve the perturbative calculation, the tadpole formulation is introduced. With u_0 being the fourth root of the plaquette expectation value it reads [77]

$$Z_H = u_0(g^2) \left(1 - \frac{g_P^2}{16\pi^2} C_F(\gamma_\mathcal{O} \ln(a\mu) + B_\mathcal{O} - \pi^2)\right). \tag{3.38}$$

u_0 is given in the appendix. The tadpole-improved coupling g_P is often replaced by $g_{\overline{\text{MS}}}$. This coupling is derived from the coupling in the potential scheme, g_V, given by [76]

$$-\ln(u_0^4) = \frac{C_F g_V^2(\mu^\star)}{4} \left(1 - \frac{g_V^2(\mu^\star)}{4\pi} \left(\frac{11 N_c}{12\pi} \ln\left(\frac{6.7117}{\mu^\star a}\right)^2\right)\right) + \mathcal{O}(g_V^6(\mu^\star)). \tag{3.39}$$

Choosing the scale to be $\mu^\star = \frac{3.4018}{a}$ gives the best matching. Together with the relation $\Lambda_{\overline{\text{MS}}} = 0.6252 \Lambda_V$ and

$$g^{-2}(a) = 2\beta_0 \ln\left(\frac{1}{a\Lambda}\right) + \frac{\beta_1}{\beta_0} \ln\left(2 \ln\left(\frac{1}{a\Lambda}\right)\right), \tag{3.40}$$

where β_0 and β_1 are renormalization independent constants, g_V is used to evaluate the coupling in the $\overline{\text{MS}}$ scheme.

In two-loop order, the renormalization constants can be written as

$$Z_H^{bare}(g^2, a\mu) = 1 + \frac{g^2}{16\pi^2}(-\gamma_\mathcal{O} \ln(a\mu) + z_1) + \left(\frac{g^2}{16\pi^2}\right)^2 (l_1 \ln(a\mu)^2 + l_2 \ln(a\mu) + z_2) \tag{3.41}$$

with the coefficients l_1, l_2, z_1, z_2 from [78, 79]. To introduce tadpole improvement to this expression, the plaquette expectation value needs to be expanded

in g.

$$u_0 = 1 + r_1 \frac{g^2}{16\pi^2} + r_2 \left(\frac{g^2}{16\pi^2}\right)^2 + \mathcal{O}\left(g^6\right) \tag{3.42}$$

$$= 1 + r_1 \frac{g^2_{LAT}}{16\pi^2} + /r_2 - 16\pi^2 r_1 p_1) \left(\frac{g^2_{LAT}}{16\pi^2}\right)^2 + \mathcal{O}(g^6_{LAT}). \tag{3.43}$$

Inserting this into (3.41) leads to the final expression for the two-loop tadpole-improved renormalization constants for Clover-improved Wilson fermions [77].

$$\begin{aligned} Z_H(g^2_{LAT}, a\mu) = u_0(1 + \frac{g^2_{LAT}}{16\pi^2}(-\gamma_{\mathcal{O}} \ln(a\mu) + z_1 + C_F\pi^2) \\ + \left(\frac{g^2_{LAT}}{16\pi^2}\right)^2 (l_1 \ln(a\mu)^2 + (l_2 + 16\pi^2 p_1 \gamma_{\mathcal{O}}) + r_1 \gamma_{\mathcal{O}} \ln(a\mu)) \\ + z_2 - r_2 - 16\pi^2 p_1(z_1 - r_1) + r_1^2 - r_1 z_1) + \mathcal{O}(g^6_{LAT})). \end{aligned} \tag{3.44}$$

In the vector channel, the one-loop perturbative renormalization constants are in good agreement with the non-perturbative constants that are believed to be more reliable. The two-loop renormalization constants differ and can be used to estimate one source of systematic errors.

In the pseudoscalar channel, we need to include an additional factor Z_5 in the renormalization to get the same anomalous dimension as the scalar density. According to [80] this factor is given by

$$Z_5 = 1 - \frac{g^2 C_F}{2\pi^2} + \frac{g^4 C_F}{128\pi^4} \frac{N_c + 2N_f}{9} + \mathcal{O}\left(g^6\right) \tag{3.45}$$

3.6 Mass Interpolation

As Fig. 3.2 shows, the measured vector meson masses do not directly match the physical J/ψ and Υ masses. Also, the temperatures in tab. 3.1 are close but not exactly the same. After the renormalization, we thus need to ensure that the correlators from the different lattices show physics at the same mass and temperatures. Therefore, we interpolate the results from different values of κ in the vector meson mass to the physical J/ψ and Υ masses by fitting every point in τT to a quadratic exponential ansatz

$$\frac{G_{ii}\left(\tau T, \frac{m_{q\bar{q}}}{T}\right) T'^2}{T^3 \chi_q} = \exp\left(p\left(\frac{m_{q\bar{q}}}{T}\right)^2 + q\frac{m_{q\bar{q}}}{T} + r\right). \tag{3.46}$$

with the three fit parameters p, q and r. As the three examples on the right of Fig. 3.3 show, this ansatz describes the data reasonably well. A linear

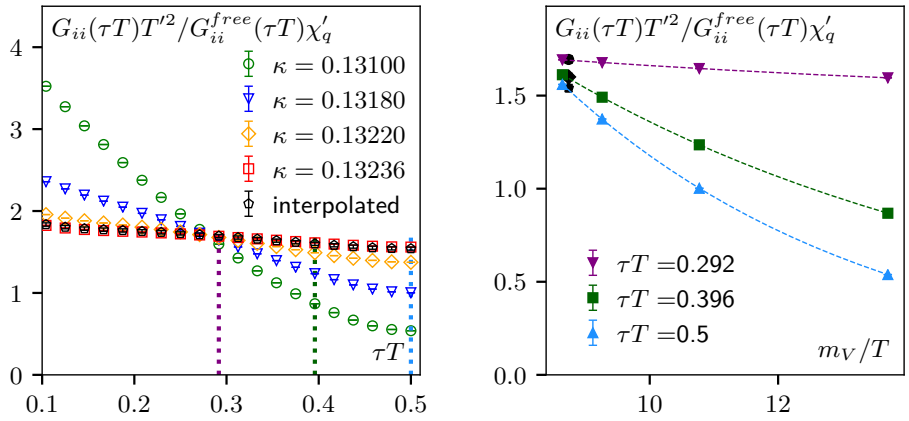

Figure 3.3: The correlators for different values of κ on a $144^3 \times 48$ lattice (*left*). For each point in τT, we interpolate with a quadratic exponential ansatz in the mass to arrive at the interpolated correlator (black) that is then used for the continuum extrapolation. For the three distances marked with the dashed lines, the interpolation to the physical J/ψ mass is shown in detail (*right*). As it is seen there, the ansatz (3.46) matches the data well.

function in the exponential was also tried and even though the results were similar, the quadratic exponential matches the data points better in some cases. We fit the four correlators with the masses closes to J/ψ and Υ respectively and obtain a mass interpolated correlator (like the one depicted with black dots in Fig. 3.3) for every lattice size and temperature. These are the basis for the following extrapolation.

3.7 Continuum Extrapolation

In a next step we need to interpolate between the distances in τT and extrapolate to the continuum. In an improved version of the algorithm in [72], these two steps are combined [71]. To perform the interpolation we make use of splines given by [81]

$$p(x) = \sum_{n=0}^{d} a_n (x - x_0)^n + \sum_{k=0}^{n} c_k (x - x_k)_+^d, \tag{3.47}$$

where

$$(x)_+ = \begin{cases} 0 & x \leq 0 \\ x & x > 0 \end{cases} . \tag{3.48}$$

The coefficients a_n and c_n are obtained by fitting the spline to the correlator. Instead of extrapolating the interpolated correlator, we extrapolate the

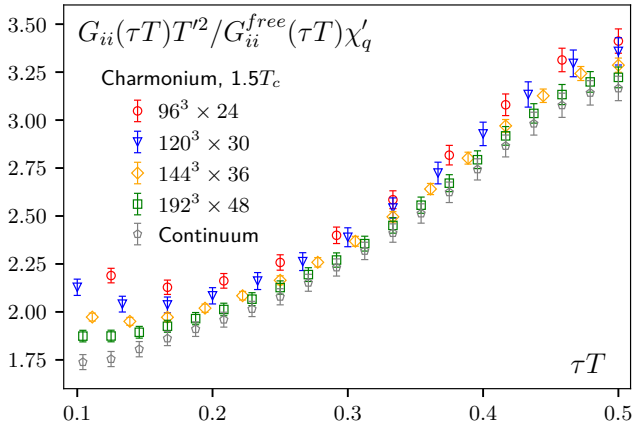

Figure 3.4: Continuum extrapolation of the mass-interpolated correlators from different lattices to the continuum (grey). The coarser lattices are interpolated with a spline and the spline coefficients are extrapolated and then used to build the continuum correlator.

spline coefficients with an ansatz quadratic in the lattice spacing, which is an acceleration and an improvement compared to the algorithm presented in [72]. Fig. 3.4 shows an example of the extrapolation of four different mass-interpolated correlators to the continuum.

This is the final step on the way from the lattice data in 3.3 to the continuum correlators that will be analyzed in the following chapters of this thesis. The whole procedure consists of renormalization, mass interpolation and the combined step of b-spline interpolation and continuum extrapolation, where each of these steps is performed on the individual bootstrap samples, which are later averaged to give a final result. Fig. 3.5 summarizes the method, which is the basis for every analysis in the following chapters. Though this method has been used for quenched lattices in this work, it could easily be extended to full QCD.

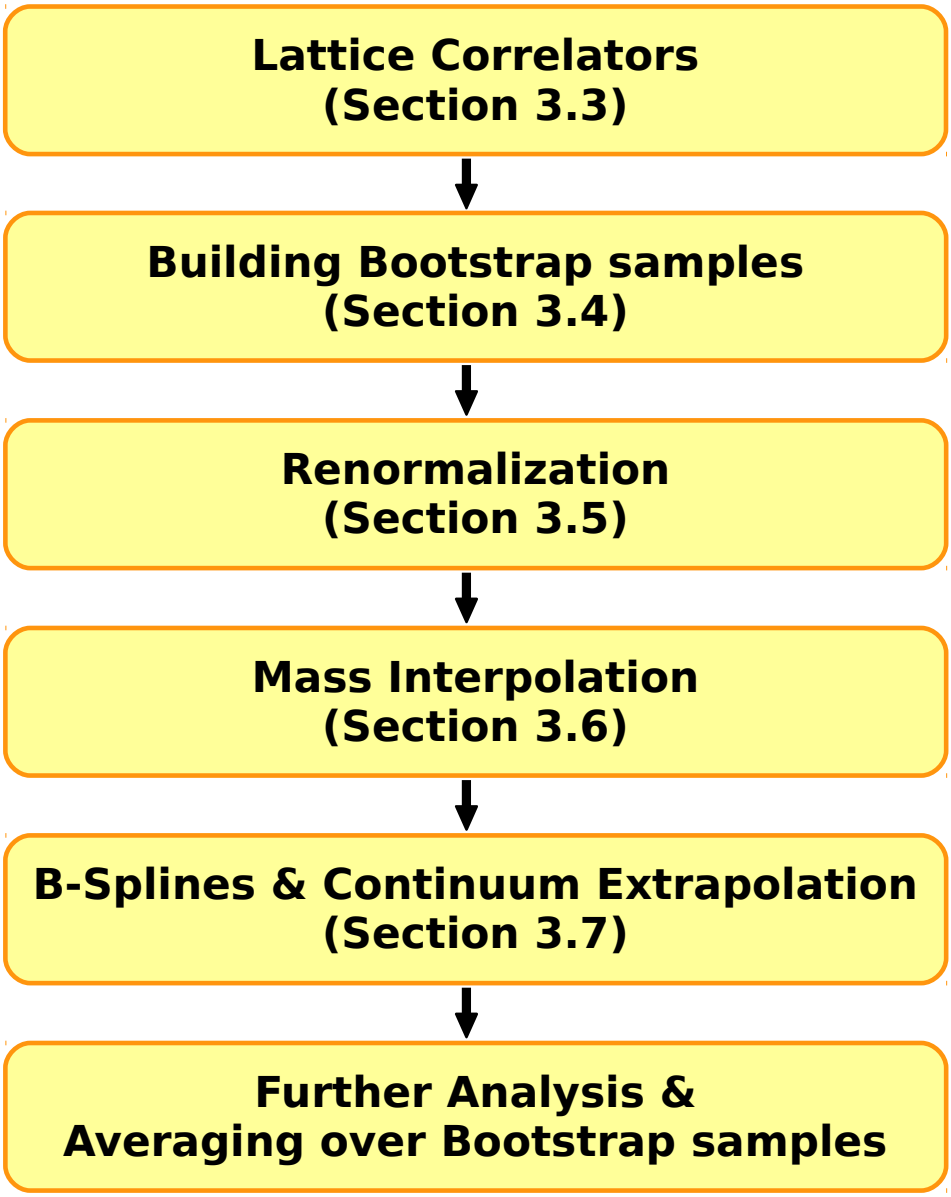

Figure 3.5: The method to obtain continuum correlators.

Chapter 4

Heavy Quarkonium Correlators and Their Comparison to a Perturbative Spectral Function

From the lattices described in the previous chapter, we obtain the continuum correlators in Figs. 4.1,4.2. Fig. 4.1 shows charmonium and bottomonium in the pseudoscalar channel at five different temperatures, one below the critical temperature ($0.75T_c$) and four above (1.1,1.3,1.5 and $2.25T_c$). For both quarkonia, the correlators show only little temperature dependence and have a very similar shape at all T. Within the statistical errors obtained from the bootstrap analysis (see section 3.4), they overlap.

The vector correlators in Fig. 4.2 are normalized with the quark number susceptibility at a reference temperature of $T' = 2.25T_c$. A more detailled explanation regarding χ_q is provided in section 4.2. In contrast to the pseudoscalar correlators, the vector channel exhibits a clear temperature dependence, especially for charmonium. While the correlators agree at small τ, the deviations grow when going to higher τ, with smaller temperatures rising more steeply.

We can already draw some first conclusions regarding the different parts of the spectral function described in chapter 2.3. Reminder: As seen in Fig. 2.2, the low frequency spectral function corresponding to the transport peak (see section 2.4) has a higher influence at high τ, while high frequencies describing the ultraviolet asymptotics (see section 2.3.3) dominate the correlator at small τ.

In the pseudoscalar channel the temperature dependence is much smaller

than in the vector channel. Since the main difference between these channels is the appearance of the transport peak, this could be an indication that a lot of the temperature dependence originates from this peak. The fact that the deviations between correlators grow with τ, just as the influence of the transport peak, seconds this. In contrast, the ultraviolet asymptotic part of the spectral function, mostly dominant in the small τ regime, does not seem to undergo significant changes when increasing the temperature. Compared to bottomonium, charmonium correlators in the vector channel show a stronger temperature dependence around the midpoint. This is not the case in the pseudoscalar channel. Thus this might be a first hint that charmonium's transport contribution is higher and more temperature dependent.

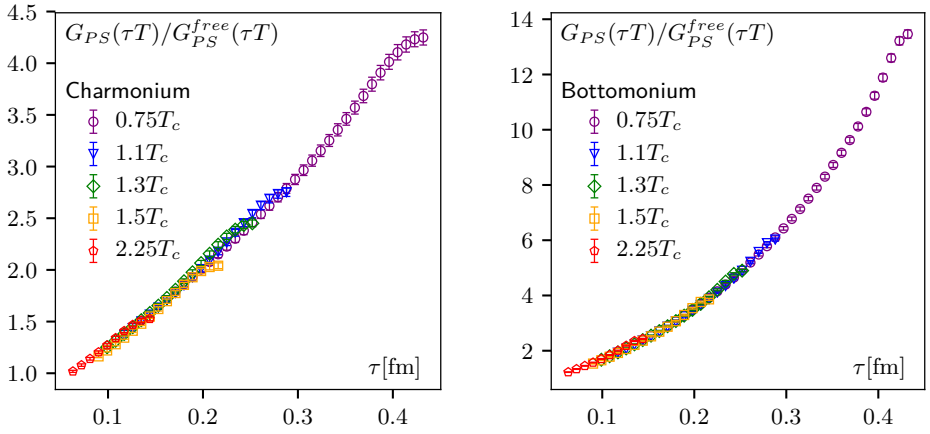

Figure 4.1: The continuum extrapolated charmonium (*left*) and bottomonium (*right*) correlators at different temperatures in the pseudoscalar channel.

A first look at Fig. 4.1 and Fig. 2.8 reveals a qualitatively good agreement between the shape of our lattice correlators and the correlators calculated from a perturbative spectral function presented in section 2.3.3. To find a more quantitative description, systematical uncertainties need to be adressed. We identified two major sources of possible errors.

On the lattice side, the renormalization constants used in the continuum extrapolation (see section 3.5) might be off. We accounted for this by introducing an overall normalization factor A to our spectral function.

On the perturbative side, uncertainties stem from the unclear relation between the pole mass and the $\overline{\text{MS}}$ mass used in the calculation of the perturbative spectral function. Thus, the spectral function might be shifted in the mass. To account for this, we introduced a mass shift B.

With these two corrections, we obtain a model spectral function

$$\rho^{mod} = A\rho^{pert}(\omega - B) \tag{4.1}$$

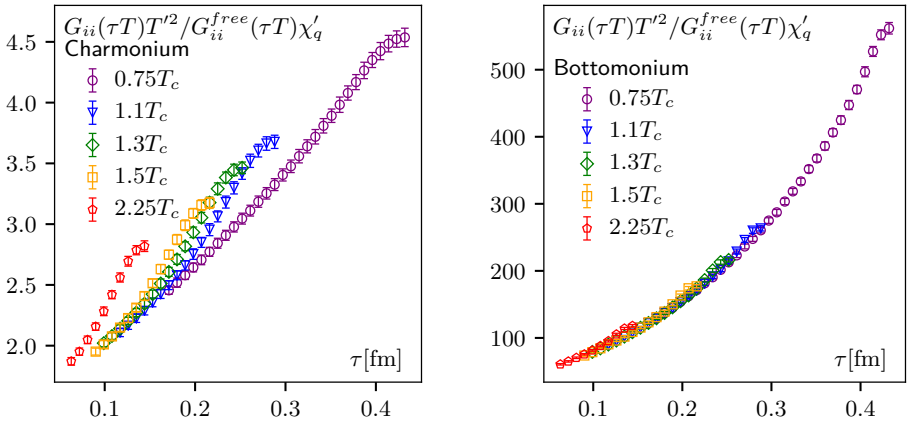

Figure 4.2: The continuum extrapolated charmonium (*left*) and bottomonium (*right*) correlators at different temperatures in the vector channel. As normalization we chose the quark number susceptibility at a temperature of $T' = 2.25T_c$.

leading to the model correlator

$$G^{mod}(\tau T) = \int_0^\infty \frac{\mathrm{d}\omega}{\pi} A\rho^{pert}(\omega - B)K(\omega, \tau) \tag{4.2}$$

A and B can now be determined by a fit of this correlator to our lattice data. The result can be used as an estimate for the agreement between perturbative description and lattice correlators. If A is close to 1 and B is around 0, our systematic uncertainties are small and our model is suited to describe the correlators.

We will apply this method to pseudoscalar and vector correlators. For the first channel, this is relatively straightforward, while the rise of the transport peak in the latter requires some more steps in the analysis. In both channels our results are then crosschecked with the maximum entropy method (MEM,[20]). Therefore, we use our fit results as a default model. If our model already describes the data well, we expect MEM to reproduce it except for small changes due to artifacts and uncertainties in the rescaled covariance matrix needed for MEM.

4.1 Pseudoscalar Channel

We first applied this fit method to the pseudoscalar channel. In [37] this led to good results, but since the fit there was conducted on the bootstrapped means of the correlators, we were not able to give a reliable error analysis. In this work we perform the fit on every bootstrap sample and only average

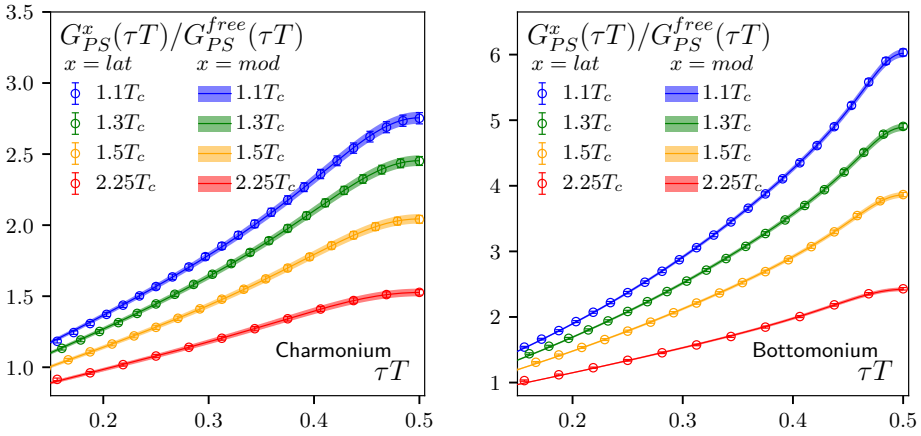

Figure 4.3: Fits to the lattice correlators.

in the end[1]. Thus we can now provide errors for our parameters A and B shown in tab. 4.1. Additionally we chose a slightly different fit range. In [37], the fit interval starts at $(\tau T)_{min} = 0.15$, while this work uses $(\tau T)_{min} = 0.2$ to further exclude the unreliable data points at small temporal distances. Our improved fits confirm the previous findings. Even though, the results from this work (tab. 4.1) and from [37] (tab. 4.2) do not always exactly agree, the tendencies and the corresponding conclusions are the same. A is around 1 and B is small. The resulting correlators in Fig. 4.3 match the data almost perfectly. The two examples in Fig. 4.4 show the comparison of lattice data, perturbative correlator and fit more closely. We conclude that our model spectral function agrees well with our lattice data with only slight modifications. The crosscheck with MEM leads to almost no changes in our results which is an additional sign that our model spectral function is a good description for our data.

Fig. 4.5 shows the model spectral functions in comparison to the perturbative spectral functions. For charmonium there is no need for an additional resonance peak at any of the analyzed temperatures, meaning that η_c dissociates rapidly above the critical temperature, which is a difference to the findings from potential models [15, 16]. For bottomonium on the other hand, we observe one resonance peak that persists up to $1.5T_c$. This peak gets thermally broadened with increasing temperature. This confirms the findings of many other studies predicting a melting of the bottomonium ground state around this temperature. Even though our mass shift B would allow the

[1]Instead of bootstrapping, we also tried correlated fits with the rescaled covariance matrix explained in 3.4. The results are similar, but the errors are overestimated. We thus choose to focus on the bootstrap method in this analysis.

	Charmonium		Bottomonium	
T/T_c	A	B/T	A	B/T
1.1	1.06(1)	0.60(2)	0.84(1)	-0.06(1)
1.3	1.05(1)	0.41(2)	0.85(1)	-0.12(2)
1.5	1.02(1)	0.34(2)	0.84(1)	-0.14(2)
2.25	1.03(1)	0.11(3)	0.88(1)	-0.14(2)

Table 4.1: Modifications to the perturbative spectral function in the pseudoscalar channel. A and B are obtained by fitting the correlator with our model spectral function (4.1).

	Charmonium		Bottomonium	
T/T_c	A	B/T	A	B/T
1.1	1.04	0.52	0.85	-0.11
1.3	1.04	0.37	0.87	-0.13
1.5	1.02	0.33	0.87	-0.11
2.25	1.06	0.16	0.93	-0.04

Table 4.2: Previous results for A and B as presented in [37]. As the first fit was performed without considering the correct statistical uncertainties, we do not quote errors here. The main differences of [37] and this work are the bootstrap analysis and the smaller fit range ($(\tau T)_{min=0.15}$ vs $(\tau T)_{min=0.2}$). Even though the new results in tab. 4.1 do not always match the parameters in this table exactly, the statement remains the same. A is close to 1 and B is small.

location of the resonance to vary for different temperatures, the maximum is found to be at the same point in ω. In this aspect, our results differ from the study of lattice potentials in [15] that obtained a mass shift. The maximum of our peak is located at $\omega \approx 9.26(2)$GeV, which is close to the PDG value of $m_{\eta_b} = 9.399(2)$.

Note that we worked in the quenched approximation, which is believed to agree better with perturbation theory. Still, the unexpectedly high agreement is a good sign that our model spectral functions are suitable to describe charmonium and bottomonium in the pseudoscalar channel.

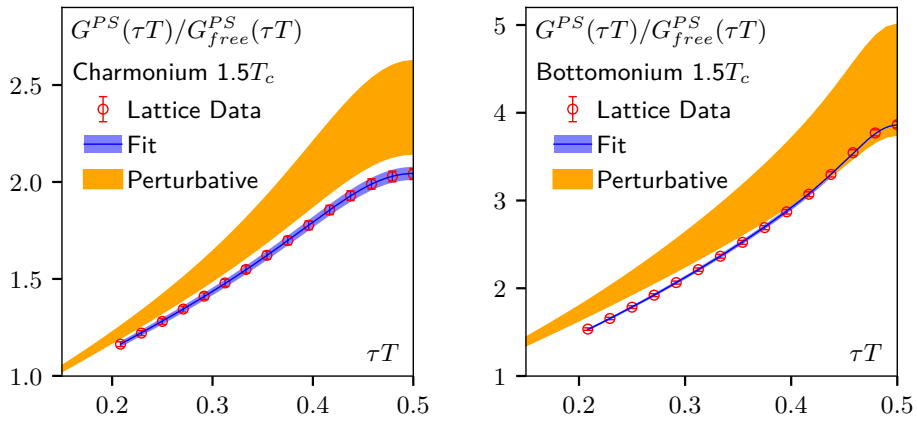

Figure 4.4: Example of the fit to the lattice data at $1.5T_c$. The orange band shows the original perturbative correlator, where the errors are estimated by varying the mass by 10%. The blue curve showing the modified spectral function obtained from our fit matches the data points almost perfectly.

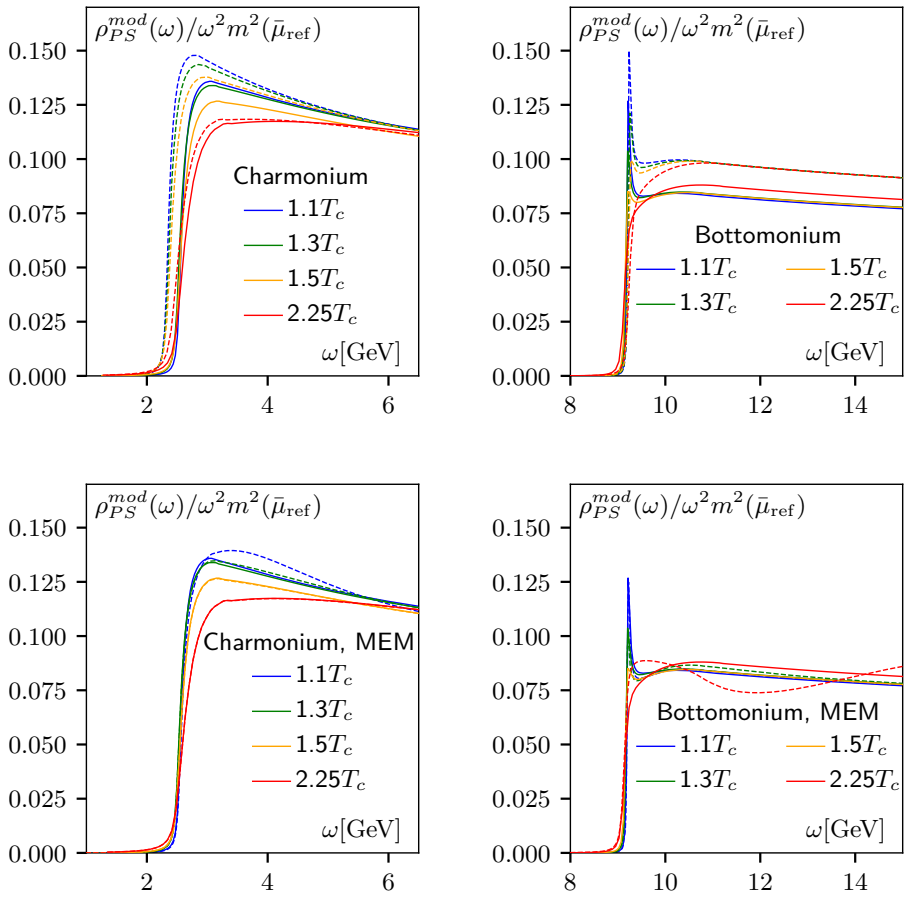

Figure 4.5: Spectral functions in the pseudoscalar channel for charmonium (*left*) and bottomonium (*right*). *Top:* The dashed lines show the original perturbative spectral functions (see section 2.3.3) and the solid lines show the modified versions after accounting for systematic uncertainties. The modifications made by the parameters A and B in our fits are only small. *Bottom:* Crosscheck with MEM. Here, the solid lines are our fit results used as default models and the dashed lines are the MEM output. We chose to not show the bottomonium result at $1.5T_c$, as the MEM analysis for this temperature failed due to uncertainties in the rescaled covariance matrix. But except for this one case, our model spectral functions remain mostly unchanged, meaning that they already describe the correlators well.

4.2 Quark Number Susceptibility

Before moving on to the analysis of the vector channel, we show the continuum extrapolated results for the quark number susceptibility χ_q. Since this quantity is used in the continuum extrapolation of the vector correlators, its determination is important for the rest of this chapter.

Via the conservation of the vector current, the quark number susceptibility is related to the zeroth component of the vector correlator:

$$G_{00} = \chi_q T \tag{4.3}$$

Since G_{00} and G_{ii} share the same renormalization constants, the quark number susceptibility is used to build a renormalization independent ratio before extrapolating to the continuum as explained in section 3.5. As χ_q becomes more reliable with increasing temperature, we normalized with χ_q'/T'^2 at a temperature of $T' = 2.25T_c$. But when analyzing the transport peak, we are often interested in the correlator divided by the quark number susceptibility at the corresponding temperature T, not at T'. Therefore we additionally continuum extrapolate the ratio χ_q/χ_q'. In this way, we again build a renormalization independent ratio. The results can be seen in tab. 4.3.

For the extrapolation of χ_q/χ_q' we start with the correlator G_{00} on the lattice, an example of which is shown in Fig. 4.6. Theoretically, G_{00} is constant at all τT, but in practice, the first few points are deviating from the constant due to cut-off effects. Thus, we use the midpoint to evaluate χ_q. The extrapolation method for χ_q follows the method for the correlators described in chapter 3 closely. We build the ratio of the quark number susceptibilities on every bootstrap sample for every value of κ. As for the correlators, we then perform a mass interpolation. For the full correlator we would then perform a spline interpolation in τT, but since we are only interested in the midpoint, this step is omitted here and we directly continuum extrapolate with an ansatz quadratic in the lattice spacing.

We then have the continuum results for $G_{ii}T'^2/\chi_q'T^3$ and for $\chi_q T'^2/\chi_q'T^2$ and can easily obtain $G_{ii}/\chi_q T$ by dividing. To further examinate the χ_q at different temperatures, we also extrapolate χ_q'/T'^2. The results are shown in Fig. 4.7. It is seen that the bottom quark number susceptibility is larger than the charm quark number susceptibility. Both increase with growing temperature.

Unresummed perturbation theory also provides an estimate for the quark number susceptibility using a similar approach as for the constant part of the transport contribution (see also [60]). At leading order, the quark number susceptibility is given as

$$T\chi_q^{LO} = G_{00}^{LO} = -4C_A \int_p T n_F'(E_p) \tag{4.4}$$

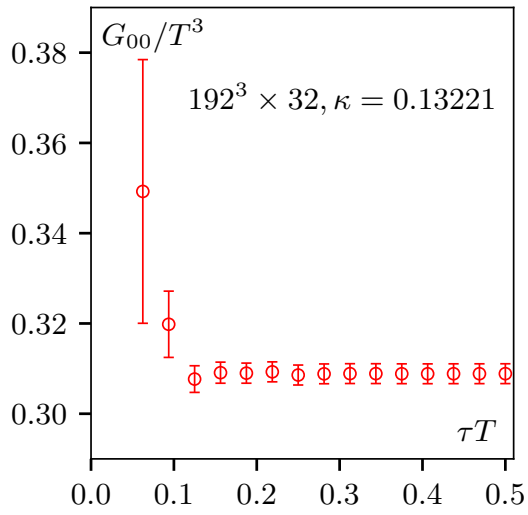

Figure 4.6: Example of the G_{00} correlator at the highest temperature on the finest lattice. After a few fluctuations at small τT due to cut-off effects, the correlator becomes constant. The midpoint is chosen for the further examination of the quark number susceptibility.

while the NLO version reads

$$T\chi_q^{NLO} = G_{00}^{NLO} = 4g^2 C_a C_F \int_p \frac{T n_F'(E_p)}{p^2} \int_k \left(\frac{n_B(\epsilon_k}{\epsilon_k} + \frac{n_F(E_k)}{E_k} \left(1 - \frac{M^2}{k^2} \right) \right). \tag{4.5}$$

If we compare our results with to the perturbative values in tab. 2.3, we observe a good agreement for the bottomonium correlator at all temperatures, while for charm the difference between lattice and perturbative result grows with decreasing temperature.

	Charmonium		Bottomonium	
T/T_c	χ_q/χ'_q	χ_q/T^2	χ_q/χ'_q	χ_q/T^2
1.1	0.063(2)		0.62(3)e-3	
1.3	0.145(5)		0.45(2)e-2	
1.5	0.333(9)		0.034(1)	
2.25	1	0.626(10)	1	0.0250(5)

Table 4.3: Quark number susceptibilities for charm and bottom at different temperatures.

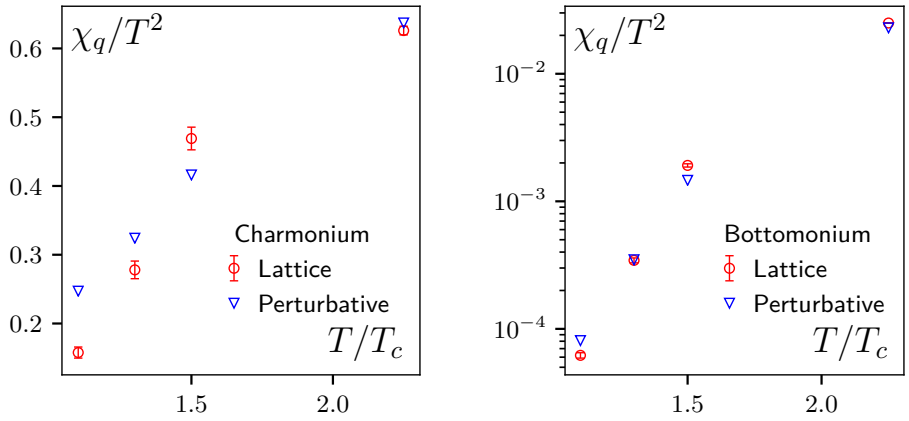

Figure 4.7: Continuum extrapolated quark number susceptibilities from charmonium and bottomonium correlators compared to estimates from unresummed perturbation theory. While for bottom the results roughly agree at all temperatures, the charm results only agree at the highest temperature and the differences grow with decreasing temperatures. Note that the right picture uses a logarithmic scale due to the large changes in the quark number susceptibility.

4.3 Vector Channel

Motivated by the success in the pseudoscalar channel, we extended our method to the vector channel. Due to the rise of the transport peak, the method is not as straightforward as this feature is not included in the perturbative description. Using a Lorentzian ansatz for the transport peak as motivated in section 2.4.2, we obtain

$$\rho_{ii}(\omega) = \underbrace{3D\chi_q \frac{\omega\eta^2}{\omega^2+\eta^2}}_{\rho_{ii}^{trans}(\omega)} + \underbrace{A\rho^{pert}(\omega - B)}_{\rho_{ii}^{mod}(\omega)} \tag{4.6}$$

with four fit parameters: A, B, D and η. Unfortunately a direct fit is not possible due to the high number of parameters. The next step would thus be to fix some of the parameters. As many calculations hint to values of $2\pi TD$ between 1 and 9 (see section 2.4.3), we decided to fix D to choices in that region and fit the remaining three parameters. The fit now converges but as seen in Figs. 4.8,4.9, the different choices all match the data equally well within errors. The reason can be seen in the upper and middle panel of Fig. 4.9. Every change in the transport peak is compensated by changes in the bound state region. Already small changes in A and B suffice to absorb large changes in the transport region. Thus we need to determine the two regimes seperately. There are different ways to split the analysis. We

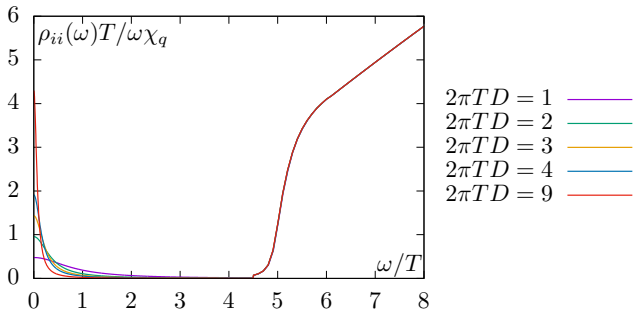

Figure 4.8: The spectral function obtained by fixing $2\pi TD$ to different values and fitting the remaining three parameters. The top panel shows the spectral function consisting of the Lorentzian transport peak at small ω and the perturbative model at larger ω. While the results for different choices of $2\pi TD$ vary much in the shape of the transport peak, the parameters A and B determining the higher and intermediate ω region are similar and only very small differences are observed there. Fig. 4.9 shows the corresponding correlators.

investigate two of them more closely.

The first makes use of the extremly flat curvature of the transport contribution to the correlator. By assuming this contribution to be constant, we can reduce the fit ansatz to three parameters:

$$G_{ii}^{const+mod}(\tau T) = G_{ii}^{trans,const} + \int_0^\infty \frac{\mathrm{d}\omega}{\pi} A\rho_{ii}^{pert}(\omega - B)K(\omega,\tau). \tag{4.7}$$

With $G_{ii}^{trans,const}$ we obtain a constant that could later be used as a constraint for investigations of the transport peak. The fit gives an A of approximately 1 and a small B, indicating that the perturbative spectral function is a good ansatz for intermediate and higher ω. The results match the data well, but a weakness to this ansatz is the lack of sensitivity to the curvature of the transport peak. By using a constant, we can obtain A and B for a further analysis of the bound state and vacuum asymptotic region but we might already be influencing later results for $2\pi TD$ and η too much.

An better way might be to use the differences of neighbouring correlators described in 2.2. As the transport contribution is more dominant around the midpoint, the subtraction of these points mostly cancels out the transport effects. We now construct a difference correlator from our model spectral function and fit to our lattice data for the difference correlator. As seen in Fig. 4.11 the fit matches the data well. As in the pseudoscalar channel, A is close to 1 and B is around 0, meaning that the perturbative model is a suitable ansatz. This is in agreement with the findings from the constant fits and indeed the differences are rather small. In Fig. 4.10, both ansätze are

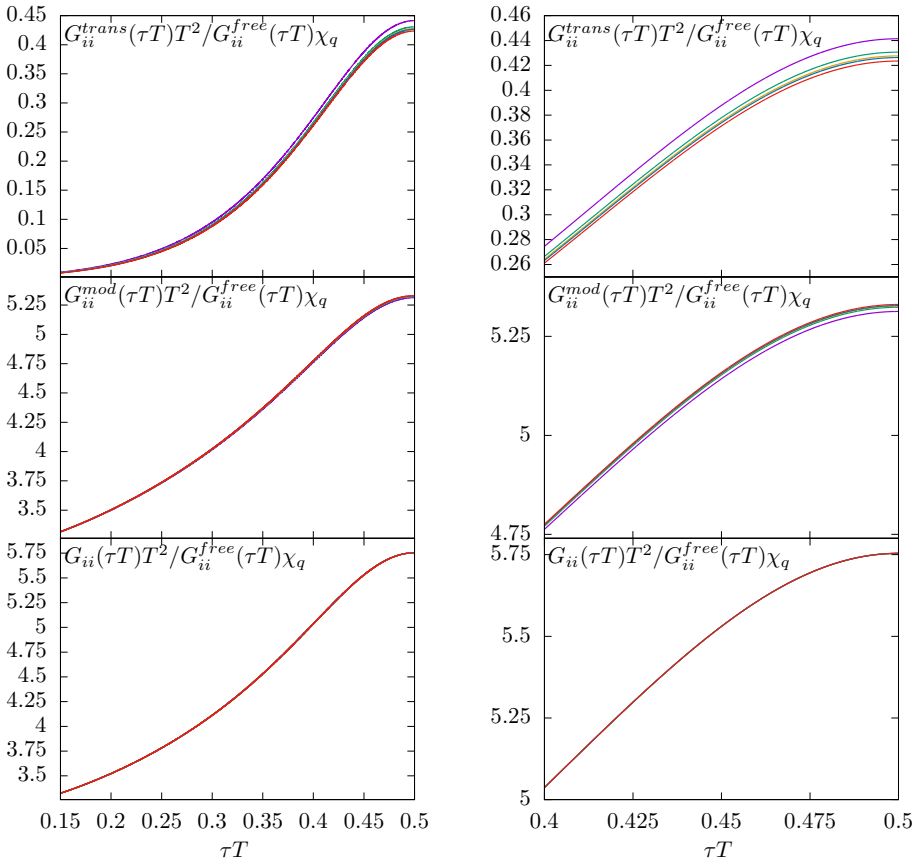

Figure 4.9: The correlators for the different parts of the spectral function, where the left side shows the whole τT range, while the right side zooms in on the correlator close to the midpoint as the transport contribution has the highest influence there. From the different correlators, a problem can be seen: Every change in the transport peak (upper correlator figures) is absorbed by the changes in the perturbative model correlator (middle correlator figures), so that the final results (bottom figures) do not show any difference, meaning they all match the data equally well. Thus, the three parameter fit method is not suitable to gain insights into the transport peak.

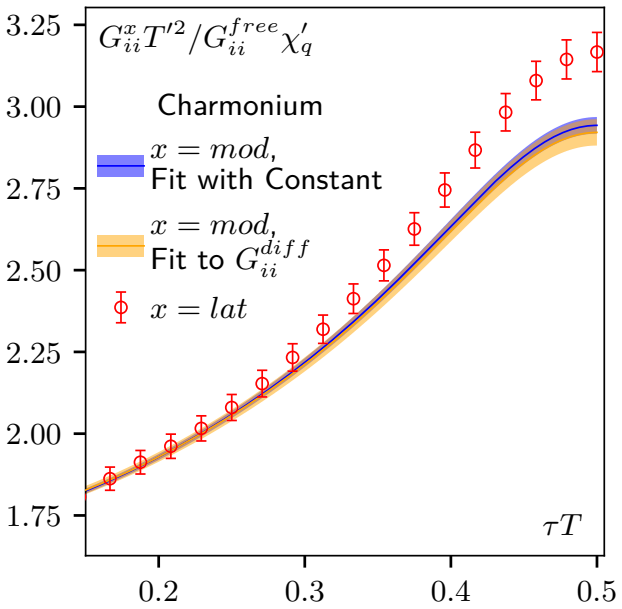

Figure 4.10: Comparison of two fit ansätze for the model spectral function for an example correlator (Charmonium, $1.5T_c$). The blue curve shows the result obtained by fitting the model correlator plus a constant transport contribution, while the orange curve shows the result obtained from fitting the difference correlator (see Fig. 4.11) and then inserting the results in the regular correlator (see Fig. 4.12). Both ansätze are relatively close with comparable error bands. In the further chapters of this thesis, we work with the result from the fits to the difference correlator.

compared. They lead to similar results and with comparable errors on the parameters A and B. Since the fit to the difference correlator does not make any assumptions about the transport peak beforehand and is thus valid for more cases, we from now on work with the results obtained from this method.

With the obtained values for A and B (tab. 4.4) we are able to describe the bound state and vacuum asymptotic region. Fig. 4.12 shows the comparison to the whole correlator. The differences between data and model correlator hint to the transport contribution and are further analyzed in chapter 5.

The spectral functions for the bound state and vacuum asymptotic region show a similar behaviour as in the pseudoscalar channel (see Fig. 4.13). For charmonium, the data is well described without a resonance peak, while bottomonium has one thermally broadened resonance peak that is melted at $2.25T_c$. The location of this peak lies around 9.2(2)GeV, which is close to $m_\Upsilon = 9.46$GeV. As for the pseudoscalar channel, the mass shift observed in [15] is not confirmed. Again, we crosscheck by using our result as a default

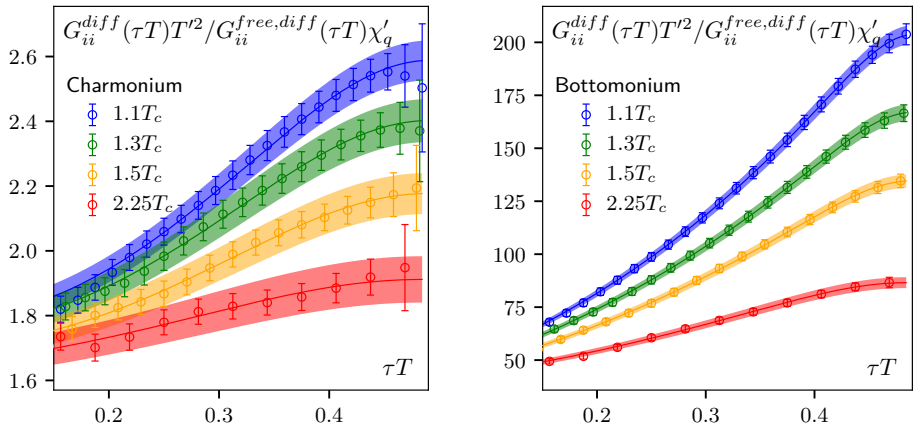

Figure 4.11: Fits to the difference of neighboring correlators for charmonium (*left*) and bottomonium (*right*) in the vector channel. As a normalization we used $\frac{\chi'_q}{T'^2}$ at a temperature $T' = 2.25T_c$. Overall, the curves describe the data well.

	Charmonium		Bottomonium	
T/T_c	A	B/T	A	B/T
1.1	1.09(2)	0.37(4)	1.03(2)	0.04(2)
1.3	1.07(2)	0.16(5)	1.01(1)	-0.05(2)
1.5	1.03(2)	0.01(6)	1.00(2)	-0.12(2)
2.25	0.99(3)	-0.27(9)	0.99(2)	-0.23(4)

Table 4.4: Modifications to the perturbative spectral function the high ω region obtained by fitting the correlator of the model spectral function eq.(4.1) to the lattice data G_{ii}^{diff} in the vector channel.

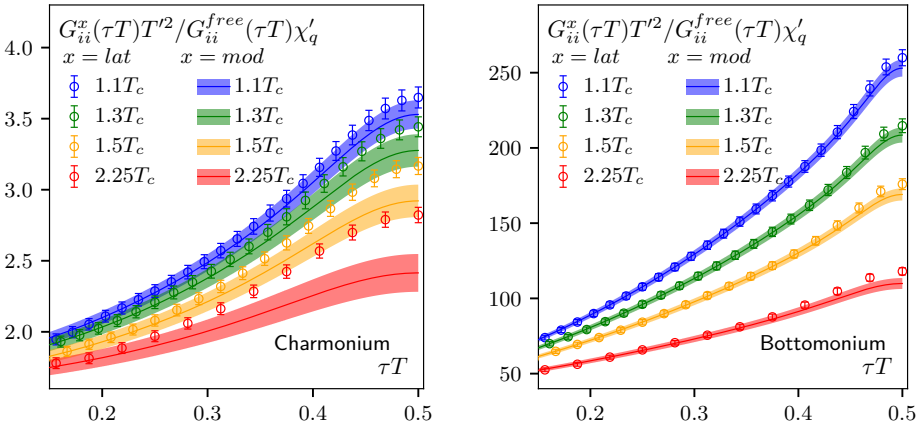

Figure 4.12: Comparison of our model spectral function (4.1) obtained from a fit to the difference correlator to the lattice data of the whole correlator. The differences hint to the transport contribution (chapter 5) and already contain some information: It seems as if the contribution for bottomonium is rather small, while the differences for charmonium grow with increasing temperature. Later, especially the differences at the midpoint will be of interest.

model for MEM. As MEM leaves the spectral functions almost unchanged, we conclude that our resulting spectral function for the intermediate and high ω region is well-suited to describe our data.

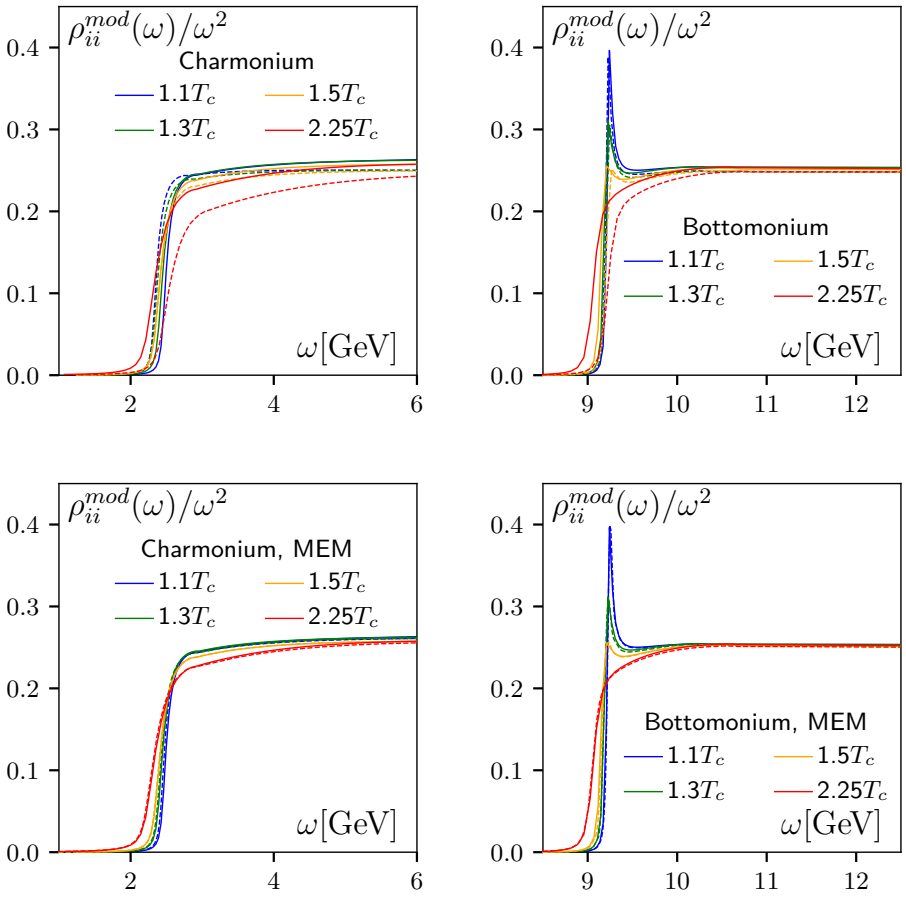

Figure 4.13: *Top:* Spectral functions in the high ω region for charmonium (left) and bottomonium (right) in the vector channel from the fits to $G_{ii}^{diff}(\tau)$. The dashed lines show the original perturbative spectral functions, while the solid lines show the modified spectral function. *Bottom:* Crosscheck using MEM. The dashed lines show the output of MEM when using the modified spectral function as a default model. Since MEM leaves the spectral functions almost unchanged, they are well-suited to describe the vector correlators.

Chapter 5

Transport Contribution

If we come back to the qualitative shape of the spectral function explained in section 2.3, we identified three major parts: The high frequency part describing the ultraviolet asymptotics, an intermediate region, where we expect bound states to fall in, and a transport peak around $\omega \approx 0$. The former two are well described by the model spectral function (4.1) analyzed in the previous chapter. In the pseudoscalar channel, where there is no transport contribution, we thus already have a complete description of the spectral function that matches our correlator data very well. This chapter will now provide insights into the low frequency spectral function of the vector channel and thus complete the analysis of our correlators.

In the previous chapter, we splitted the analysis of the vector channel into two parts, as it was not possible to fit the transport peak and the higher frequency part simultaneously. By a fit to the difference correlator we determined a model spectral function ρ_{ii}^{mod} for intermediate and higher frequencies (see (4.1) and tab. 4.4). In Fig. 4.12 the corresponding correlator G_{ii}^{mod} is compared to the continuum extrapolated lattice data G_{ii} obtained with the setup in chapter 3. As G_{ii}^{mod} does not describe the whole spectral function, there is a difference between the continuum data and the model, which is clearly seen in the figure. This gap will now be closed by the transport contribution:

$$G_{ii}^{trans}(\tau T) = G_{ii}(\tau T) - G_{ii}^{mod}(\tau T). \tag{5.1}$$

The mentioned figures already allow for some qualitative conclusions. It can be seen that for charmonium the transport contribution grows with increasing temperature and is generally larger than for bottomonium.

In order to reach a deeper understanding of the transport contribution and to extract the heavy quark diffusion coefficient D, we need to employ an ansatz for the low frequency spectral function. As mentioned in section 2.4.1, linear response theory relates the transport peak to the heavy quark

diffusion coefficient D via a Kubo formula

$$D = \frac{1}{3\chi_q} \lim_{\omega \to 0} \frac{\rho_{ii}(\omega)}{\omega}, \tag{5.2}$$

The shape of the transport peak can be modelled using Brownian motion and the Langevin formalism. According to [14] this leads to a Lorentzian ansatz as presented in section 2.4.2. To prevent an overestimation of the transport peak at larger frequencies, we use an additional cut-off $1/\cos(\omega/2\pi T)$ proposed in [40]:

$$\rho_{ii}^{trans}(\omega) = 3D\chi_q \frac{\omega\eta^2}{\omega^2 + \eta^2} \frac{1}{\cosh\left(\frac{\omega}{2\pi T}\right)}, \tag{5.3}$$

where the drag coefficient η corresponds to the width of the peak and is connected to D via the Einstein relation [82]

$$\eta = \frac{T}{MD}. \tag{5.4}$$

It is not entirely clear, which kinetic mass M to insert. In this work we used $M_c = 1.28\text{GeV}$ and $M_b = 4.18\text{GeV}$, but assume a 10% uncertainty. We then use the Einstein relation to eliminate one of the two parameters D and η to simplify our calculations. This leads to

$$\rho_{ii}^{trans}(\omega) = 3\chi_q \frac{T}{M} \frac{\omega\eta}{\omega^2 + \eta^2} \frac{1}{\cosh\left(\frac{\omega}{2\pi T}\right)}, \tag{5.5}$$

Another ansatz sometimes applied to the transport region is the Gaussian ansatz [14]. In this work, we apply the Lorentzian ansatz but use the Gaussian ansatz as a crosscheck. The results can be found in the appendix.

At infinitely high temperature, the width approaches zero and for both ansätze the transport peak takes the form of a δ peak as predicted in [14, 83, 84]

$$\rho_{ii}^{trans}(\omega) \underset{\eta \to 0}{\longrightarrow} 2\pi\chi_q \frac{T}{M} \omega\delta(\omega). \tag{5.6}$$

In Fig. 5.1 the transport contribution G_{ii}^{trans} is shown. The data points are obtained by subtracting the model for higher frequency contributions from the continuum data, according to (5.1). As many calculations presented in section 2.4.3 hint to values of 1-9 for the heavy quark diffusion coefficient, we additionally show the transport contributions obtained with the Lorentzian ansatz and different choices of $2\pi TD$ in this region. It can already be seen why the analysis of the transport peak is a challenging task: The curvature of our data is extremely small, especially when compared to the statistical

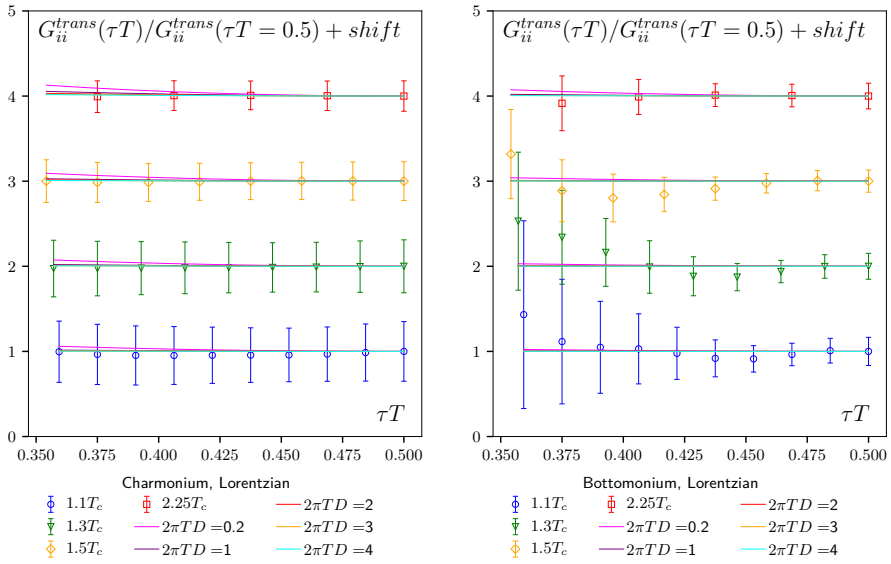

Figure 5.1: The transport contribution normalized by its midpoint. The shift in y direction does not have a physical meaning but is rather to guide the eye. It can be seen that the curvature is extremely small compared to the uncertainties on the data. For a comparison we plotted the same contribution for a Lorentzian ansatz (5.3) with different choices of $2\pi TD$, where the drag coefficient is determined via the Einstein relation (5.4) with masses of $M_c = 1.28\text{GeV}$ and $M_b = 4.18\text{GeV}$. Within errors all choices match our data and the value of $2\pi TD$ can not be resolved based on curvature.

uncertainties. Thus, the different choices of $2\pi TD$ can not simply be resolved based on the curvature or a fit and we have to try other approaches.

For a more detailed analysis we are especially interested in the difference at the correlator midpoint $G_{ii}^{trans}(\tau T = 0.5)$, where the influence of the transport contribution is the strongest. Fig. 5.2 shows this midpoint for charmonium and bottomonium and in comparison to the respective whole correlators. For both quarkonia, the transport contribution only accounts for a small fraction of the correlator while the major contribution comes from the intermediate and high frequency part discussed in the previous chapter. It can further be seen that the transport contribution rises with temperature for charmonium, while for bottomonium it remains largely constant within errors. The further investigation of the midpoint is divided into several parts. Before we calculate transport coefficients quantitatively, we approach qualitatively by first comparing to perturbative results and drawing some conclusions from the comparison of charmonium and bottomonium.

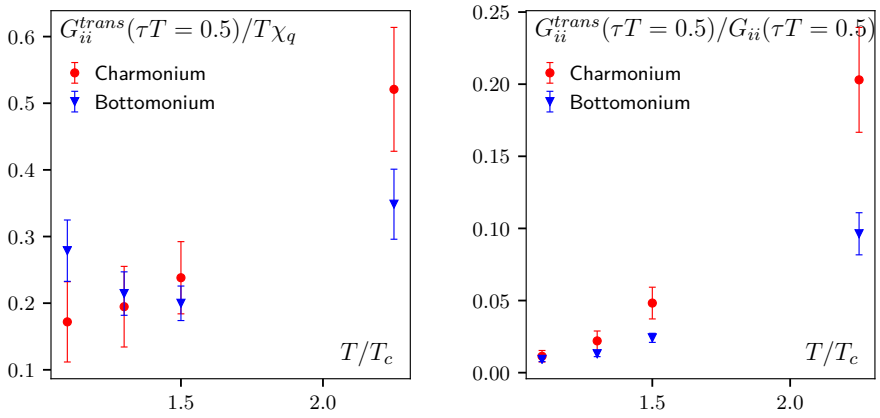

Figure 5.2: The midpoint of $G_{ii}^{trans}/(T\chi_q)$ for charmonium and bottomonium at different temperatures. While the charmonium transport contributions rise with temperature, the bottomonium transport contributions remain roughly constant. The right plot shows the fraction of the midpoint value that stems from the transport contribution.

5.1 Comparison to Perturbative Constants

Even though perturbation theory can not provide an exact shape of the transport peak, it can give an estimate for the constant part of its contribution to the correlator in a similar way as the quark number susceptibility is calculated. The results up to NLO from [60] are given in tab. 2.3. In our analysis, we specifically chose not to assume the contribution to be constant from the beginning, but as our results for G_{ii}^{trans} show only very little curvature, it is still reasonable to compare our result at the midpoint to the perturbative constant. In Fig. 5.3 we see that the perturbative and lattice results for bottomonium agree within errors for most temperatures. For charmonium, not even the highest temperature agrees and the deviations grow with decreasing temperature. This confirms the expectation that perturbation theory describes bottomonium better than charmonium.

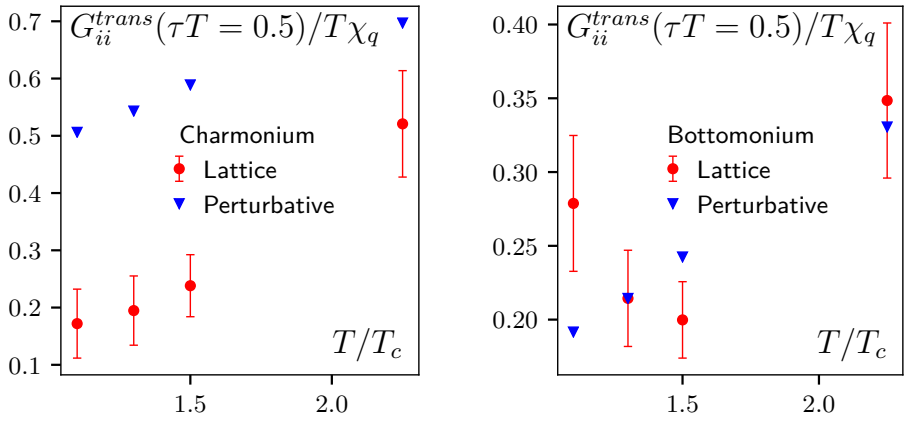

Figure 5.3: Comparison of the transport contribution at the midpoint determined in (5.1) and the perturbative constants from [60]. For bottomonium (*right*) we see agreement to some extent, at least for 1.3 and $2.25T_c$ and for $1.5T_c$ if we consider that the perturbative constants might also suffer some uncertainties. For charmonium (*left*) on the other hand, the perturbative results overshoot our data at all temperatures. The deviation becomes smaller with increasing temperature.

5.2 Comparison of Charmonium and Bottomonium

To get some more insights on the transport coefficients, we now assume a Lorentzian shape (5.3)[1]. We now insert (5.5) into (2.16) and cut the integration of at some frequency ω_{cut} to avoid an overestimation at large frequencies, where the transport peak should not have an effect. At the midpoint, where the integration kernel simplifies to $1/\sinh(\frac{\omega}{2T})$, the correlator then reads

$$\begin{aligned} G_{ii}^{trans}(\tau T = 0.5) &= \int_0^{\omega_{cut}} \frac{\mathrm{d}\omega}{\pi} 3D\chi_q \frac{\omega\eta^2}{\omega^2+\eta^2} \frac{1}{\cosh\left(\frac{\omega}{2\pi T}\right)} \frac{1}{\sinh\left(\frac{\omega}{2T}\right)} \\ &= \int_0^{\omega_{cut}} \frac{\mathrm{d}\omega}{\pi} 3\chi_q \frac{M}{T} \frac{\omega\eta}{\omega^2+\eta^2} \frac{1}{\cosh\left(\frac{\omega}{2\pi T}\right)} \frac{1}{\sinh\left(\frac{\omega}{2T}\right)} \end{aligned} \tag{5.7}$$

[1]The following analysis would work for other ansätze as well. As a crosscheck we tried the Gaussian ansatz (B.1). This leads to similar results, see appendix.

We perform a Taylor expansion of the kernel and the cut-off term around $\omega \approx 0$:

$$\frac{\cosh\left(\omega(1/2T - 1/2T)\right)}{\sinh\left(\frac{\omega}{2T}\right)\cosh\left(\frac{\omega}{2\pi T}\right)} \approx \frac{2T}{\omega} - \frac{(3+\pi^2)\omega}{12\pi^2 T} + \frac{(75+30+7\pi^4)\omega^3}{2880\pi^4 T^3} - \frac{(1281+525\pi^2+147\pi^4+31\pi^6)\omega^5}{483840\pi^6 T^5} + \mathcal{O}\left(\omega^7\right). \tag{5.8}$$

This expansion is then used together with the Lorentzian ansatz in the integration (2.16), which leads to an approximated correlator

$$\frac{G_{ii}^{trans}(\tau T = 0.5)}{\chi_q T} = \frac{T}{\pi M}\left(f_1 + f_2 + f_3 + f_4 + \mathcal{O}(\omega^7)\right), \tag{5.9}$$

with the following factors f_i:

$$f_1 = 2\arctan\left(\frac{\omega_{cut}}{\eta}\right) \tag{5.10}$$

$$f_2 = \frac{(3+\pi^2)\eta^2}{12\pi^2 T}\left(\arctan\left(\frac{\omega_{cut}}{\eta}\right) - \frac{\omega_{cut}}{\eta}\right) \tag{5.11}$$

$$f_3 = \frac{7\left(15+\pi^4\right)\eta}{8640\pi^4 T^3}\left(3\eta^3\arctan\left(\frac{\omega_{cut}}{\eta}\right) - 2\eta^2\omega_{cut} + \omega_{cut}^3\right) \tag{5.12}$$

$$f_4 = \frac{(1281+525\pi^2+147\pi^4+31\pi^6)\eta}{483840\pi^6 T^5} \cdot \left(-\arctan\left(\frac{\omega_{cut}}{\eta}\right)\eta^5 + \eta^4\omega_{cut} - \frac{\eta^2\omega_{cut}^3}{3} + \frac{\omega_{cut}^5}{5}\right). \tag{5.13}$$

These coefficients only depend on the drag coefficient η and the frequency ω_{cut} at which we cut off the integration. The higher order terms f_3 and f_4 are negligible in comparison to f_1, f_2 is around 5% of f_1. As we aim for a qualitative estimate, we also neglect f_2. We apply these simplifications and build the ratio of charmonium and bottomonium correlators at the midpoint:

$$\frac{G_{ii,c}^{trans}/\chi_q^c}{G_{ii,b}^{trans}/\chi_q^b} \approx \frac{M_b}{M_c}\frac{\tan^{-1}\left(\frac{\omega_{cut}}{\eta^c}\right)}{\tan^{-1}\left(\frac{\omega_{cut}}{\eta^b}\right)}. \tag{5.14}$$

The appearing ratio of masses $\frac{M_b}{M_c}$ is around 3. If we now compare with Fig. 5.2, where it is seen that the midpoint of the transport contribution for charmonium is almost always larger or at least around that of bottomonium, we can conclude that $\eta^c > \eta^b$.

5.3 Estimating the Transport Coefficients

To gain a more quantitative estimate for the transport coefficients, we again use the Lorentzian ansatz[2] and consider the midpoint, see (5.7). In Figs. 5.8 and 5.4, we now compare the midpoint obtained from different values of the drag coefficient η (curves) to our data points (constant lines). As masses, we again choose $M_c = 1.28\text{GeV}$ and $M_b = 4.18\text{GeV}$, but as we aim for a quantitative estimate, we now also take an uncertainty of 10% into account. On the data side, we show the statistical uncertainties as errorbands on the constant lines. Within theses errors we see an overlap for our data and the ansatz. We determine the lower and upper bound of this overlapping region and thus are able to give a range for η.

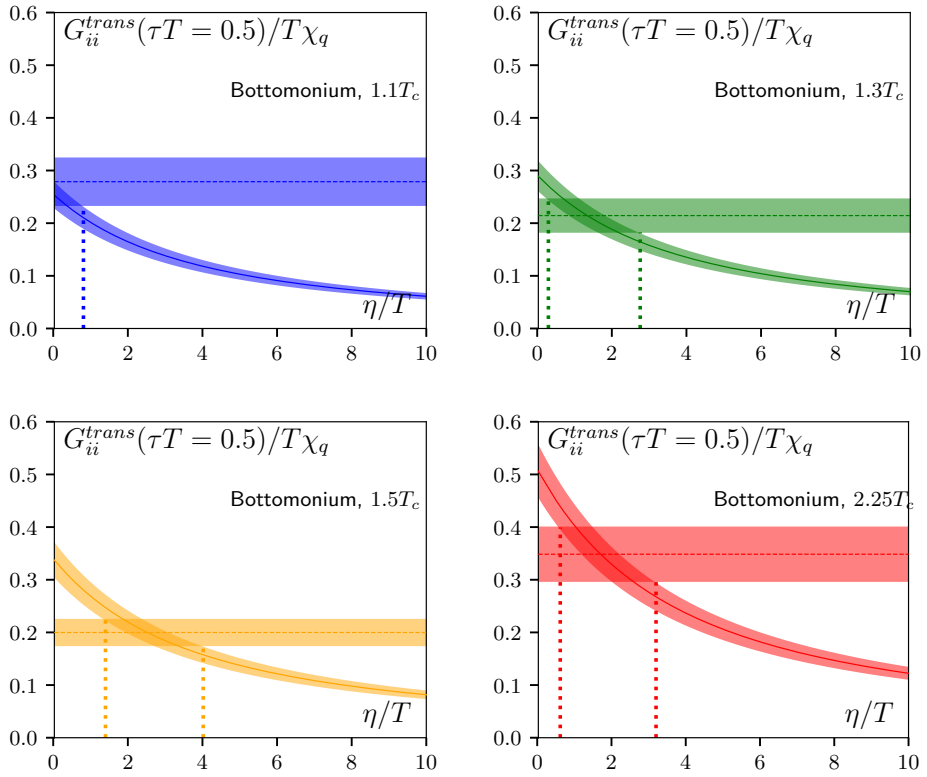

Figure 5.4: Determination of a range for η at different temperatures using the bottomonium results. The dashed constant lines represent our data for the midpoint of G_{ii}^{trans} with errors. The solid curves show the results of a Lorentzian ansatz from 5.7, where the errorbands are obtained by assuming an uncertainty of $\sim 10\%$ in the mass. The intersection points (*dotted*) are then taken as upper and lower bound of a range for possible η/T and are given in tab. 5.1.

[2] And again check with the Gaussian ansatz, see appendix.

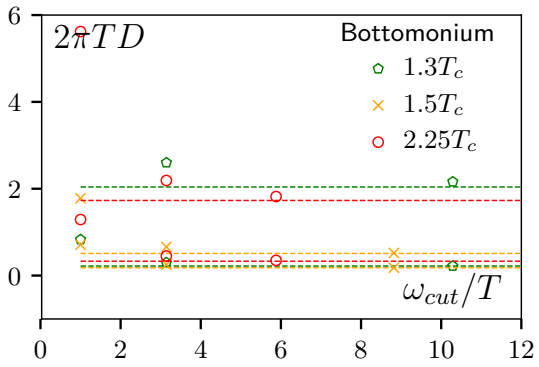

Figure 5.5: The different upper and lower boundaries for $2\pi TD$ depending on the upper limit of the integration. The dashed lines show the result at $\omega_{cut} = \infty$, that are later taken as the final result. It can be seen that the higher ω_{cut} is, the more the results approach the result at an infinite cut-off. After the first point, there seems to be a plateau.

The given figures show the result for an upper integration limit of $\omega_{cut} = \infty$, but we also investigated the limits $\omega_{cut} = T, \pi T, M$ to gain an understanding of how far the relevant contribution of the transport peak stretches out in ω. For bottomonium, a plateau is reached after πT. From there on, the different choices of integration limits produce roughly the same overlap regions. Fig. 5.5 shows the dependence of the lower (η^{small}) and upper (η^{large}) bound of the drag coefficient on the upper limit of the integration. It can be seen that both are close to their value at $\omega_{cut} = \infty$ for $\omega_{cut} > \pi T$. We thus choose an upper limit of infinity as the integration limit as this is the choice with the strongest physical motivation. The results for the range of η and the corresponding values of $2\pi TD$ are given in tab. 5.1.

If we now combine the model spectral function for intermediate and higher frequencies with our findings for the transport peak, we can now give a spectral function for the whole ω range (see Fig. 5.6). For bottomonium, both parts are clearly separated. The transport peak falls off rapidly and gives almost no contribution at frequencies where bound states arise.

We also calculate the whole correlator by adding the model correlator G_{ii}^{mod} for intermediate and high frequencies and the transport contribution using the η range from our method. The results can be seen in Fig. 5.7 with the dashed lines showing the low η result and the solid line the high η result. It is seen that with the combination of the two parts, the whole correlator is described. We have thus obtained one possible spectral function of bottomonium in the vector channel.

Regarding the heavy quark diffusion coefficient, the method in this sections leads to results between $2\pi TD = 0.18$ and $2\pi TD = 2.04$ with no

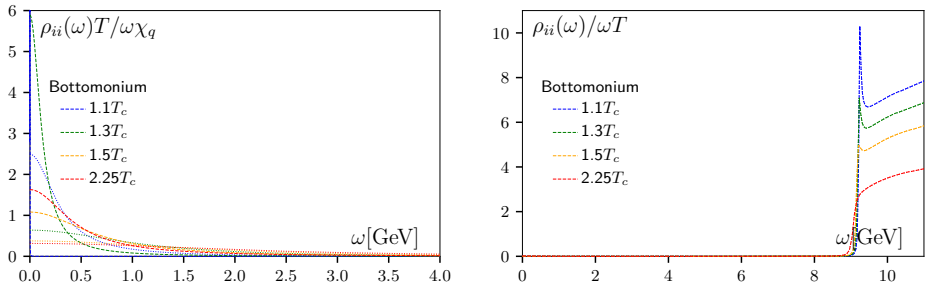

Figure 5.6: The spectral function for bottomonium consisting of the model ansatz for intermediate and higher ω and the transport peak using our results in tab. 5.1. The dashed lines show the spectral function for the lower bound of η, while the dotted lines show it for the upper bound. The right side shows an overview of the whole spectral function, while the left side zooms into the transport region.

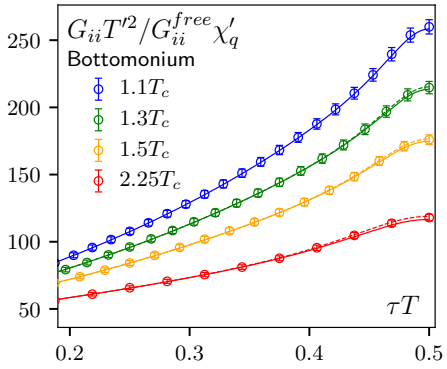

Figure 5.7: The whole bottomonium correlator consisting of the model correlator for intermediate and high ω and the transport contribution based on the Lorentzian ansatz with the η from tab. 5.1. The dashed line stands for the lowest choice of η and the solid for the highest choice. For comparison, we also show the data points from our continuum extrapolated lattices.

obvious temperature dependence. In section 5.5, this range will be combined with estimates from another method to gain a final result.

We repeat the same method for charmonium with the intersection ranges shown in Fig. 5.8. Here, however, the analysis is more complicated as transport peak and bound state region are not as clearly separated. The investigation of the different integration limits $\omega_{cut} = T, \pi T, M, \infty$ shows no plateau, meaning that the transport peak stretches far out.

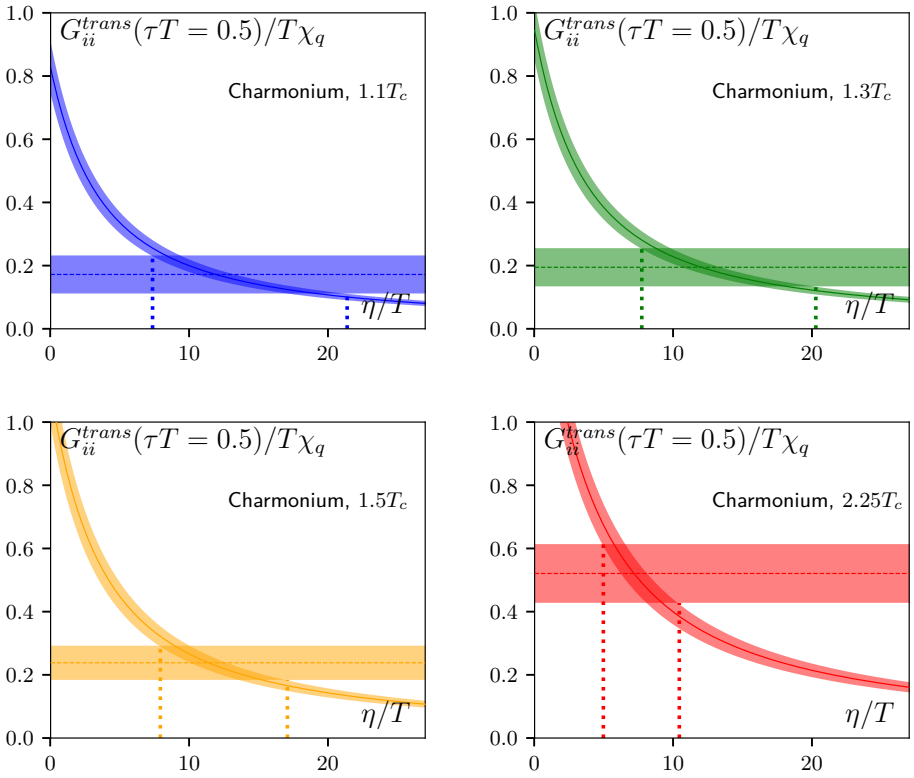

Figure 5.8: Determination of a range for η at different temperatures using the charmonium results. The dashed constant lines represent our data for the midpoint of G_{ii}^{trans} with errors. The solid curves show the results of a Lorentzian ansatz from 5.7, where the errorbands are obtained by assuming an uncertainty of $\sim 10\%$ in the mass. The intersection points (*dotted*) are then taken as upper and lower bound of a range for possible η/T and are given in tab. 5.1.

If we combine the model spectral function for intermediate and higher frequencies with our findings for the transport peak, we are able to describe the whole correlator. In Fig. 5.9, we see the comparison to the continuum data. Again the results are shown with dashed lines for the lower bound of η and solid lines for the higher bound of η. The corresponding spectral functions for the whole ω range are given in Fig. 5.10. Here, we clearly see

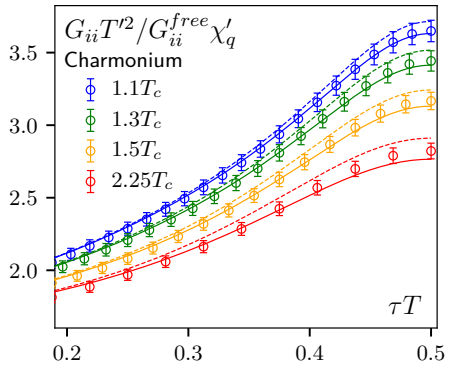

Figure 5.9: The whole charmonium correlator consisting of the model correlator for intermediate and high ω and the transport contribution based on the Lorentzian ansatz with the η from tab. 5.1. The dashed line stands for the lowest choice of η and the solid for the highest choice. For comparison, we also show the data points from our continuum extrapolated lattices.

that the transport region stretches out into the bound state region, which causes problems in our method. This ansatz is suited much better for bottomonium. Still, we quote the η range for $\omega_{cut} = \infty$ in tab. 5.1 as we did for bottomonium, with the remark that we should not rely on these numbers too much but rather use the bottomonium results and the findings from the previous and the following section.

	Charmonium		Bottomonium	
T/T_c	η/T	$2\pi TD$	η/T	$2\pi TD$
1.1	7.37-21.38	0.08-0.24	<0.81	>0.66
1.3	7.75-20.28	0.10-0.26	0.30-2.76	0.22-2.04
1.5	7.93-17.08	0.14-0.29	1.40-4.02	0.18-0.51
2.25	4.98-10.45	0.33-0.70	0.62-3.20	0.33-1.73

Table 5.1: Estimated ranges for η/T from Figs. 5.8,5.4 and their corresponding values for $2\pi TD$ according to the Einstein relation with a mass of $M_c = 1.28$GeV and $M_b = 4.18$GeV.

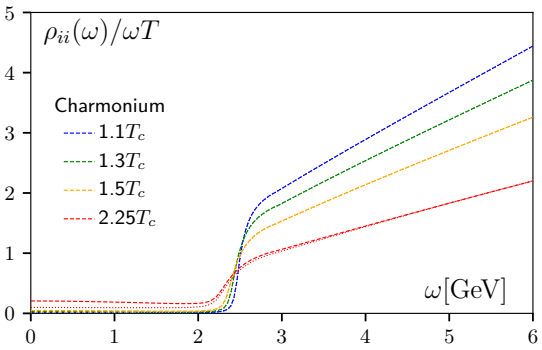

Figure 5.10: The spectral function for charmonium consisting of the model ansatz for intermediate and higher ω and the transport peak using our results in tab. 5.1. The dashed lines show the spectral function for the lower bound of η, while the dotted lines show it for the upper bound.

5.4 Thermal Moments

To gain further information on the transport peak, we Taylor expand the correlator around the midpoint to obtain the thermal moments mentioned in section 2.2.2. As explained there, we get the ratios of thermal moments by fitting the curvature of our continuum extrapolated correlators with the Taylor expansion

$$\frac{\Delta_H(\tau T)}{G_H(\tau T = 0.5)} \approx R_H^{2,0} \left(1 + \sum_{n=1}^{N} R_H^{2n+2,2n} (\tau T - 0.5)^{2n}\right). \tag{5.15}$$

For charmonium we choose $N = 1$, for bottomonium $N = 2$. The fit is conducted on every bootstrap sample and the fit parameters $R^{2n+2,2n}$ are averaged later. Examples of the fit are shown in Figs. 5.11 and 5.12. As explained before, the approximation is valid around the midpoint, so the fit interval should be closely around $\tau T = 0.5$, but at the same time we need enough data points to conduct a fit with realistic errors, where the number of points depends on the number of parameters that we choose in the approximation. We chose to show the thermal moments up to the order of $R^{4,2}$ for charmonium since the corresponding fits have two parameters and are stable. For bottomonium the fits still lead to good results with one more parameter $R^{6,4}$. Adding another thermal ratio works for some temperatures but leads to instabilities at others.

The resulting thermal ratios depending on the lower limit of the fit intervall, $\tau_{min}T$, can be seen in Figs. 5.13 and 5.14. To quote a number for the thermal ratios, we identify plateaus in the fit results and average over the values inside the plateau and arrive at the results in tab. 5.2. If no plateau is

found, we use the closest values to the midpoint that have reasonably small errors. The values over which the average is taken are indicated by the length of the lines in Figs. 5.13 and 5.14.

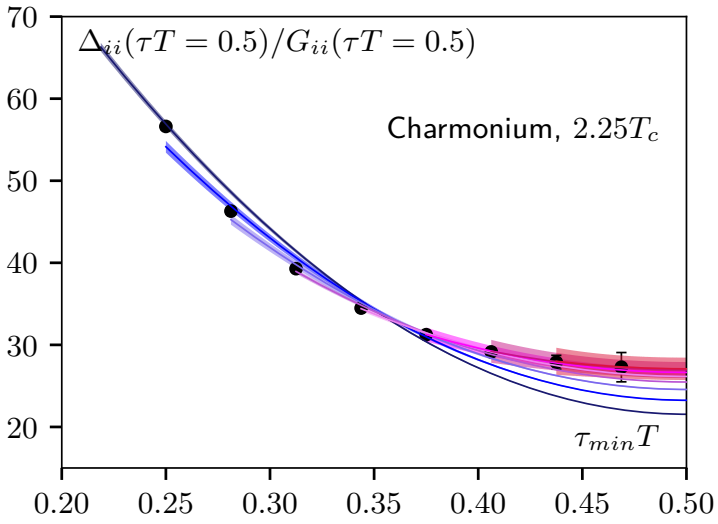

Figure 5.11: Curvature of the charmonium correlator at $2.25T_c$. The lines show the fit (2.30) for different ranges. As fit parameters we used the first two thermal ratios, $R^{2,0}$ and $R^{4,2}$. For intervalls with starting points close to the midpoint (pink curves), this describes the data well, while for larger intervalls (blue curves), higher orders need to be taken into account.

	Charmonium		Bottomonium		
T/T_c	$R^{2,0}$	$R^{4,2}$	$R^{2,0}$	$R^{4,2}$	$R^{6,4}$
1.1	52.28(24)	16.60(64)	389.4(1.5)	64.4(1.2)	24.2(1.6)
1.3	44.22(10)	14.49(47)	303.04(35)	52.19(65)	16.3(1.3)
1.5	37.59(21)	14.28(74)	229.45(22)	39.33(26)	14.03(74)
2.25	26.89(16)	13.02(1.35)	114.37(37)	22.10(13)	9.34(84)

Table 5.2: Thermal ratios at different temperatures, determined by averaging over the plateaus identified in Figs. 5.13,5.14. For charmonium, we use the first two ratios as a fit with three parameters lead to instabilities. For bottomonium, adding a third ratio was possible.

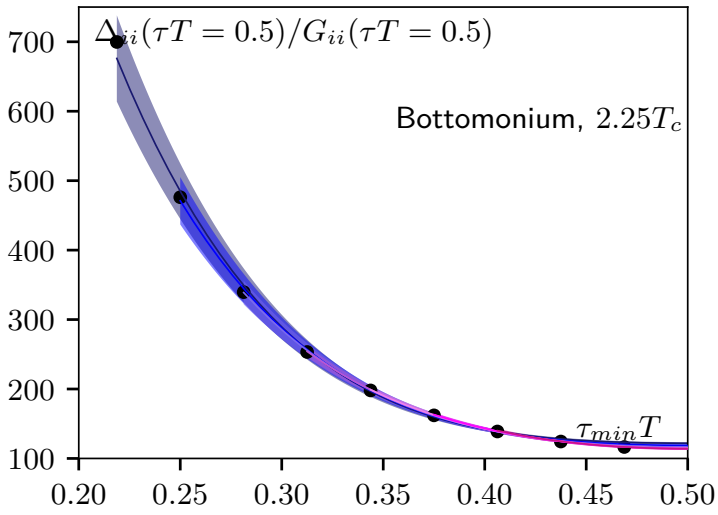

Figure 5.12: Curvature of the bottomonium correlator at $2.25T_c$. The lines show the fit (2.30) for different ranges. As fit parameters we used the first three thermal ratios, $R^{2,0}, R^{4,2}$ and $R^{6,4}$. Due to taking a higher order into account, the fits describe the data better than for charmonium, even at smaller starting points $\tau_{min}T$.

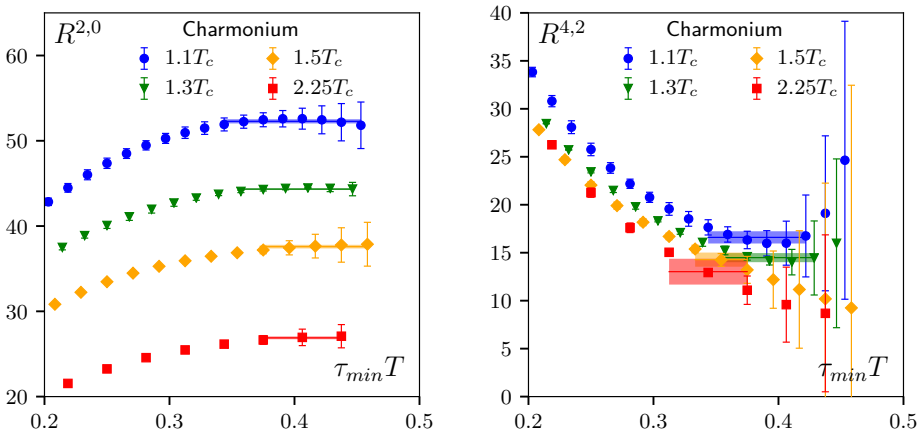

Figure 5.13: The thermal ratios depending on the lower limit of the fit intervall for Charmonium. The line shows the average and error over a plateau region indicated by the length of the line. For some cases, no plateau was found. In that case we averaged over values with reasonably small errors.

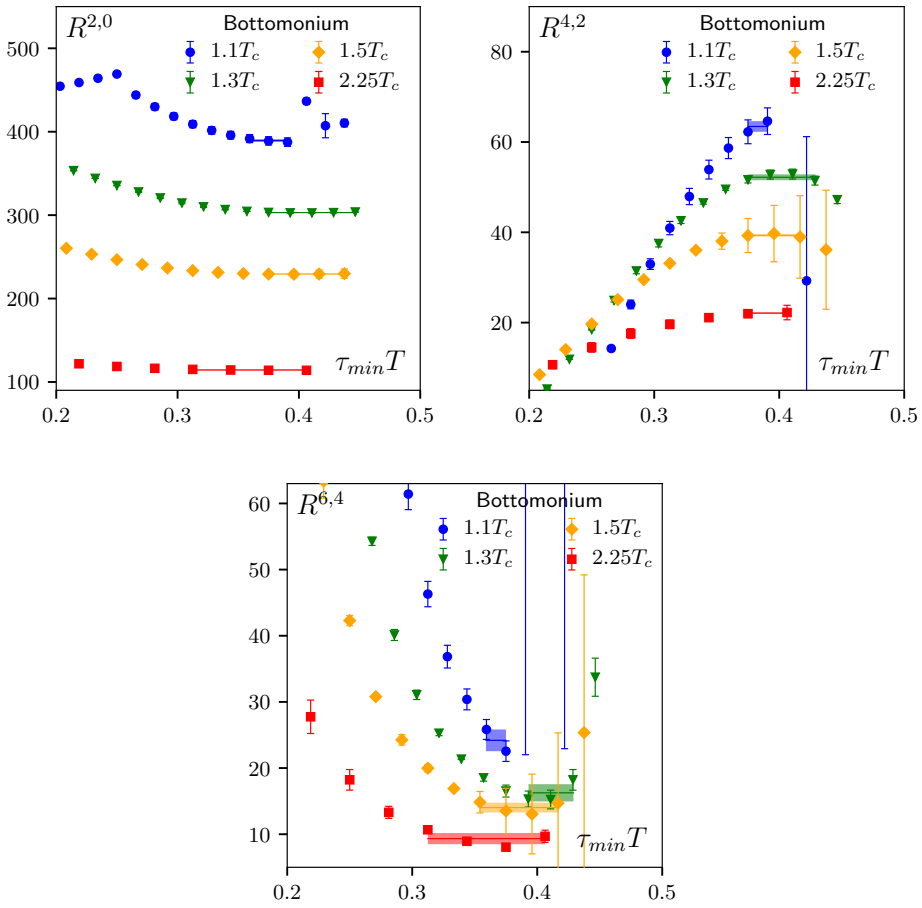

Figure 5.14: Like Fig. 5.13 but for bottomonium and also including the next order $R^{6,4}$.

We can now compare the thermal ratios from our data to the ones calculated using our spectral function (4.6). For $R^{2,0}$, this reads

$$R^{2,0}(A,B,\eta) = \frac{G^{(2)}_{mod}(A,B) + G^{(2)}_{trans}(\eta)}{G^{mod}_{ii}(\tau T = 0.5) + G^{trans}_{ii}(\tau T = 0.5)} \tag{5.16}$$

with

$$G^{(2)}_{mod}(A,B) = \frac{1}{2}\int_0^\infty \frac{\mathrm{d}\omega}{\pi}\left(\frac{\omega}{T}\right)^2 A\rho^{pert}_{ii}(\omega - B)\frac{1}{\sinh\left(\frac{\omega}{2T}\right)} \tag{5.17}$$

$$G^{(2)}_{trans} = \frac{1}{2}\int_0^\infty \frac{\mathrm{d}\omega}{T}\left(\frac{\omega}{T}\right)^2 3\chi_q \frac{T}{M}\frac{\omega\eta}{\omega^2+\eta^2}\frac{1}{\cosh\left(\frac{\omega}{2\pi T}\right)\sinh\left(\frac{\omega}{2T}\right)}, \tag{5.18}$$

where we use A and B from tab. 4.4 and the estimated ranges for η from the previous section. Fig. 5.15 shows that the lower choice for η is always closer to the data than the higher choice for $R^{2,0}$. Especially at higher temperatures, there is already some agreement, but in general the moments calculated from our model tend to overshoot the data. For $R^{4,2}$, the results for the two different η are so close that a distinction is not possible, especially not given the errors on the data. Thus we only investigate the $R^{2,0}$ further.

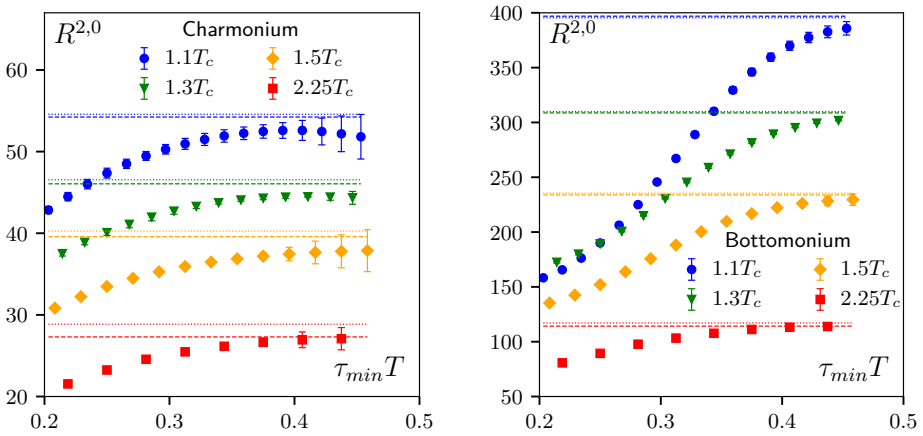

Figure 5.15: Thermal moments depending on the starting point of the fit intervall compared to the result of (5.16) using A and B from tab. 4.4 and the η-range from the previous section. The dashed lines show the result for the lower bound of η and the dotted lines show the result for the upper bound.

Similar to the method we applied for the midpoint, we now solve (5.16) for η. To get a range of possible results, we take the statistical errors of A,B and the $R^{2,0}$ coming from the data into account, as well as an uncertainty of

$\sim 10\%$ in the mass. We determine a lower and an upper bound for η, given in tab. 5.3 and use the Einstein relation to obtain $2\pi TD$. Unfortunately, this does not work for all temperatures. For charmonium, we get results for 1.3,1.5 and $2.25T_c$, while for bottomonium there are only intersections at $2.25T_c$. The ranges we obtain with this method differ from the result in the previous section. In general, this method seems to work better for charmonium.

	Charmonium		Bottomonium	
T/T_c	η/T	$2\pi TD$	η/T	$2\pi TD$
1.1	-	-	-	-
1.3	<0.27	>7.48	-	-
1.5	0.85-2.78	0.84-2.73	-	-
2.25	3.32-5.28	0.66-1.05	0.29-1.10	0.97-3.66

Table 5.3: Estimated ranges for η/T using the thermal ratio $R^{2,0}$. Their corresponding values for $2\pi TD$ are obtained by the Einstein relation with a mass of $M_c = 1.28$GeV. For some temperatures, the method did not give a result.

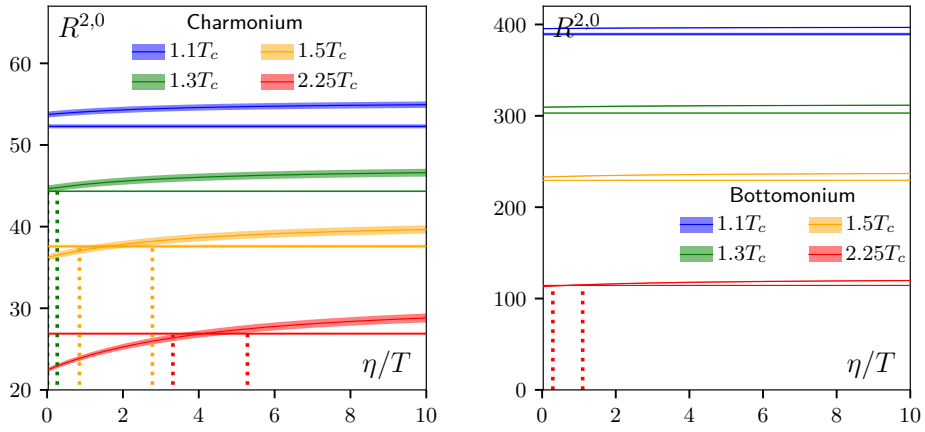

Figure 5.16: Comparison of the first thermal ratio from the data to the result of (5.16). The constant lines represent the average over a plateau and the error bands are the standard error of this average. The error bands for the curves are obtained by assuming a 10% uncertainty in the mass. The dotted lines indicate the ranges, where ansatz and data overlap.

5.5 Combining the Results

In this chapter, several attempts have been made at estimating $2\pi TD$ and η, each more suitable for some cases and less for others. As a reminder, the

different methods used are:

- Qualitative analysis of the ratio of η^c and η^b (see section 5.2).
- Comparison of the midpoint of G_{ii}^{trans} from the data and the Lorentzian ansatz for different η (see section 5.3). Works for bottomonium and charmonium at every temperature.
- Comparison of the first thermal ratio $R^{2,0}$ from the data to the Lorentzian ansatz for different η (see section 5.4). Works for charmonium above $1.3T_c$ and for bottomonium at the highest temperature.

Each of these approaches has also been crosschecked with the Gaussian ansatz (see appendix). To get a final result, the different estimates are combined in this section.

First, it can be seen that the statement $\eta^c > \eta^b$ predicted in 5.2 is confirmed in the more quantitative analysis in 5.3 and 5.4. For charmonium, the results in 5.3 do not seem too reliable, as the transport peak extends far into the bound state region. This is slightly better in the approach with the thermal moments. For bottomonium on the other hand, the thermal moment analysis does not provide a deeper understanding, as for most temperatures no intersection ranges were found. But there, the direct comparison of the midpoint seems more promising. So far, we used a Lorentzian ansatz for the transport peak, but the same analysis has been carried out for the Gaussian ansatz with the results shown in the appendix. There, we observe similar tendencies: The thermal moment analysis is more promising with charmonium correlators, while the comparison to the midpoint works better with bottomonium correlators.

Regarding the systematic uncertainties, one should note that the results at a temperature of $2.25T_c$ are the most reliable for mainly two reasons. First, the quark number susceptibility included in the transport peak can be most accurately determined here. For the other temperatures T we continuum extrapolated a ratio of the quark number susceptibility at T and $T' = 2.25T_c$, as argued in section 4.2. This ratio is by far not as certain as the extrapolation of χ_q at $2.25T_c$. And second, as the transport part of the correlator is estimated by subtracting the perturbative result from the whole correlator, the method is more valid at high temperatures, where perturbation theory is more reliable. Due to this, the bottomonium result is also more reliable than the charmonium result.

Fig. 5.17 shows an overview of all the results for the heavy quark diffusion coefficient we obtained with the different methods. As already argued, not all results are equally trustworthy. Thus, Fig. 5.18 shows another version of this plot, where only the following results are taken into account:

- The bottomonium results from a comparison of the midpoint with the Lorentzian ansatz for temperatures of $1.3T_c$ and above.

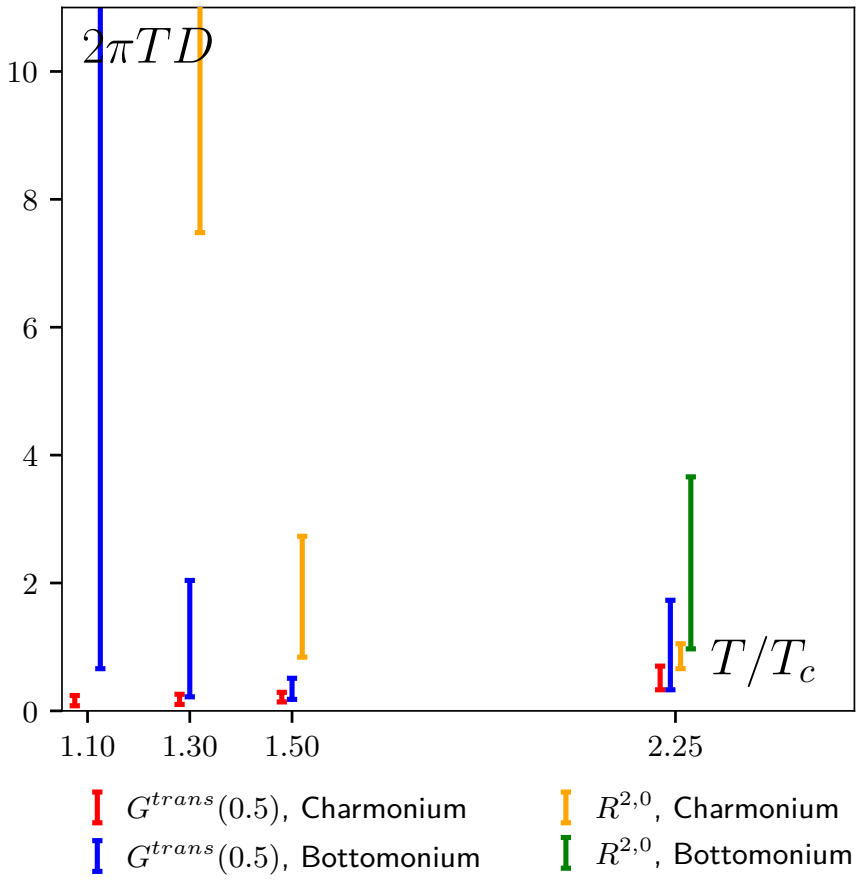

Figure 5.17: Overview of the different results for $2\pi TD$ from different ansätze.

- The results for charmonium and bottomonium from the thermal ratios, determined with the Lorentzian ansatz.

There is no obvious temperature dependence visible.

If we now compare our results to the current state of research presented in 2.4.3, we see that our value of $2\pi TD$ falls on the lower side of the spectrum. As the errors are still quite large, we do not quote an exact result, but rather constrain the range of $2\pi TD$. The lowest bound of the reliable results for charm is $2\pi TD = 0.66$, while the highest value is around $2\pi TD = 2.73$. We thus conclude $2\pi TD^c \in [0.66, 2.73]$. For bottom we find $2\pi TD^b \in [0.18, 3.66]$. It should be noted that the result from bottomonium correlators is more reliable as transport and bound state region are clearly more seperated in the corresponding spectral function. But since the result from charmonium

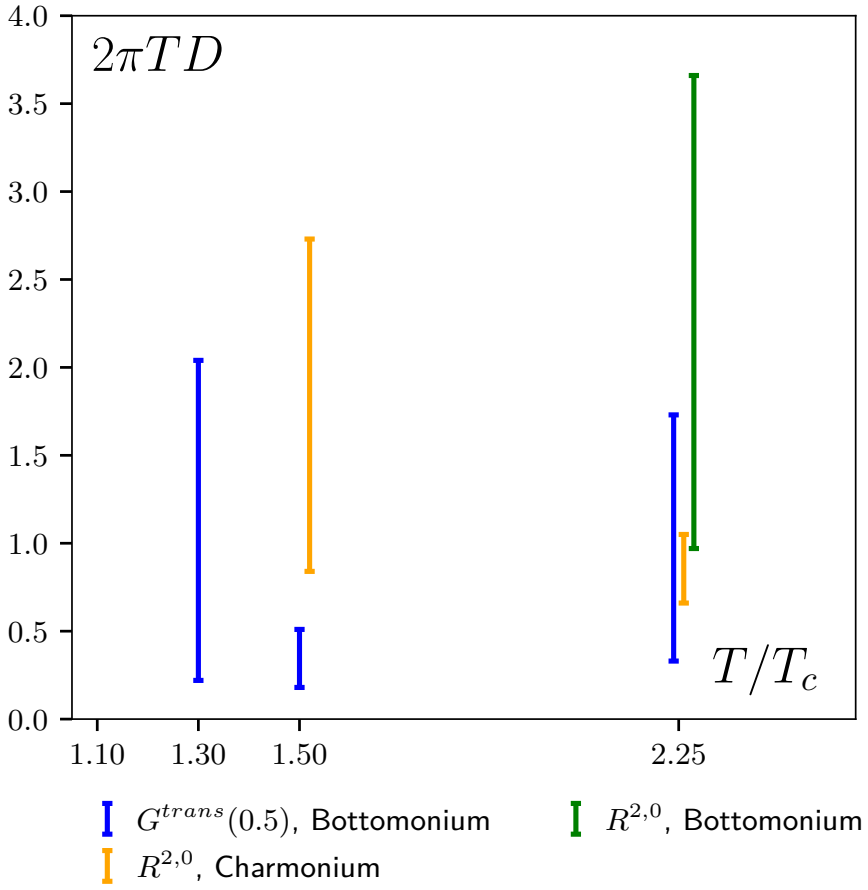

Figure 5.18: Like Fig. 5.17, but only for the more reliable results.

correlators is included in the bottomonium result, we still quote it here.

Within errors, our findings are in agreement with a lot of the results presented earlier, especially the MEM results in [51]. Our results partly overlap with the two newer studies on the heavy quark momentum diffusion coefficient κ [48, 49]. Older studies on κ on the other hand hint to slightly higher values for $2\pi TD$ [47, 50]. The distribution of the different lattice results is especially interesting since this work and the MEM study both work with finite quark masses, while the studies on the heavy quark momentum diffusion coefficients are all carried out in the heavy quark limit. As [57] argues, corrections of order $\mathcal{O}(T/M)$ are to be expected when going to finite masses. The result of this work together with the MEM study could hint to those corrections and can maybe be used to gain further insight.

The experimental results from ALICE [53] and STAR [54] show a small overlap with our range. Our lower bounds seems underestimated, as no other result for $2\pi TD$ extends to such small values, but the upper bounds fit very well into the picture. Thus, it seems reasonable to add our values into the overview picture to get to the final Fig. 5.19. Within this picture, our values take a special place. So far, every result from lattice QCD has been either based on the limit of an infinitely large quark mass (κ-studies) and/or obtained on non-continuum extrapolated data (MEM studies). This is the first investigation based on continuum extrapolated mesonic correlation functions for charm and bottom quarks. So far, this analysis has only been carried out in the quenched approximation, but the procedure presented in this work could be a basis for future studies in full QCD.

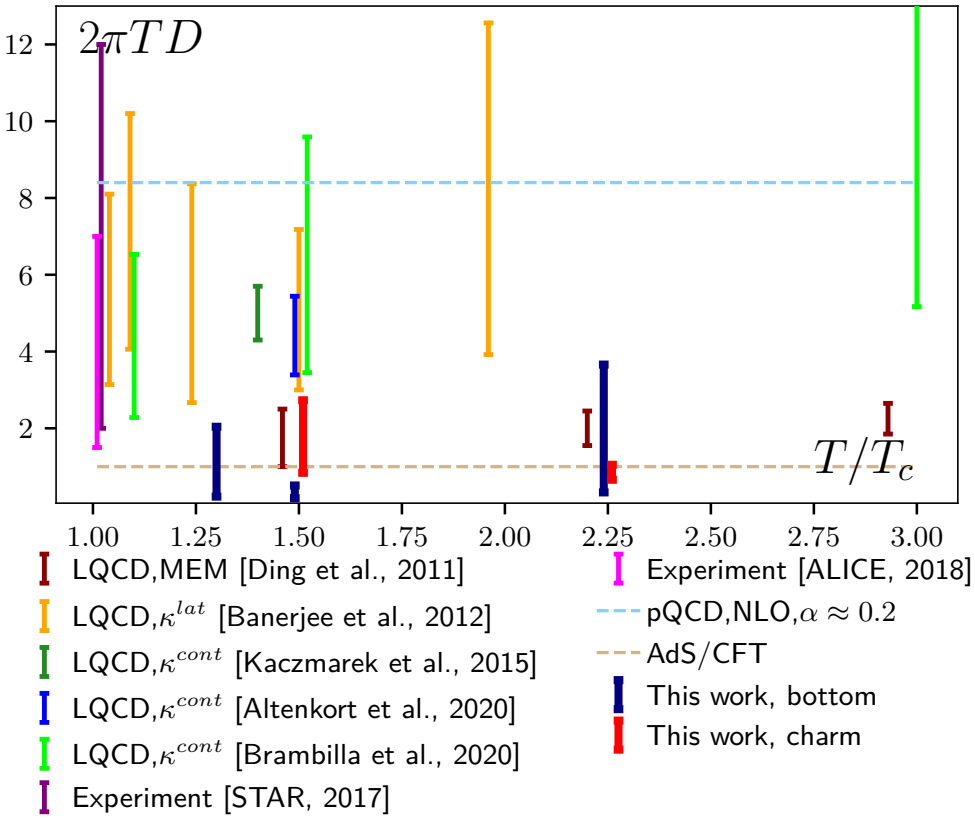

Figure 5.19: The overview of selected results for $2\pi TD$ (see section 2.4.3, Fig. 2.9) complemented by our final results. It can be seen that our results agree with many other approaches, especially the experimental results (within errors), the MEM study and the newest investigation on the heavy quark momentum diffusion coefficient κ.

Chapter 6

Conclusion

In this work, we gained insight into thermal modifications of charmonia and bottomonia by comparing LQCD results and a perturbative ansatz.

On the lattice side, we worked with correlators measured on very large and fine lattices in the quenched approximation using clover-improved Wilson fermions. In total, four different lattice spacings were included in the analysis, the coarsest being $a = 0.018$fm and the finest $a = 0.009$fm. We performed a continuum extrapolation using a relatively new method that includes a mass-interpolation and obtained the correlation functions for five different temperatures, 0.75, 1.1, 1.3, 1.5 and $2.25T_c$. On the correlator level, we drew first conclusions on the behaviour of charmonia and bottomonia at different temperatures. From a comparison of pseudoscalar correlators, which show only little temperature dependence and vector correlators, showing a large temperature dependence around the midpoint, it can be concluded that most of the temperature dependence originates from the transport contribution. It can also be seen that bottomonium shows less temperature dependence than charmonium. These observations and their interpretation are, however, mostly intuition based.

To gain a more profound understanding, we combined our data with a perturbative approach. Above T_c, we compare to a perturbative spectral function, which is constructed by combining vacuum asymptotics at high frequencies and pNRQCD at low to intermediate frequencies via a matching procedure. We accounted for the two major sources of systematical uncertainties: First, we introduced an overall normalization factor to absorb uncertainties in the renormalization of lattice correlators. Second, we implemented a mass shift, since the relation between the $\overline{\text{MS}}$ and pole mass used in the perturbative calculation is not exactly known. These two parameters were determined in a fit to the continuum correlators. In the pseudoscalar channel, this procedure showed that only minor modifications are needed to describe the correlators with the perturbative spectral function. The normal-

ization factor is close to unity and the mass shift small. The errors on both parameters, determined from performing the analysis on different bootstrap samples, are reasonable. We thus obtained pseudoscalar spectral functions for charmonium and bottomonium at four different temperatures above T_c. A crosscheck with MEM confirmed our results.

In the vector channel the presence of the transport peak prohibited us from applying the same procedure directly to the correlator. Instead, we fitted our model spectral function to differences of neighbouring correlators. The results are quite similar to those in the pseudoscalar channel. Again, the normalization factor was around 1 and the mass shift close to 0. Again, after the crosscheck with MEM, we conclude that our model is suitable to describe our correlators.

In both channels, we did not observe a resonance peak for charmonium, while for bottomonium, one thermally broadened resonance peak improved the agreement with the data. This one peak lies close to the expected peak for the ground states Υ and η_b and is melted at $2.25T_c$, which is consistent with the predictions for Υ and η_b from other studies.

The difference of the original vector correlator and our model obtained by fitting to the difference correlator contains information on the low frequency part of the spectral function, namely the transport peak. As the related transport coefficients are an important quantity for understanding heavy ion collisions, we investigate the transport contribution further. We assume a Lorentzian ansatz for the analysis of the heavy quark diffusion coefficient and the drag coefficient and relate the two quantities with the Einstein relation. Our main focus lies on the midpoint as the transport contribution is more dominant there than for small temporal distances. By comparing the ratios of charmonium and bottomonium contributions, we can already conclude that the drag coefficient of charmonium is larger than the bottomonium one. To quote numbers, we compare the correlator obtained from the Lorentzian ansatz for different values of the drag coefficient to our data. Including the error on the data and an uncertainty of 10% in the mass, we are able to find an overlap region. For bottomonium, this procedure lead to a range in which we would expect our drag coefficient and the heavy quark diffusion coefficient respectively. For charmonium this unfortunately does not produce reliable results. The obtained drag coefficient is so large, that the transport region extends into the bound state region. Instead, we tried another method. By Taylor-expanding the correlator around the midpoint, we obtain the thermal moments. The ratio of the first thermal moments is then analyzed further. We again compare to the Lorentzian ansatz and determine the overlap. This method works significantly better for charmonium.

As a check, we repeated every step of our analysis with the Gaussian ansatz, obtaining similar values. By combining the results, we can finally quote a range for the heavy quark diffusion coefficient. As the bottomonium

results are more reliable due to the clear separation of transport and bound state part in the spectral function, we examine charm and bottom seperately. We obtain a range of $2\pi TD = 0.18..3.66$ for bottom and a range of $2\pi TD = 0.66..2.73$ for charm, which is included in the bottom range and can thus also be trusted. Our values match the results of many different approaches from other methods and hint to the smaller end of the spectrum.

So far, the method for comparing perturbative correlation functions to lattice correlators was applied to quenched lattices, but the methodology developed by us provides the basis for extending the studies to full QCD. There, however, we would expect some changes in the results. Quenched QCD is believed to agree better with perturbation theory, as the critical temperature there is around two times larger than in full QCD, while the coupling is smaller. Due to these differences, additional resonance peaks might be needed and are expected from non-relativistic models i.e. in [15]. For charmonium, one could expect at least one peak for the ground state at the temperatures analyzed in this study, at the lowest temperature, there might even be a second state. For bottomonium we would not expect the behaviour of the resonance peak to change much, but there would probably be more bound states, at least for the lower temperatures. With the onset of computational power, full QCD studies will soon be possible.

Appendix A

Renormalization Constants

The following tables give an overview of the renormalization constants used in this work. The calculation was done according to 3.5. We present all available renormalization constants, even though we only use the following:

- In the vector channel we rely mostly on builing a renormalization independent ratio with the quark number susceptibility, which is then renormalized non-perturbatively with the constants from tab. A.1 for the case of massive quarks.
- In the pseudoscalar channel, where a non-perturbative determination is not possible, we use one-loop (tab. A.2) as well as two-loop results (tab. A.3), both including the mass correction and a correction factor for the anomalous dimension (tab. A.4). From the differences, the systematic uncertainties can be estimated.

β	κ	$Z_V^{np,massless}$	$Z_V^{np,massive}$	Z_V^{1loop}	Z_V^{2loop}
7.192	0.131940	0.8421264500921962	0.916394139906	0.918547	0.855159
	0.131500		0.929882288784	0.931763	0.867464
	0.131000		0.945319713862	0.946890	0.881546
	0.130000		0.97655081229	0.977492	0.910037
	0.128000		1.04047696688	1.040131	0.968353
	0.122570		1.22455738023	1.220505	1.136279
7.394	0.132008	0.8491849220385659	0.91120932568	0.912623	0.856702
	0.131500		0.926709021275	0.927841	0.870988
	0.131000		0.942082013823	0.942934	0.885156
	0.129000		1.00476568886	1.004479	0.942930
	0.124772		1.14389338468	1.141146	1.071223
7.544	0.132360	0.8539928563366839	0.898183696476	0.899968	0.849346
	0.132200		0.903014142349	0.904716	0.853826
	0.131800		0.915141566775	0.916635	0.865075
	0.131000		0.939618597449	0.940692	0.887779
	0.129500		0.986328143437	0.986601	0.931105
	0.126410		1.08604365708	1.084606	1.023598
7.793	0.132210	0.8612733107488421	0.898744883533	0.900061	0.855616
	0.132090		0.902361766986	0.903621	0.859000
	0.131810		0.910826772497	0.911952	0.866920
	0.131250		0.92786513559	0.928722	0.882862
	0.130190		0.960517635748	0.960860	0.913413
	0.127980		1.03033445432	1.029578	0.978737

Table A.1: Renormalization constants in the vector channel. *np* denotes the non-perturbatively determined constants.

β	u_0	$g^2_{\overline{\rm MS}}(\frac{1}{a})$	$Z_{PS}^{massless}(\mu = \frac{1}{a})$	κ	$Z_{PS}^{massive}(\mu = \frac{1}{a})$
7.192	0.908950(3)	1.523	0.85615	0.13194	0.930561
				0.13150	0.943949
				0.13100	0.959271
				0.13000	0.990270
				0.12800	1.053720
				0.12257	1.236431
7.394	0.912417(3)	1.443000	0.862247	0.132008	0.923889
				0.131500	0.939293
				0.131000	0.954571
				0.129000	1.016869
				0.124772	1.155206
7.544	0.9148340(2)	1.388	0.866449	0.13236	0.910628
				0.13220	0.915431
				0.13180	0.927490
				0.13100	0.951829
				0.12950	0.998276
				0.12641	1.097431
7.793	0.9185380(1)	1.308	0.872757	0.13221	0.910068
				0.13209	0.913667
				0.13181	0.922091
				0.13125	0.939045
				0.13019	0.971537
				0.12798	1.041011

Table A.2: One-loop Renormalization constants in the pseudoscalar channel.

β	u_0	$g^2_{\overline{\rm MS}}(\frac{1}{a})$	$Z_{PS}^{massless}(\mu = \frac{1}{a})$	κ	$Z_{PS}^{massive}(\mu = \frac{1}{a})$
7.192	0.908950(3)	1.523	0.835023	0.13194	0.907590
				0.13150	0.920647
				0.13100	0.935592
				0.13000	0.965825
				0.12800	1.027709
				0.12257	1.205910
7.394	0.912417(3)	1.443000	0.843087	0.132008	0.903359
				0.131500	0.918421
				0.131000	0.933360
				0.129000	0.994273
				0.124772	1.129536
7.544	0.9148340(2)	1.388	0.848597	0.13236	0.891865
				0.13220	0.896570
				0.13180	0.908381
				0.13100	0.932218
				0.12950	0.977708
				0.12641	1.074820
7.793	0.9185380(1)	1.308	0.856738	0.13221	0.893364
				0.13209	0.896897
				0.13181	0.905166
				0.13125	0.921810
				0.13019	0.953705
				0.12798	1.021903

Table A.3: Two-loop Renormalization constants in the pseudoscalar channel.

β	additional factor
7.192	0.6454
7.544	0.5999
7.793	0.5726

Table A.4: Additional factors for the mass correction.

Appendix B

Results for the Gaussian Ansatz

In this section, the analysis in chapter 5 is repeated for the Gaussian ansatz [14]

$$\rho_{ii}^{trans,G}(\omega) = 3\pi\chi_q \frac{T}{M}\frac{\omega}{\sqrt{2\pi\eta_G^2}} e^{-\frac{\omega^2}{2\eta_G^2}} \quad \text{with} \quad \eta_G = \sqrt{\frac{\pi}{2}}\frac{T}{MD} = \sqrt{\frac{\pi}{2}}\eta. \tag{B.1}$$

Again, we made use of the Einstein relation to replace $2\pi TD$ in terms of η.

B.1 Comparison of Charmonium and Bottomonium

We start with the qualitative comparison between the drag coefficients for bottom and charm, presented in 5.2. Since this time, we only need to expand the kernel and not the cut-off term, the expansion changes to

$$\frac{\cosh\left(\omega(1/2T - 1/2T)\right)}{\sinh(\omega/2T)} = \frac{2T}{\omega} - \frac{\omega}{12T} + \frac{7\omega^3}{2880T^3} - \frac{31\omega^5}{483840T^5} + \mathcal{O}\left(\omega^7\right). \tag{B.2}$$

The factors f_i in the approximated correlator

$$\frac{G_{ii}^{trans,G}(\tau T = 0.5)}{\chi_q T} = \frac{T}{M}\left(f_1 + f_2 + f_3 + f_4 + \mathcal{O}(\omega^7)\right), \tag{B.3}$$

read

$$f_1 = \frac{2\Gamma\left(\frac{\omega_{cut}}{\sqrt{2}\eta_G}\right)}{\eta_G} \tag{B.4}$$

$$f_2 = \frac{\eta_G\left(\sqrt{\frac{2}{\pi}}\omega_{cut}\exp\left(\frac{-\omega_{cut}^2}{2\eta_G^2}\right) - \eta_G\Gamma\left(\frac{\omega_{cut}}{\sqrt{2}\eta_G}\right)\right)}{8T} \tag{B.5}$$

$$f_3 = \frac{7\eta_G\left(3\eta_G^3\Gamma\left(\frac{\omega_{cut}}{\sqrt{2}\eta_G}\right) - \sqrt{\frac{2}{\pi}}\omega_{cut}\exp\left(\frac{-x^2}{2\eta_G^2}\right)(3\eta_G^2+\omega_{cut}^2)\right)}{1920T^3} \tag{B.6}$$

$$f_4 = \frac{31\left(15\sqrt{\frac{\pi}{2}}\eta_G^7\Gamma\left(\frac{\omega_{cut}}{\sqrt{2}\eta_G}\right) - \eta_G^2\omega_{cut}\exp\left(\frac{\omega_{cut}}{2\eta_G^2}\right)(15\eta_G^4+\omega_{cut}^4+5\eta_G^2\omega_{cut}^2)\right)}{161280\sqrt{2\pi}\eta T^5} \tag{B.7}$$

with the error function Γ. Again, we only take f_1 into consideration and arrive at the ratio

$$\frac{G_{ii,c}^{trans}/\chi_q^c}{G_{ii,b}^{trans}/\chi_q^b} \approx \frac{M_b}{M_c}\frac{\Gamma\left(\frac{\omega_{cut}}{\sqrt{2}\eta_G^c}\right)\eta_G^b}{\Gamma\left(\frac{\omega_{cut}}{\sqrt{2}\eta_G^b}\right)\eta_G^c} \tag{B.8}$$

which only depends on the ratio of the masses, which is known to be of approximately 3, the upper limit of the integration ω_{cut} and η_G. When comparing to the data in Fig. 5.2, our previous statement that $\eta^c > \eta^b$ holds for the Gaussian ansatz.

B.2 Estimating the Transport Coefficients

For a more quantitative result, we continue by finding an overlap between our data (including errors) and the Gaussian ansatz with physical charm and bottom quark masses and an uncertainty of 10%. This is done analoguously to section 5.3 Figs. B.1,B.2 and tab. B.1 show the results. The dependence on the upper integration limit was similar as for the Lorentzian ansatz, so we again choose infinity as this is most correct. Unfortunately, we encounter the same problems for charmonium. Again, the transport peak stretches too far out and reaches into the bound state region. But for bottomonium this method works with the Gaussian ansatz as well. We find a similar lower bound of $2\pi TD = 0.12$. The upper bound $2\pi TD = 10.88$ is probably overestimated, but the range includes the results we found for the Lorentzian ansatz and thus does not contradict our previous findings.

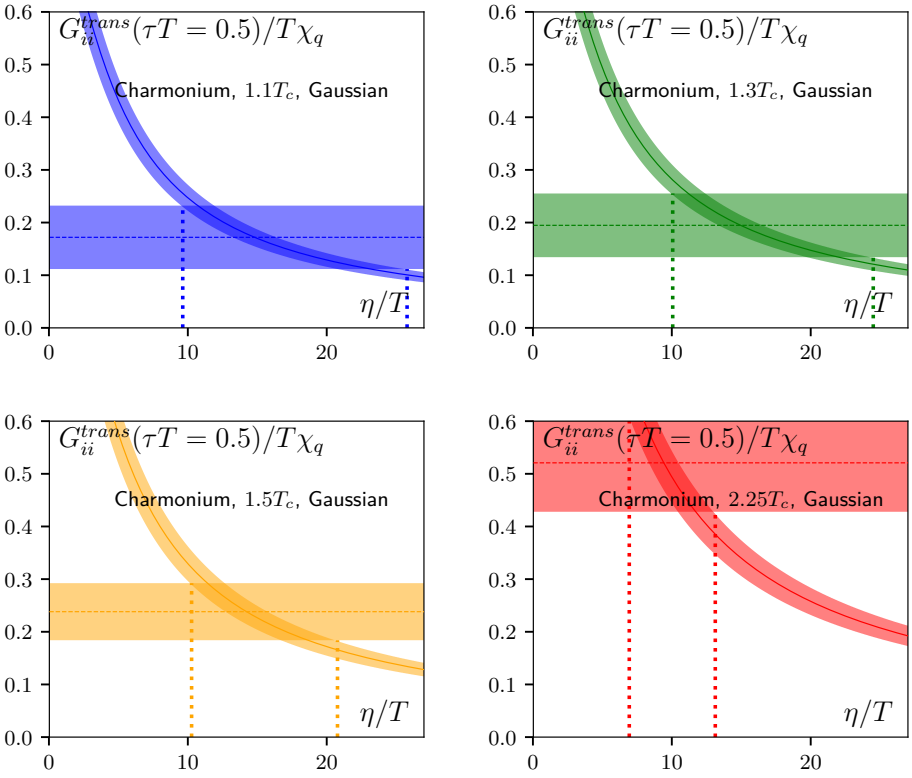

Figure B.1: Like Fig. 5.8, but for the gaussian ansatz.

	Charmonium		Bottomonium	
T/T_c	η/T	$2\pi TD$	η/T	$2\pi TD$
1.1	9.63-25.79	0.06-0.18	0.05-2.01	0.27-10.88
1.3	10.06-24.50	0.08-0.20	1.10-4.45	0.14-0.56
1.5	10.27-19.78	0.11-0.23	2.75-5.90	0.12-0.26
2.25	6.94-13.13	0.27-0.50	1.66-4.96	0.22-0.64

Table B.1: Like tab. 5.1, but for for the Gaussian ansatz.

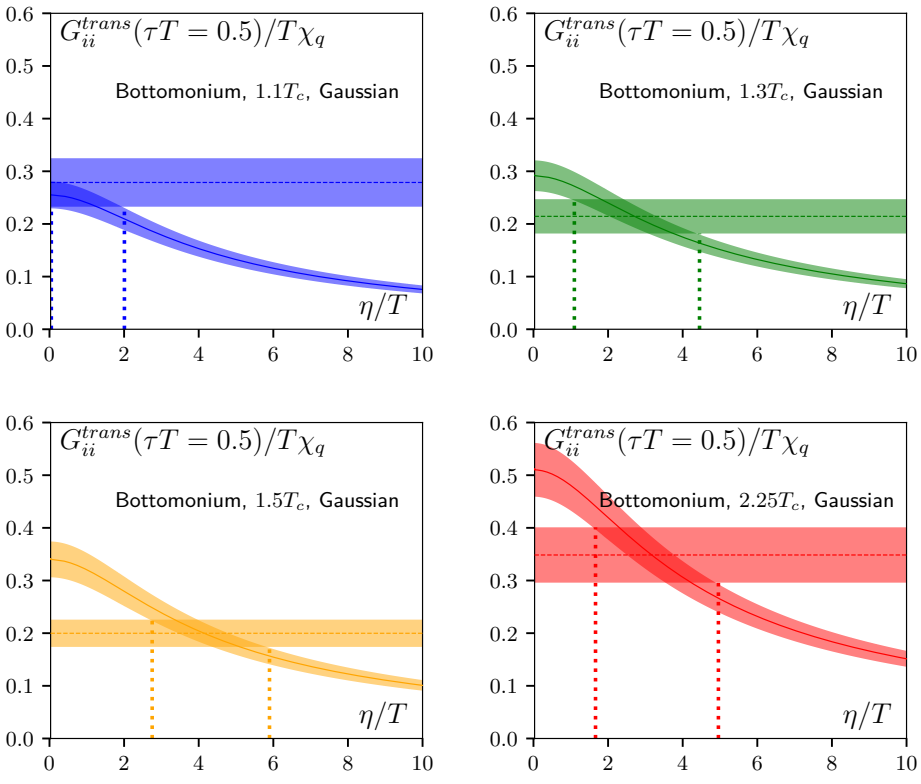

Figure B.2: Like Fig. 5.4, but for the gaussian ansatz.

B.3 Thermal Moments

We also repeat the analysis of thermal moments in section 5.4 for the Gaussian ansatz. The range, in which data and the Gaussian ansatz agree within errors is seen in Fig. B.3 and tab. B.2. As with the Lorentzian ansatz, this method works better for charmonium. For bottomonium, only the highest temperature shows an intersection.

	Charmonium		Bottomonium	
T/T_c	η/T	$2\pi TD$	η/T	$2\pi TD$
1.1	-	-	-	-
1.3	<0.29	>6.77	-	-
1.5	0.78-3.07	0.76-2.97	-	-
2.25	3.64-6.11	0.57-0.96	0.10-1.13	0.95-10.33

Table B.2: The ranges for η and $2\pi TD$ determined by comparing the first thermal ratio from the data with the gaussian model.

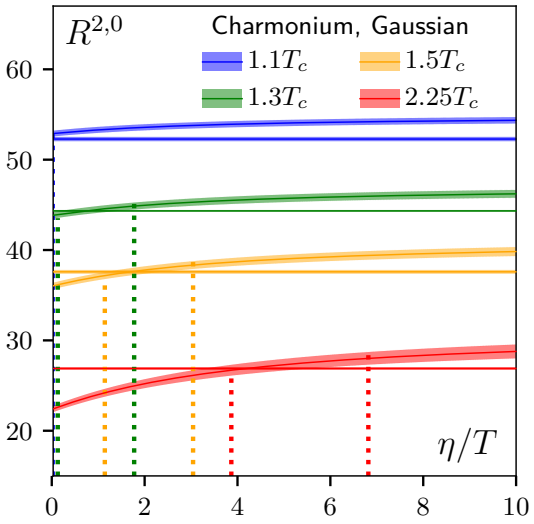

Figure B.3: Like Fig. 5.16, but for the Gaussian ansatz.

B.4 Combining the Results

After combining the results from the Gaussian ansatz and removing the less reliable results as we did for the Lorentzian ansatz, we obtain $2\pi TD^c = 0.57..2.97$ and $2\pi TD^b = 0.12..10.88$. The charm range agrees very well with the previous results. For bottom, there is almost exactly the same lower bound, but the upper limit seems overestimated. Still, the Gaussian results do not contradict but support the findings from the Lorentzian ansatz. Since the Lorentzian ansatz has a better theoretical motivation, we believe those results to be more reliable.

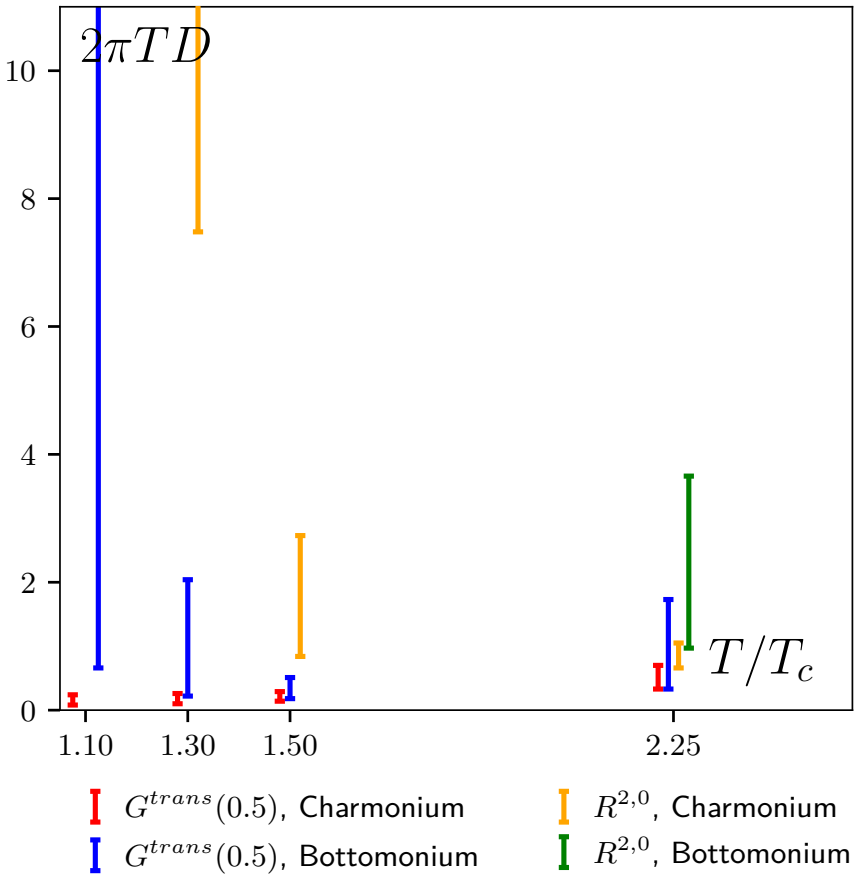

Figure B.4: Overview of the different results for $2\pi TD$. Like Fig. 5.17, but for the Gaussian ansatz.

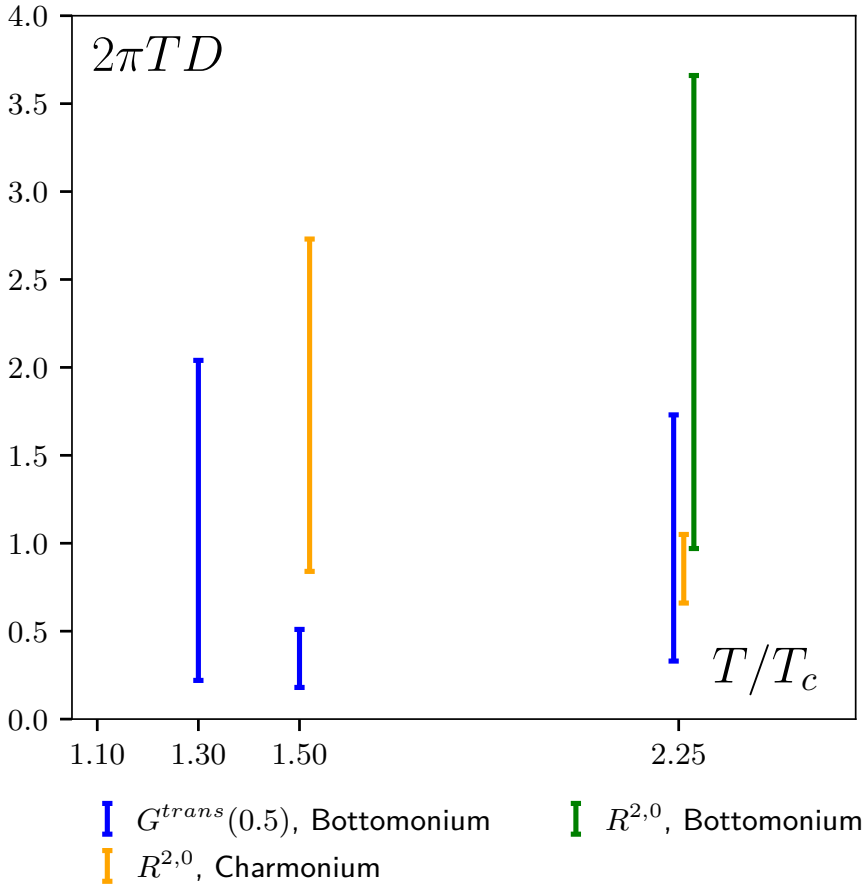

Figure B.5: Like Fig. B.4, but only for the more reliable results.

Bibliography

[1] Particle Data Group collaboration, *Review of Particle Physics*, *PTEP* **2020** (2020) 083C01.

[2] D. J. Gross and F. Wilczek, *Ultraviolet Behavior of Nonabelian Gauge Theories*, *Phys. Rev. Lett.* **30** (1973) 1343.

[3] K. G. Wilson, *Confinement of quarks*, *Phys. Rev. D* **10** (1974) 2445.

[4] J. C. Collins and M. J. Perry, *Superdense Matter: Neutrons or Asymptotically Free Quarks?*, *Phys. Rev. Lett.* **34** (1975) 1353.

[5] T. Matsui and H. Satz, *J/ψ Suppression by Quark-Gluon Plasma Formation*, *Phys. Lett. B* **178** (1986) 416.

[6] R. Arnaldi, *J/ψ production in p-A and A-A collisions at fixed target experiments*, *Nuclear Physics A* **830** (2009) 345c.

[7] G. Aad, B. Abbott, J. Abdallah, A. A. Abdelalim, A. Abdesselam, O. Abdinov et al., *Measurement of the centrality dependence of J/ψ yields and observation of Z production in lead–lead collisions with the ATLAS detector at the LHC*, *Physics Letters B* **697** (2011) 294.

[8] CMS Collaboration, *Suppression of non-prompt J/psi, prompt J/psi, and Y(1S) in PbPb collisions at sqrt(sNN) = 2.76 TeV*, *Journal of High Energy Physics* **2020** (2012) 063.

[9] B. Abelev, J. Adam, D. Adamová, A. M. Adare, M. M. Aggarwal, G. A. Rinella et al., *J/ψ Suppression at Forward Rapidity in Pb-Pb Collisions at $\sqrt{s_{NN}}$ =2.76 TeV*, *Physical Review Letters* **109** (2012) 072301.

[10] S. Chatrchyan, V. Khachatryan, A. M. Sirunyan, A. Tumasyan, W. Adam, E. Aguilo et al., *Observation of Sequential Υ Suppression in PbPb Collisions*, *Physical Review Letters* **109** (2012) 222301.

[11] A. K. Chaudhuri, *Sequential melting of charmonium states in an expanding quark–gluon plasma and J/ψ suppression at RHIC and LHC*

energy collisions, *Journal of Physics G: Nuclear and Particle Physics* **35** (2008) 095107.

[12] M. Aaboud, G. Aad, B. Abbott, O. Abdinov, B. Abeloos, S. H. Abidi et al., *Prompt and non-prompt J/ψ and ψ(2S) suppression at high transverse momentum in* 5.02 TeV *Pb+Pb collisions with the ATLAS experiment*, *The European Physical Journal C* **78** (2018) 762.

[13] A. Rothkopf, *Heavy quarkonium in extreme conditions*, *Physics Reports* **858** (2020) 1.

[14] P. Petreczky and D. Teaney, *Heavy quark diffusion from the lattice*, *Phys.Rev.* **D73** (2006) 014508.

[15] Y. Burnier, O. Kaczmarek and A. Rothkopf, *Quarkonium at finite temperature: Towards realistic phenomenology from first principles*, *JHEP* **12** (2015) 101.

[16] C. Miao, A. Mocsy and P. Petreczky, *Quarkonium spectral functions with complex potential*, *Nucl. Phys. A* **855** (2011) 125.

[17] C. Gattringer and C. B. Lang, *Quantum chromodynamics on the lattice*, vol. 788. Springer, Berlin, 2010, 10.1007/978-3-642-01850-3.

[18] R. Kubo, *Statistical-Mechanical Theory of Irreversible Processes. I. General Theory and Simple Applications to Magnetic and Conduction Problems*, *Journal of the Physical Society of Japan* **12** (1957) 570.

[19] P. C. Martin and J. Schwinger, *Theory of Many-Particle Systems. I*, *Phys. Rev.* **115** (1959) 1342.

[20] M. Asakawa, T. Hatsuda and Y. Nakahara, *Maximum entropy analysis of the spectral functions in lattice QCD*, *Prog. Part. Nucl. Phys.* **46** (2001) 459.

[21] S. Fuchs, T. Pruschke and M. Jarrell, *Analytic continuation of quantum Monte Carlo data by stochastic analytical inference*, *Phys. Rev. E* **81** (2010) 056701.

[22] S. Datta, F. Karsch, P. Petreczky and I. Wetzorke, *Behavior of charmonium systems after deconfinement*, *Phys. Rev. D* **69** (2004) 094507.

[23] P. Petreczky, S. Datta, F. Karsch and I. Wetzorke, *Charmonium at finite temperature*, *Nucl. Phys. B Proc. Suppl.* **129** (2004) 596.

[24] H. T. Ding, A. Francis, O. Kaczmarek, F. Karsch, H. Satz and W. Soeldner, *Charmonium correlation and spectral functions at finite temperature*, *PoS* **LATTICE2010** (2010) 180.

[25] H.-T. Ding, A. Francis, O. Kaczmarek, F. Karsch, H. Satz and W. Soeldner, *Charmonium properties in hot quenched lattice QCD*, *Phys. Rev. D* **86** (2012) 014509.

[26] G. Aarts and J. Resco, *Continuum and lattice meson spectral functions at nonzero momentum and high temperature*, *Nuclear Physics B* **726** (2005) 93.

[27] A. Jakovác, P. Petreczky, K. Petrov and A. Velytsky, *Quarkonium correlators and spectral functions at zero and finite temperature*, *Physical Review D* **75** (2007) 014506.

[28] A. Bazavov, P. Petreczky and A. Velytsky, *Quarkonium at finite temperature*, *Quark-Gluon Plasma 4* (2010) 61.

[29] T. Umeda, K. Nomura and H. Matsufuru, *Charmonium at finite temperature in quenched lattice QCD*, *The European Physical Journal C* **39** (2004) 9.

[30] M. Asakawa and T. Hatsuda, *J/ψ and η_c in the Deconfined Plasma from Lattice QCD*, *Physical Review Letters* **92** (2004) 012001.

[31] F. Karsch, S. Datta, E. Laermann, P. Petreczky, S. Stickan and I. Wetzorke, *Hadron correlators, spectral functions and thermal dilepton rates from lattice QCD*, *Nuclear Physics A* **715** (2003) 701c.

[32] G. Aarts, C. Allton, M. B. Oktay, M. Peardon and J.-I. Skullerud, *Charmonium at high temperature in two-flavor QCD*, *Physical Review D* **76** (2007) 094513.

[33] H.-T. Ding, O. Kaczmarek, S. Mukherjee, H. Ohno and H.-T. Shu, *Stochastic reconstructions of spectral functions: Application to lattice QCD*, *Physical Review D* **97** (2018) 094503.

[34] N. Brambilla, J. Ghiglieri, A. Vairo and P. Petreczky, *Static quark-antiquark pairs at finite temperature*, *Phys. Rev. D* **78** (2008) 014017.

[35] A. Mócsy and P. Petreczky, *Can quarkonia survive deconfinement?*, *Phys. Rev. D* **77** (2008) 014501.

[36] A. Mócsy and P. Petreczky, *Color Screening Melts Quarkonium*, *Phys. Rev. Lett.* **99** (2007) 211602.

[37] Y. Burnier, H.-T. Ding, O. Kaczmarek, A.-L. Kruse, M. Laine, H. Ohno et al., *Thermal quarkonium physics in the pseudoscalar channel*, *JHEP* **11** (2017) 206.

[38] H.-T. Ding, O. Kaczmarek, A.-L. Lorenz, H. Ohno, H. Sandmeyer and H.-T. Shu, *Charm and beauty in the deconfined plasma from lattice QCD*, *Work in Progress* .

[39] Y. Burnier, M. Laine and M. Vepsäläinen, *Heavy quark medium polarization at next-to-leading order*, *Journal of High Energy Physics* **2009** (2009) 008.

[40] Y. Burnier and M. Laine, *Towards flavour diffusion coefficient and electrical conductivity without ultraviolet contamination*, *Eur. Phys. J.* **C72** (2012) 1902.

[41] Y. Burnier, M. Laine and M. Vepsalainen, *Heavy quarkonium in any channel in resummed hot QCD*, *JHEP* **01** (2008) 043.

[42] M. Laine, *A Resummed perturbative estimate for the quarkonium spectral function in hot QCD*, *JHEP* **05** (2007) 028.

[43] D. Forster, *Hydrodynamic Fluctuations, Broken Symmetry, and Correlation Functions*. Advanced Book Classics. Perseus Books, 1976, https://doi.org/10.1002/bbpc.19760800922.

[44] R. Kubo, *Statistical-Mechanical Theory of Irreversible Processes. I. General Theory and Simple Applications to Magnetic and Conduction Problems*, *Journal of the Physical Society of Japan* **12** (1957) 570.

[45] A. Beraudo, A. De Pace, W. Alberico and A. Molinari, *Transport properties and Langevin dynamics of heavy quarks and quarkonia in the Quark Gluon Plasma*, *Nuclear Physics A* **831** (2009) 59.

[46] P. Kovtun, D. T. Son and A. O. Starinets, *Holography and hydrodynamics: diffusion on stretched horizons*, *Journal of High Energy Physics* **2003** (2003) 064.

[47] O. Kaczmarek, *Continuum estimate of the heavy quark momentum diffusion coefficient κ*, *Nucl. Phys.* **A931** (2014) 633.

[48] L. Altenkort, A. M. Eller, O. Kaczmarek, L. Mazur, G. D. Moore and H.-T. Shu, *Heavy quark momentum diffusion from the lattice using gradient flow*, *Physical Review D* **103** 014511.

[49] N. Brambilla, V. Leino, P. Petreczky and A. Vairo, *Lattice QCD constraints on the heavy quark diffusion coefficient*, *Physical Review D* **102** (2020) 074503.

[50] D. Banerjee, S. Datta, R. Gavai and P. Majumdar, *Heavy quark momentum diffusion coefficient from lattice QCD*, *Physical Review D* **85** (2012) 014510.

[51] H.-T. Ding, A. Francis, O. Kaczmarek, F. Karsch, H. Satz and W. Söldner, *Heavy quark diffusion from lattice QCD spectral functions*, *Journal of Physics G: Nuclear and Particle Physics* **38** (2011) 124070.

[52] S. Caron-Huot and G. D. Moore, *Heavy Quark Diffusion in Perturbative QCD at Next-to-Leading Order*, *Physical Review Letters* **100** (2008) 052301.

[53] S. Acharya, D. Adamova, J. Adolfsson, M. M. Aggarwal, G. A. Rinella, M. Agnello et al., *D-Meson Azimuthal Anisotropy in Midcentral Pb-Pb Collisions at sNN=5.02 TeV*, *Physical Review Letters* **120** (2018) 102301.

[54] L. Adamczyk, J. Adkins, G. Agakishiev, M. Aggarwal, Z. Ahammed, N. Ajitanand et al., *Measurement of D0 Azimuthal Anisotropy at Midrapidity in Au+Au Collisions at sNN=200 GeV*, *Physical Review Letters* **118** (2017) 212301.

[55] J. Casalderrey-Solana and D. Teaney, *Heavy quark diffusion in strongly coupled N=4 Yang-Mills theory*, *Physical Review D* **74** (2006) 085012.

[56] A. Francis, O. Kaczmarek, M. Laine, T. Neuhaus and H. Ohno, *Nonperturbative estimate of the heavy quark momentum diffusion coefficient*, *Physical Review D* **92** (2015) 116003.

[57] A. Bouttefeux and M. Laine, *Mass-suppressed effects in heavy quark diffusion*, *Journal of High Energy Physics* **2020** (2020) 150.

[58] G. D. Moore and D. Teaney, *How much do heavy quarks thermalize in a heavy ion collision?*, *Physical Review C* **71** (2005) 064904.

[59] S. S. Gubser, *Comparing the drag force on heavy quarks inN=4super-Yang-Mills theory and QCD*, *Physical Review D* **76** (2007) 126003.

[60] Y. Burnier and M. Laine, *Massive vector current correlator in thermal QCD*, *JHEP* **11** (2012) 086.

[61] Y. Burnier and M. Laine, "`http://www.laine.itp.unibe.ch/quarkonium`."

[62] K. G. Wilson, *Quarks and Strings on a Lattice*, in *13th International School of Subnuclear Physics: New Phenomena in Subnuclear Physics*, p. 99, 11, 1975.

[63] P. H. Ginsparg and K. G. Wilson, *A Remnant of Chiral Symmetry on the Lattice*, *Phys. Rev. D* **25** (1982) 2649.

[64] E. Follana, Q. Mason, C. Davies, K. Hornbostel, P. Lepage and H. Trottier, *Further Improvements to staggered quarks*, *Nuclear Physics B - Proceedings Supplements* **129-130** (2004) 447.

[65] B. Sheikholeslami and R. Wohlert, *Improved continuum limit lattice action for QCD with wilson fermions*, *Nuclear Physics B* **259** (1985) 572.

[66] M. Lüscher, S. Sint, R. Sommer, P. Weisz and U. Wolff, *Non-perturbative O(a) improvement of lattice QCD*, *Nuclear Physics B* **491** (1997) 323.

[67] R. Sommer, *Scale setting in lattice QCD*, *PoS* **LATTICE2013** (2014) 015.

[68] A. Francis, O. Kaczmarek, M. Laine, T. Neuhaus and H. Ohno, *Critical point and scale setting in su(3) plasma: An update*, *Physical Review D* **91** (2015) 096002.

[69] S. Dürr, Z. Fodor, C. Hoelbling and T. Kurth, *Precision study of the SU(3) topological susceptibility in the continuum*, *JHEP* **04** (2007) 055.

[70] HPQCD and UKQCD Collaborations collaboration, Υ, *Phys. Rev. D* **72** (2005) 094507.

[71] H. Sandmeyer, *Hadronic correlators from heavy to very light quarks*, Ph.D. thesis, U. Bielefeld (main), 2019. 10.4119/unibi/2936264.

[72] H.-T. Ding, O. Kaczmarek, A.-L. Kruse, H. Ohno and H. Sandmeyer, *Continuum extrapolation of quarkonium correlators at non-zero temperature*, *EPJ Web Conf.* **175** (2018) 07010.

[73] P. Hasenfratz, *Prospects for perfect actions*, *Nuclear Physics B - Proceedings Supplements* **63** (1998) 53.

[74] M. Lüscher, S. Sint, R. Sommer and H. Wittig, *Non-perturbative determination of the axial current normalization constant in O(a) improved lattice QCD*, *Nucl.Phys.* **B491** (1997) 344.

[75] S. Capitani, M. Göckeler, R. Horsley, H. Perlt, P. E. L. Rakow, G. Schierholz et al., *Renormalisation and off-shell improvement in lattice perturbation theory*, *Nuclear Physics B* **593** (2001) 183.

[76] T. R. Klassen, *QCD (lattice) potential and coupling: How to accurately interpolate between multiloop QCD and the string picture*, *Phys. Rev. D* **51** (1995) 5130.

[77] QCDSF/UKQCD Collaborations collaboration, *Perturbative and nonperturbative renormalization in lattice QCD*, *Phys. Rev. D* **82** (2010) 114511.

[78] A. Skouroupathis and H. Panagopoulos, *Two-loop renormalization of scalar and pseudoscalar fermion bilinears on the lattice*, *Phys. Rev. D* **76** (2007) 094514.

[79] A. Skouroupathis and H. Panagopoulos, *Two-loop renormalization of vector, axial-vector, and tensor fermion bilinears on the lattice*, *Phys. Rev. D* **79** (2009) 094508.

[80] S. A. Larin, *The renormalization of the axial anomaly in dimensional regularization*, *Physics Letters B* **303** (1993) 113.

[81] C. de Boor, "B(asic)-Spline Basics." `https://www.cs.unc.edu/~dm/UNC/COMP258/Papers/bsplbasic.pdf`, 1986.

[82] S. Caron-Huot, M. Laine and G. D. Moore, *A way to estimate the heavy quark thermalization rate from the lattice*, *Journal of High Energy Physics* **2009** (2009) 053.

[83] F. Karsch, E. Laermann, P. Petreczky and S. Stickan, *Infinite temperature limit of meson spectral functions calculated on the lattice*, *Phys. Rev.* **D68** (2003) 014504.

[84] G. Aarts and J. M. M. Resco, *Continuum and lattice meson spectral functions at nonzero momentum and high temperature*, *Nucl. Phys.* **B726** (2005) 93.

Acknowledgements

My work was supported through the CRC-TR 211 'Strong-interaction matter under extreme conditions'– project number 315477589 – TRR 211. Additionally, my thanks go to the BGTS and HGS-HIRe. I am extremely grateful for the opportunities the mentioned institutions and collaborations have given me.

After many years in this working group and almost a decade at this university, it is time to reflect about the people who were there along the way and to thank everyone who supported me on my quest to get a PhD.

At first, I would like to thank Olaf Kaczmarek, who supervised my work from Bachelor to PhD thesis. Thank you, Olaf, for introducing me to Lattice QCD and taking so much time to explain things. You were always there to discuss and answer questions and your advise to write this thesis like a novel was great. Thanks for always having your door open for your students and for always listening. I always left your office more motivated than I entered it. Doing science is not only a matter of having the correct formula or the fastest code, but also a matter of having the right people to help, to support and to listen. When I will look back at my time at Uni Bielefeld in the future, I am certain I will always remember your help and your encouragement.

I would also like to thank everyone involved in this specific work, especially everyone from our pre-Corona phone call. Thank you, Hai-Tao, Heng-Tong, Hiroshi and Swagato for the fruitful discussions and thanks to Mikko Laine for providing the perturbative spectral functions used in this thesis. I am very thankful that Hai-Tao proofread this thesis and basically all of my other work and provided helpful comments. And, of course, I have to mention Hauke's support over the years. Thank you for teaching me that it is okay to ask questions and to ask for help. From our first visit to China until now, you became a close friend and a constant reminder that company and solidarity are important, in science as well as in real life.

Thanks also to everyone from the working group and from the D- and E-6 floor. Our conversations were great and I surely miss the lunch breaks together. Thanks, Lukas, David and Hauke (again). Sharing an office with you has been great and I am really thankful that you tolerated all my chaos.

I would also like to thank all my friends for all the epic adventures, the parties, the deep conversations until late at night, the countless coffees enjoyed together, the walks, the hugs, the support and your open ears. Thank you for the great time!

I am very grateful for all the support I received from my family. Thanks for believing in me and providing support, without which I would certainly not be where I am now.

And last but not least, I would like to thank my wonderful husband. Flo, you are the best. Your support helped me during stressful times and your

encouragement motivated me to keep going. Thanks for staying with me through the highest highs and lowest lows.

Disclaimer

I hereby declare that the work done in this thesis is that of the author alone with the help of no more than the mentioned literature and auxiliary means.

Bielefeld, 15.06.2021

_____

Anna-Lena Lorenz

Gedruckt auf alterungsbeständigem Papier gemäß DIN ISO 9706.